From Disorder to Order

Shear rheology of macroscopically structured materials

Gerard Giménez Ribes

Propositions

1. Using macroscopic model systems facilitates our understanding of microscopic structures.

   (this thesis)

2. Shear-induced normal stresses are too often ignored in the mechanical characterization of new materials and foods.

   (this thesis)

3. The problem of "black boxes" as scientific equipment is slowing down science progress worldwide.

4. All the reasons leading to conspiracy theories that were mentioned in Hornsey *et al.* (2023) can be summarized as a lack of engaging and effective science communication.

   Hornsey, M. J., Bierwiaczonek, K., Sassenberg, K., & Douglas, K. M. Individual, intergroup and nation-level influences on belief in conspiracy theories.*Nature Reviews Psychology*, 2(2), 85-97, (2023).

5. Society's perception of science as a closed body of knowledge instead of simply as a way of thinking promotes science rejection.

6. Practicing outdoor sports in nature benefits not only the physical and mental health, but also the society and environment.

7. Cultures with consolidated culinary tradition come accompanied by high food neophobia.

Propositions belonging to the thesis, entitled:

From disorder to order: Shear rheology of macroscopically structured materials

Gerard Giménez I Ribes
Wageningen, 26 September 2023

From disorder to order

Shear rheology of macroscopically structured materials

Gerard Giménez I Ribes

Thesis committee

Promotor
Prof. Dr Erik van der Linden
Professor of Physics and Physical Chemistry of Foods
Wageningen University & Research

Co-promotor
Dr Mehdi Habibi
Associate professor, Physics and Physical Chemistry of Foods
Wageningen University & Research

Other members
Prof. Dr Jasper van der Gucht, Wageningen University & Research
Prof. Dr Martin van Hecke, Leiden University
Prof. Dr Mokhtar Adda-Bedia, École Normale Supérieure de Lyon, France
Dr Joshua Dijksman, University of Amsterdam

This research was conducted under the auspices of VLAG Graduate School (Biobased, Biomolecular, Chemical, Food and Nutrition Sciences).

From disorder to order

Shear rheology of macroscopically structured materials

Gerard Giménez I Ribes

Thesis
submitted in fulfilment of the requirements for the degree of doctor
at Wageningen University & Research
by the authority of the Rector Magnificus,
Prof. Dr A.P.J. Mol,
in the presence of the
Thesis Committee appointed by the Academic Board
to be defended in public
on Tuesday 26 September 2023
at 4 p.m. in the Omnia Auditorium.

Gerard Giménez I Ribes

From disorder to order: Shear rheology of macroscopically structured materials, 250 pages.

PhD thesis, Wageningen University, Wageningen, The Netherlands (2023)
With references, with summary in English

ISBN: 978-94-6447-754-2
DOI: https://doi.org/10.18174/633120

Contents

Chapter 1

General introduction

From a soft matter perspective, order and disorder are key concepts in understanding material organization and behavior. Order usually refers to an arrangement or pattern in a system where its components, such as atoms, molecules, or unit cells, have a high level of organization or regularity. Systems with regular, structured arrangements, such as crystals [1], self-assembled supramolecular structures [2], or metamaterials with arranged unit cells [3, 4] exhibit order. On the contrary, disorder is associated with structural components lacking a predictable spatial organization, such as amorphous solids [5] and many polymers [6]. In this thesis, entitled "From disorder to order: Shear rheology of macroscopically structured materials", we will deal with structural (dis)order in materials from a macroscopic perspective.

1.1 Macroscopically disordered systems

Disordered systems are ubiquitous in nature and in everyday life. Most people might think of daily situations such as a disordered bedroom, a messy office desk, or a crumpled paper ball. However, many soft matter physicists might think instead of glasses, polymers, gels, or emulsions. All these cases share important traits: lack of an ordered spatial arrangement, and some frustration that prevents their evolution to an ordered configuration, at least for a period of time. However, there are clear differences between everyday disordered systems and those studied in soft matter physics, with the most obvious one being the scale of the system at which we observe the disorder. We are familiar in daily life with disordered systems at the macroscopic scale, since we can clearly see the components and the lack of any ordered spatial arrangement. However, in the case of microscopic disordered systems, also known in the literature as amorphous solids [5, 7], or materials with dynamic heterogeneity [8], they might seem ordered at the macroscopic scale, but lack any spatial long-range order at the microscopic scale. In the case of a window glass, a mayonnaise, or a polymer melt, they appear uniform to the naked eye, while they present profound disorder at the microscopic scale.

Studying the deformation of materials is a common way to characterize their behavior under stress for practical applications and to understand the interplay of its structural elements when deformed [9]. No material is used for construction without an analysis of its behavior under stress, and no new food product is released on supermarket shelves without studying its texture or viscosity. In the case of amorphous solids, their study under deformation has long been employed by the scientific community to understand what gives rise to their peculiar properties [10]. However, in many cases linking a certain mechanical response to specific physical processes happening at the microscopic scale is challenging.

It is not surprising, therefore, that certain materials have arisen as macroscopic candidates for model systems to study the physics of microscopic disordered materials. Two such systems mentioned in the literature, which are studied in this thesis, are crumpled materials and entangled chains or ropes. Crumpled systems, such as a simple crumpled paper ball, have been shown in the past to exhibit similarities with amorphous disordered solids, such as glasses [11]. In the case of amorphous solids, there exists an energy landscape with large energy barriers and local minima, which prevents the system from reaching a global minimum, thereby remaining in a disordered or amorphous state [5, 12]. A similar situation occurs in crumpled materials, where through the process of randomly crumpling, a disordered structure is created with a self-avoiding structure where the structural components do not intersect each other and frustrated regions, which are prevented from reaching a global energy minimum [11, 13]. We review the similarities between crumpled materials and disordered amorphous solids extensively in **Chapter 2**, and study the deformation of crumpled materials under shear in **Chapter 3**.

In the case of entangled chains, their similarities with microscopic polymer chains have been used in the past to better understand the effect of entanglements or entropy in polymer physics. Numerous models have been created to elucidate the impact of entanglements on polymer rheology. One notable example is the model introduced by de Gennes, which incorporated the concept of reptation [14, 15]. This model was later refined into reptation theory by Edwards and Doi, providing a robust framework for understanding entanglements in polymers [6, 16]. The influence of topological constraints on polymer rheology and the physical mechanisms governing the flow or deformation of systems such as polymer gels or rubbers is key for understanding and predicting polymer behavior. As the de Gennes-Edwards-Doi reptation theory builds on physical constraints rather than specific particle interactions, and these physical constraints are difficult to control at the microscopic level experimentally, macroscopic models have been used to study polymer dynamics. An example of this system is the granular chain with beads connected via flexible links, which we can easily find in sink stopper chains or window shade pulls. The granular chain is based on the theoretical model system using freely jointed bead-rod chains which were already used by Kramers in 1944 [17]. Ben-Naim, Daya, Ecke, and co-workers [18–20] introduced this macroscopic model system as a means to study the opening time of knots, the entropic tightening of chains, and the diffusion of rings. Since then, these macroscopic versions of polymer chains have been used in greater depth for polymer research, as they are easily cut and modified physically [21–36]. These macroscale model systems with chains have already shown good compliance with nanoscale models for translocation or diffusion [26, 37], and for compression experiments [31, 35, 38]. Granular chains have also been used as a means of studying the physics behind the glass transition, both alone [21], and together with spherical inclusions [39, 40]. In **Chapter 4**, we study the behavior of entangled macroscopic chains or ropes under shearing deformations.

However, how to use these macroscopic structures to gain insight into microscopic systems is still an open question, mainly caused by the lack of understanding of what happens to these macroscopically disordered structures when they are deformed. Specifically, both crumpled systems and entangled chains have been studied previously under uniaxial or isotropic compression, but not under shear deformations, and therefore a complete rheological characterization is still lacking.

1.2 Macroscopically ordered systems

1.2.1 Anisotropy in meat (analogues)

Skeletal muscle tissue, commonly known as meat, has a hierarchical structure made up of fibers. At the microscopic level, these fibers are composed of myofibrils, which are roughly in the μm range in diameter and formed by fibrillar structures. Myofibrils are composed of sarcomers, which are repeating units that contain myofilaments, specifically macromolecules myosin and actin, responsible for muscle contraction and relaxation [41]. In addition to fibers, each muscle fiber is surrounded by connective tissue called endomysium, while several fibers are bundled together by perimysium [42]. Endomysium and perimysium allow proper movement of the fibers during muscle contraction. While the main structure of muscle tissue is generally similar, there are variations between different muscles and animals [43]. Therefore, the meat structure consists of roughly ordered arrangements of quasi-1D filaments, providing a system with the same basic components of **Chapter 4** but with increased structural order.

Despite extensive research on meat structure, methods for quantitative comparison of meat analogues with real whole-cut meat are still limited [44]. The Warner-Bratzler test is commonly used to test shear deformations of meat samples, which involves a V-shaped blade that applies a cutting deformation to the product [44]. However, this method applies a combination of mechanical deformations and is primarily used to assess quality attributes rather than precise physical attributes [45]. The Kramer Shear Cell, which uses multiple parallel blunt blades to simulate a bite into food, also suffers from a similar issue [44].

In order to develop meat analogues that mimic whole-cut meat, an important step is to understand the effect of meat anisotropy on the shear and shear-induced normal force responses. Specially for complex deformations such as chewing, which occur outside the linear viscoelastic (LVE) regime [46–49], understanding the normal force response induced upon shear is important, and has been ignored in the previous literature on food products. In **Chapter 5** we address this issue by studying the large amplitude oscillatory shear (LAOS) response of meat and meat analogues with fiber orientations parallel or perpendicular to the shear direction. Furthermore, we also studied the shear-induced normal force response, in meat and meat analogues. These concepts were previously studied on simple materials, but have been completely ignored in the field of food science. Therefore, we provide a complete mechanical characterization of meat and meat analogue samples that present anisotropy. The linear and nonlinear rheology used in this thesis is explained in more detail in section 1.4

1.2.2 Asymmetry in cylindrical shells

Cylindrical origami shells are commonly used to design new mechanical metamaterials, engineered materials with properties not found in the materials themselves, but derived from their specific structural arrangement [3]. Applications range from shock absorption [50] to soft bistable electricity generators [51], or self-deployable stent grafts for medical applications [52]. However, despite the practical applications for which the origami bellows are being used, the shear resistance, and more specifically, the shear-induced normal force response, remains largely unexplored. The origami shells, as well as the crumpled materials studied experimentally in **Chapter 3**, present the same type of basic structural units: folds arranged in creases and vertices. However, in the case of origami patterns, this network of folds is arranged in a specific order, whereas in crumpled materials it is completely random. Therefore, in this thesis the origami studied in **Chapter 6** represent the ordered version of the structural components studied in **Chapter 3**.

In this thesis, three specific types of origami shells are studied: Yoshimura, Kresling, and crumpled origami. The Yoshimura pattern arises naturally under uniaxial compression with appropriate conditions of buckling load, strain, and compression rate, and consists of a diamond pattern with diagonal mountain folds and horizontal valley folds [53]. If instead of uniaxial compression, a twist deformation is performed, a Kresling design is obtained, which resembles the Yoshimura design, but with the diamonds tilted toward the direction of rotation [54, 55]. Therefore, the Yoshimura and Kresling designs offer good candidates to study the effect of structural arrangement and symmetry/asymmetry in cylindrical shells, particularly because these properties arise from their ordered folding patterns.

Although folded origami cylinders made with Yoshimura or Kresling designs already contain the symmetry or asymmetry in their design, a cylinder containing a pattern made randomly by uniaxial compression was also compared. With a material such as paper, which can easily buckle and bend, a pattern that resembles the Yoshimura design can be obtained, as shown for conical paper shells in [56], while still presenting randomness and imperfections. The pattern is therefore semi-ordered, as some randomness is still present in the system, which is composed of crumpled unit cells. This allowed us to study in **Chapter 6** systems where a well-defined asymmetry is present in the pattern, and compare with a system where the asymmetry is introduced randomly upon compression.

1.3 Core objective of this thesis

As indicated in section 1.1, crumpled materials and granular chains offer interesting macroscopic systems to study due to their similarities with disordered solids. However, before a direct comparison can be made between the macroscopic and microscopic systems, a deeper understanding of the structures in these systems is needed. Furthermore, both crumpled materials and entangled systems present interesting properties by themselves that make them good candidates for use for practical applications as disordered mechanical metamaterials [57, 58], as we discuss in **Chapters 2, 3,** and **4**. The primary characteristics of these systems often originate from their geometric structure. As such, these properties can be considered generic, persisting across different length scales. However, it is important to note that factors such as molecular interactions, thermal fluctuations, and friction may induce variations, thereby influencing the effect of the geometric structure at different length scales.

Shear rheology provides a valuable tool for studying how these structures respond under stress, and specifically large deformations have the potential to provide rich information. Surprisingly, the response in shear of these macroscopic disordered systems has been largely ignored in previous studies. Under shear deformations, it becomes clear how the internal structures of these disordered systems play a role in their mechanical response. The internal structures in crumpled materials can have preferred orientations, which therefore result in anisotropy, as shown in **Chapter 3**. In the case of entangled chains or ropes studied in **Chapter 4**, the shear rheology showed the effect of topological constraints on the sheared area of the sample and the stiffening upon shear. These results were then used to study two more applied systems, which present anisotropy, where the components of previous chapters are used in more ordered arrangements. In **Chapter 5**, we studied meat and plant-based meat analogues where the samples presented anisotropy in the form of fiber orientations, therefore being an ordered counterpart of the quasi-1D filaments used in **Chapter 4**. Finally, in **Chapter 6** we studied cylindrical paper shells with well-defined symmetry/asymmetry and compared with asymmetry formed randomly by crumpling. **Chapter 6** contains therefore a more ordered arrangement of the basic structures present in **Chapter 3**: folds in the form of creases and vertices.

The primary objective of this thesis is therefore to understand the role of structures within macroscopically disordered materials, such as crumpled materials and entangled assemblies of filaments, by investigating their mechanical response under shear stress. By employing nonlinear shear rheology, we aim to uncover the role of internal structures, anisotropy, and topological constraints in these systems. Afterward, we explore the role of the same structures, but in more ordered arrangements and more applied systems that present clear anistropy, such as meat and plant-based meat analogues, as well as origami cylindrical paper shells with defined symmetry/asymmetry.

In the following section, we provide an introduction to the shear rheology, both linear and non-linear, used in the experimental chapters of this thesis. Finally, we present an overview of the thesis projects.

1.4 Introduction to shear rheology

1.4.1 Small amplitude oscillatory shear (SAOS)

Rheology is the field of science that focuses on studying the deformation and flow of materials. First coined in the 1920s by Eugene C. Bingham, it is formed from the ancient greek words "*rhéo*" (to flow), and the suffix "*logy*" (study of) [46]. Rheology is now a well-established domain within material sciences in general and is at the core of the study in miscellaneous scientific fields where flow or deformations are involved, such as polymers, foods, adhesives, cosmetics, geology, or waste industry, just to name a few.

At its core, the rheological properties are well summarized by the starting sentence of Ewoldt *et al.* [59]: "Rheological properties answer the question, 'What happens when I poke it?'". While the general population may be unaware of the scientific discipline of rheology, they are well aware of the intuitive concept behind it: shaking a ketchup bottle to get it to pour, squeezing a tube of toothpaste to dispense the paste, or running on a cornstarch suspension without sinking. All of these are iconic cases where the rheological properties of the material are at play and could be quantified if desired.

When a force is applied to a material, a corresponding deformation is induced resulting in a strain, which is a measure of the change in size or shape of an object relative to its original dimensions. This deformation behavior can be described rheologically, and for most materials, the response sits in between a purely elastic deformation where no energy is lost, or a flow of viscous fluid, where all the energy is dissipated to the medium. Therefore, most materials behave as viscoelastic materials, where some of the mechanical energy applied is stored and some is transformed into heat via viscous dissipation [46].

There are three main types of strain: 1) normal strain, resulting in extension/contraction deformations, 2) shear strain, resulting in shear deformations, and 3) volumetric (or bulk) strain, which changes the volume of the sample. Mostly, the first two are amply used in research and industry, because they are easier to apply in a laboratory setting. In normal strains, two particles are displaced away or toward each other, whereas in shear strains, two particles are displaced over or past each other. These two different types of strain are represented in Figure (1.1). From these simple deformations, we can already start defining the terms that will be used throughout this thesis, where mainly shear deformations were performed. Some simple mechanical characterizations were also performed via compressive or extensional deformations, and are explained in the corresponding chapters. For this reason, mostly shear rheology of soft solid materials will be discussed in this general introduction (**Chapter 1**).

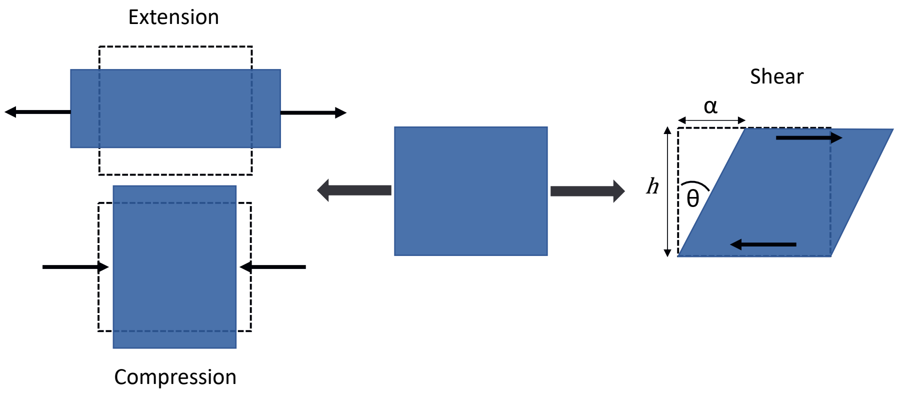

Figure 1.1: Schematic depiction of normal strain in the form of extension/compression on the left, and shear strain causing a shear deformation on the right. Figure adapted from [60].

The force, F, applied to a material per unit area, A, is defined as stress, σ, applied on the material:

$$\sigma = \frac{F}{A} \tag{1.1}$$

When σ is applied on the material, it will cause a deformation, or relative change in length as mentioned earlier, defined as strain,

$$\gamma = \frac{\alpha}{h} = \tan\theta, \tag{1.2}$$

where α is the change in length, and h is the original length of the material. When a small shear deformation is applied to a purely elastic material, the ratio of stress to deformation corresponds to a material constant, the shear modulus G, so that

$$G = \frac{\sigma}{\gamma}. \tag{1.3}$$

As far as that ratio remains constant, the material is within the so-called linear elastic range, and G is a measure of the material rigidity [61]. However, for viscoelastic materials the energy is not completely stored, as mentioned earlier. A useful way to characterize viscoelastic materials is through the use of oscillatory tests, which have been used extensively in this thesis. In oscillatory tests a sinusoidal γ is applied to the material,

$$\gamma(t) = \gamma_0 \sin(\omega t), \tag{1.4}$$

where γ_0 is the strain amplitude, ω is the frequency, and t is the time. The resulting σ is then measured by the rheometer, and its analysis offers a plethora of results to characterize material properties. Since for viscoelastic materials part of the mechanical energy is stored, and part is dissipated, the stress response is represented as a phase-shifted sine function

$$\sigma(t) = \sigma_0 \sin(\omega t + \delta), \tag{1.5}$$

where σ_0 is the stress amplitude and δ corresponds to the phase shift between the strain and stress signals, as indicated in Figure 1.2.

As was the case for simple shear deformations, the ratio between stress and strain gives us a modulus, in this case the complex shear modulus,

$$G^* = \frac{\sigma(t)}{\gamma(t)}. \tag{1.6}$$

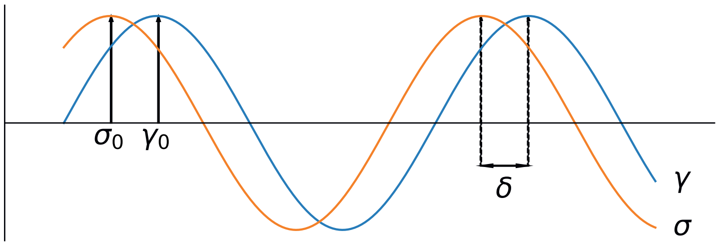

Figure 1.2: Sinusoidal strain, γ, and resulting stress response, σ. The amplitude of strain and stress, γ_0 and σ_0, respectively, and phase shift, δ, are shown.

By analyzing the oscillatory $\sigma(t)$ via Fourier Transform, which decomposes the signal into a sum of waves of varying amplitude and frequency, σ_0 and δ are obtained from the amplitude and phase shift of the fundamental sine wave (See Fig. 1.2). By this mean, the signal can be decomposed into a real and imaginary part, orthogonal to each other, so that [61]

$$G^* = G' \sin \omega t + G'' \cos \omega t, \tag{1.7}$$

where $G' \sin \omega t$ is the component in phase with the strain wave, G' denotes the storage modulus, indicative of the stored energy, $G'' \cos \omega t$ is the component 90^o out of phase, and G'' denotes the loss modulus, indicative of the dissipated energy. Equation (1.7) can be rewritten as

$$G^* = G' + iG'', \tag{1.8}$$

where i is the imaginary number. This relation and the orthogonality between moduli is depicted in Figure (1.3).

Both G' and G'' are independent of the γ and σ in the LVE regime, and are measured in short amplitude oscillatory shear (SAOS) tests. However, as the amplitude of deformation is extended into the non-linear viscoelastic (NLVE) regime in large amplitude oscillatory shear

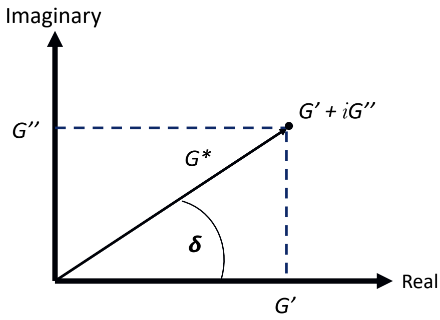

Figure 1.3: Vector diagram of the complex modulus G^* and its components in the real space (storage modulus G'), and imaginary space (loss modulus G''). δ denotes the phase angle.

(LAOS) experiments, both moduli become functions of the strain amplitude, $G'(\gamma_0)$ and $G''(\gamma_0)$. When going into the NLVE regime, the stress signal becomes distorted by the presence of higher harmonics, and therefore the analyses of G' and G'' performed from the first harmonic, become mathematically inacurate [62] and different analyses are required. The higher harmonics are waves with a frequency which is a positive integer multiple of the first (or fundamental) harmonic, as shown in Figure 1.4.

1.4.2 Going into large amplitude oscillatory shear (LAOS)

While SAOS tests fully describe the material response at small deformations, and therefore gives a convenient rheological characterization of soft materials, most real life deformations will be both large and fast, happening in the NLVE regime [62]. In this thesis, we aimed to measure the different materials not only in the small LVE regime, but also when the deformations are in the NLVE regime, to obtain a richer mechanical characterization of the materials and structures. Continuing with the description of oscillatory tests explained in the last section, we will extend

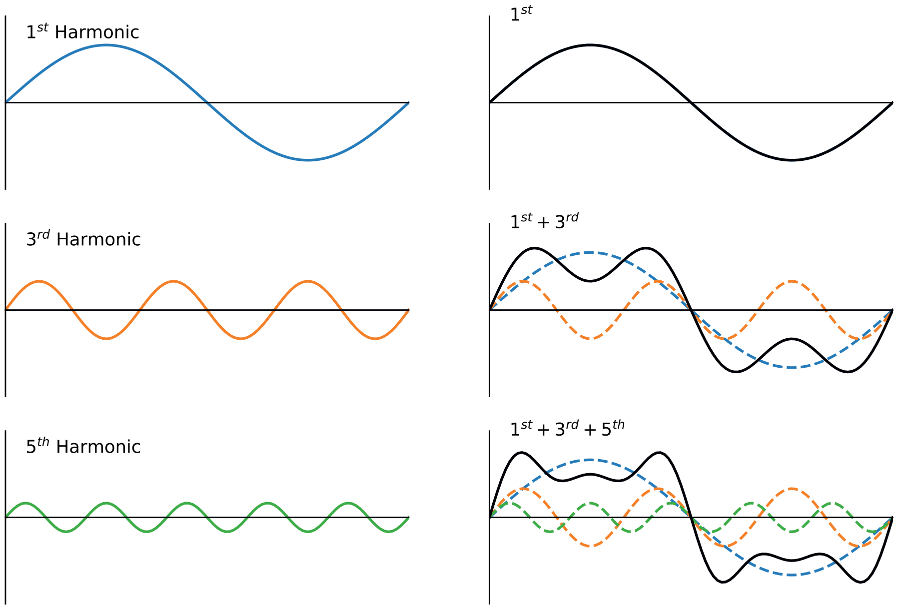

Figure 1.4: Representation of the first (fundamental) harmonic, as a simple sine wave, and how the addition of odd higher harmonics (third and fifth) affect the oscillatory signal (black). The amplitudes of the harmonics are 1 for the 1^{st}, 0.5 for the 3^{d}, and 0.25 for the 5^{th}.

here the description for the LAOS techniques used in this thesis.

Since the calculation of G' and G'' performed by the rheometer makes use of the first harmonic in the oscillatory stress signal, rich information on the material behavior at LAOS deformations is lost. Simply by plotting parametrically the γ vs σ signals, we can obtain information in the LAOS regime. This type of plots are known as Lissajous-Bowditch [63] plots (referred simply as Lissajous plots from now on). In Figure (1.5A-C), examples of responses in the LVE regime are shown, with a purely elastic response (phase angles of 0^0, slightly shifted for visualization purpose), a purely viscous response (phase angle of 90^0), a linear viscoelastic response (phase angle of 45^0). A non-linear viscoelastic response is also shown (Fig. (1.5D)) with higher harmonics present in the stress signal.

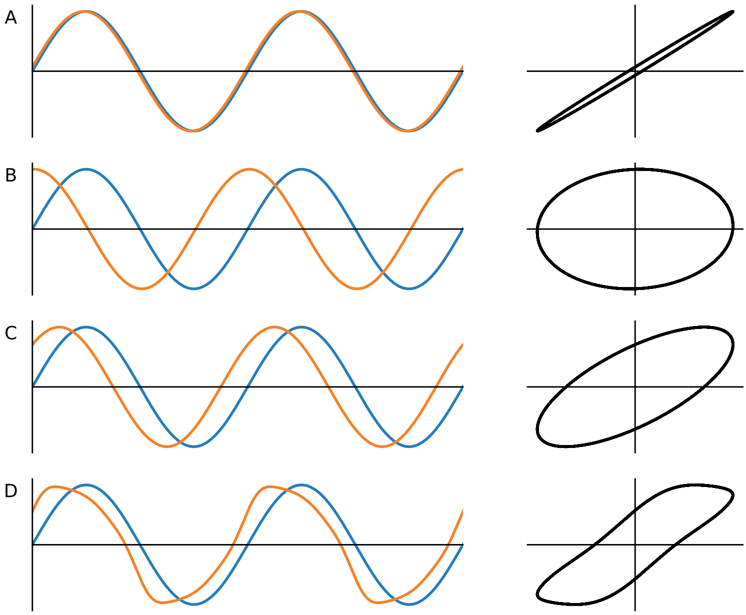

Figure 1.5: Example of linear elastic response (A), linear viscous response (B), linear viscoelastic response (C), and non-linear viscoelastic response (D). Blue line corresponds to $\gamma(t)$, and orange to $\sigma(t)$.

LAOS rheology is by no means new, since early publications in the 1960s already studied the non-linearity phenomena of viscoelastic materials in oscillatory shear, such as the study from Payne [64]. In that study, the author observed the dependence of shear moduli on strain amplitude for rubber filled with carbon black particles, and reported the non-linear behavior as “dynamic stress softening”, which is currently known as “Payne effect” [64]. It was during the 1990s that book chapters by Giacomin and Dealy [65] and Dealy and Wissbrun [66] offered more detailed protocols for LAOS experiments, and the interpretation of the data via Fourier series, hence giving rise to the Fourier Transform (FT)-rheology. While eq. 1.5 describes the sinusoidal stress oscillation in the LVE regime, such as that shown in Fig. (1.5A-C), becomes clear that contributions from higher harmonics are needed to explain the oscillatory stress curve in Fig. (1.5D). Assuming the shear stress response is symmetric when shearing in both directions, *i.e.* independent of the shear direction, then the stress must be an odd function (i.e., present only odd harmonics) with respect to the shear deformation direction. This is also assumed throughout the experimental chapters in this thesis (except in **Chapter 6**, where we used samples presenting asymmetry in both shear directions). Therefore, the stress response can be represented as a Fourier series of odd harmonics [62]

$$\sigma(t) = \sum_{n=1,\, odd} \sigma_n \sin(n\omega t + \delta_n), \tag{1.9}$$

where σ_n represents the stress amplitude of the n harmonic, and δ_n the phase shift of the n harmonic. However, while FT-rheology is a very sensitive indicator of non-linearity, the FT-rheology framework lacks clear physical interpretation of the higher harmonics coefficients. Therefore, in our experimental chapters (**Chapters 3** and **5**), we use mostly the methodology developed by Randy Ewoldt and coworkers in the late 2000s [63, 67]. In **Chapter 4**, however, we used a four blade vane geometry, which has ill-defined stress and strain fields, and therefore we limit ourselves to plotting the raw torque as function of deflection angles to construct the Lissajous curves. In [63, 67], the authors developed a framework that makes use of the previously reported FT higher coefficients describing the non-linear stress responses via the use of Chebyshev polynomials of the first kind. Two of the parameters defined to quantify the LAOS response that we used in the current thesis are the strain-stiffening ratio (S) and the dissipation ratio Φ. The S ratio is defined as [63]

$$S = \frac{G'_L - G'_M}{G'_L}, \tag{1.10}$$

where $G'_L = \frac{\sigma}{\gamma}|_{\gamma=\gamma_0}$ is the shear elastic large-strain modulus at γ_0, and $G'_M = \frac{d\sigma}{d\gamma}|_{\gamma=0}$ the shear elastic minimum-strain modulus. Both the G'_L and G'_M are schematically represented in Figure 1.6. The S ratio indicates then the strain stiffening (or softening) within a cycle (intracycle stiffening), as it is obtained from the local slopes of the Lissajous curves. If the sample is in the linear regime, then the Lissajous has an ellipsoidal shape, such as that shown in Fig. 1.5C, and $G'_L = G'_M = G'$, so $S = 0$, and thus the G' obtained from the first harmonic captures accurately the rheological response. However, this intracycle information is lost if one only looks at the G' and G'' curves obtained from the first harmonic [63] for measurements performed outside the NLVE regime.

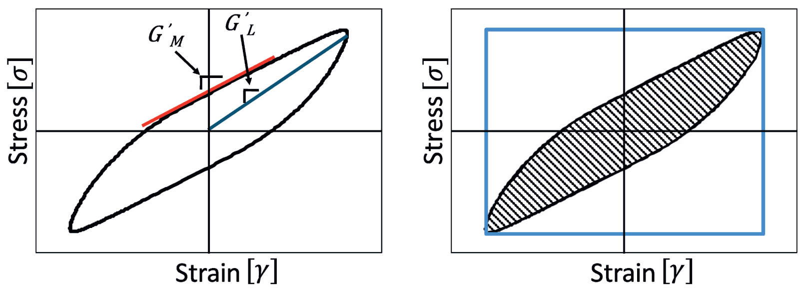

Figure 1.6: Example of Lissajous-Bowditch curve indicating the elastic modulus at largest strain, G'_L , and the elastic modulus at minimum strain, G'_M, on the left. And the dissipation ratio represented by the area enclosed within the Lissajous-Bowditch curve (hatched pattern) over the total possible plastic energy dissipation (blue rectangle) on the right.

An analogous ratio, the shear-thickening ratio, T, was also defined from the viscous Lissajous curves (stress vs shear rate) [63], but will not be discussed here as our materials, being soft solids, exhibit a mostly elastic response.

The second parameter used in this thesis is the dissipation ratio (Φ) defined as [67]

$$\Phi = \frac{E_d}{(E_d)_{pp}} = \frac{\pi\gamma_0 G_1''}{4\sigma_{max}}, \tag{1.11}$$

with $E_d = \oint \sigma d\gamma = \pi\gamma_0^2 G_1''$ being the energy dissipated per unit volume within a LAOS oscillation cycle (hatched pattern in right Lissajous, Fig. 1.6), and $(E_d)_{pp} = (2\gamma_0)(2\sigma_{max})$ the possible maximum energy dissipated by a perfect plastic material an oscillation cycle (blue rectangle in right Lissajous, Fig. 1.6). G_1'' corresponds to the first harmonic loss modulus, which is the only one contributing to the total energy dissipation [67, 68].

1.4.3 Normal response induced by shear

So far, we have described in sections 1.4.1 and 1.4.2 the shear stress response during shear deformations. However, shearing a material also induces a normal force response, which in most literature on shear deformations is largely ignored. Already in 1909, Poynting discovered when twisting piano wires, that the torsion induced an axial dilation, or a normal force induced by shear [69, 70]. This normal force follows a quadratic relation with γ with a coefficient known as Poynting modulus, G_N, so that

$$\sigma_n = G_N\,\gamma^2, \tag{1.12}$$

where σ_n is the normal stress [71, 72]. For most materials, G_N, takes on positive values, which leads to the conventional Poynting effect [72]. However, more recently some complex materials have been observed to exhibit a reversed Poynting effect, i.e., negative G_N, such as biopolymer gels [73].

Eq. 1.12 holds true for isotropic materials, or anisotropic materials that show symmetry on both positive and negative direction of shear. However, for anisotropic materials that do not show symmetry on positive and negative direction of shear, the normal force response usually obtains linear terms as a function of shear, i.e. one direction of shear causes a positive normal force response and the opposite direction results in a negative normal force response. Therefore, the shear-induced normal force can be used to get insigt into the structural properties of the system. In **Chapter 6**, we show this is true with origami cylinder designed with symmetric and asymmetric patterns with the shear directions.

While eqs. 1.12 and 1.3 can be used directly for rheometer geometries such as the cone-plate and plate-plate geometry (used in **Chapter 5**) to obtain G_N and G, this is not the case for cylindrical shells, which we studied in **Chapter 6**. For cylindrical shells with an inner radius R_{min} and an outer radius R_{max}, the normal force response during shear can be written as [72]

$$F_N = G_N \, J \left(\frac{\varphi}{h}\right)^2, \tag{1.13}$$

where $J = \frac{\pi}{2}(R_{max}^4 - R_{min}^4)$ is the second moment of inertia, φ is the deflection angle, and h is the height of the shell. Taking an average radius for the shell, so that $R = (R_{max} + R_{min})/2$, the shear force for the shell is written as [72]

$$F_S = \frac{\tau}{R} = \frac{GJ\varphi}{Rh}, \tag{1.14}$$

where τ is the torque around the axis of the shell. In **Chapter 6** we show that eqs. 1.13 and 1.14 are applicable for an origami cylindrical shell which has a symmetric pattern in positive and negative directions of shear, a Yoshimura design. For an origami cylindrical shell which shows asymmetry in both directions of shear such as the Kresling design, eq. 1.13 fails to fit adequately the shear-induced normal force response, and therefore a linear approximation via Taylor's expansion was used.

1.5 Thesis aim and overview

As we generally explained in this general introduction, we aim to investigate specific systems in each **Chapter (2-6)**, with a focus on systems presenting different ordering level at the macroscopic scale. Here we provide an overview of the systems we studied and our approaches.

1.5.1 Studied systems and approaches

We started the thesis by researching the rheology of macroscopically disordered materials. First, in **Chapter 2** we performed a review on crumpled materials, understood from a disordered or amorphous solid perspective, and provided examples for designing disordered mechanical metamaterials by introducing crumpling.

In **Chapter 3** we addressed an area of crumpled materials still to be explored: shear deformations. All previous literature on crumpled materials so far has focused on uni-axial or isotropic compressions. However, comprehending their behavior under shear is crucial for effectively utilizing these systems in practical applications. In this chapter we studied the shear behavior of crumpled materials, individually investigating the effect of material training, internal morphology, friction, and plasticity, through non-linear shear rheology.

In **Chapter 4** we moved to another macroscopically disordered system amply used in literature as polymer analogue, macroscale granular chains, and compared the results also to cooked spaghetti. As for the crumpled materials, the deformation behavior of entangled macroscale chains and spaghetti has so far been studied under compression or penetration tests, but not under shear deformations. Using a vane geometry and a rheometer head, we studied the effect of chain length on the rheological properties of granular chains and spaghetti, combining the results with image analysis and simulations.

Then, we studied two more application-driven systems, where the level of order was increased, applying part of the knowledge found in **Chapters 2-4**. In **Chapter 5**, we studied the effect of fiber orientation on the rheological response of meat and meat analogues. Using a combination of shear stress together with shear-induced normal stress, we explain how the structure of the samples affects the mechanical response. This allowed us to develop a novel methodology to quantitatively compare whole-cut meat samples with plant-based meat analogues mimicking the meat fibrous structure, and potentially other food samples presenting structural anisotropy.

Finally, in **Chapter 6** we investigated a specific class of mechanical metamaterials, origami bellows, and the effect of introducing disorder with a crumpled cylinder mimicking an origami bellow. By integrating the analysis of shear stress and shear-induced normal stress as done in **Chapter 5**, and combining it with simulations of the unit cells of the systems, and image analysis of the crumpled pattern, we performed a complete mechanical characterization of the origami cylinders. This approach allowed us to relate the structural arrangement and (a)symmetry with the shear direction to the normal stress response.

1.5.2 Structure of the thesis

In addition to the General Introduction (current **Chapter 1**), this thesis consists of one review chapter (**Chapter 2**), four experimental chapters (**Chapters 3-6**), a general discussion (**Chapter 7**), and summary. Some of the chapters contain Supplementary Information (provided after the main text in the corresponding chapter). The references for the whole thesis are listed after **Chapter 7**, before the summary.

1

Chapter 2

Crumpled structures as robust disordered mechanical metamaterials

This chapter is published in a revised version as:
G. Giménez-Ribes, M. Motaghian, E. van der Linden, & M. Habibi, Crumpled structures as robust disordered mechanical metamaterials. *Materials & Design*, 232 (2023), 112159.

Abstract

Mechanical metamaterials such as origami or ordered 3D printed structures have shown tremendous applications in science and technology. However, the main disadvantage of these systems is their dependency on a perfectly ordered structure, making them sensitive to defects. Disordered metamaterials offer a way to circumvent this sensitivity. Within disordered metamaterials, crumpled systems have recently received increased attention due to their intriguing properties such as negative Poisson's ratio, low density, high mechanical shock absorption, and easy manufacturing process. Mechanical relaxation of these systems was successfully explained by stretched exponential and logarithmic models, typically used for complex relaxation in amorphous systems. This drove researchers to study crumpled systems as amorphous systems with a complex energy landscape. Further research remarked similarities between crumpled structures and other metastable systems such as glasses, by studying the mechanical memory effect. Edward's statistical mechanics was also applied to crumpled systems to unravel their statistical properties. In this review, we summarize different aspects of crumpled materials and their potential to be exploited for designing new robust disordered metamaterials. Finally, we build on the current knowledge and introduce a design principle to make crumpled origami-like structures with robust mechanical responses and briefly compare them with ordered origami structures.

2.1 Introduction

Overcoming fundamental restrictions to tailoring the functionality of natural materials has been an aim of science throughout history. Throughout history human life was revolutionized by utilizing novel materials in such a way that different eras of civilization are named by these materials: e.g. the stone, bronze and silicon age. Now we live in a new era where recent developments in science and technology have helped us to go beyond what nature has offered us, and scientists and engineers are trying to create materials that can be precisely programmed for the desired purposes.

It was already in the 1960s when the concept of metamaterial appeared to designate materials with electromagnetic properties not found in nature [74]. Later on, the concept of metamaterial expanded to all sorts of materials whose properties arise from the design of the material rather than its composition. As a result, nowadays, a rough classification of metamaterials in four different categories exists, i.e., electromagnetic metamaterials, acoustic metamaterials, thermal metamaterials, and mechanical metamaterials [74]. Research on mechanical metamaterials focuses on the mechanical energy, motion, stress or deformation of metamaterials [3]. These structures have been engineered in a way that the material exhibits mechanical characteristics that cannot be found in conventional materials, for instance: negative Poisson's ration [75–77], or negative bulk moduli [78]. One of the reasons for the success of mechanical metamaterials in recent years is undoubtedly the rise of 3D printing technologies for creating novel complex structures [4]. Figure 2.1, shows some examples of cylindrical mechanical metamaterials fabricated by 3D printing of soft elastomers. Mechanical metamaterials are often designed by repeating a unit-cell in a symmetric lattice, and therefore, they are dependent on specific geometrical restrictions and the interplay between their subunits. In turn, this deteriorates the functionality of mechanical metamaterials when any imperfection appears in their structure. Disordered mechanical metamaterials can offer a solution, and therefore can provide more robustness for tailoring functionality without requiring all

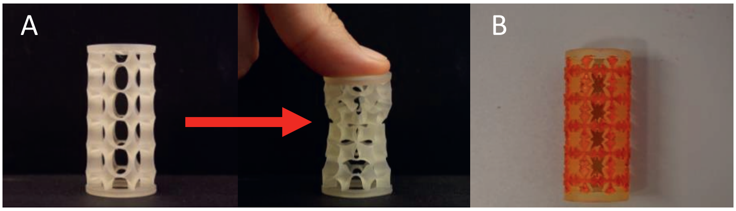

Figure 2.1: Examples of cylindrical mechanical metamaterials with different properties: (A) Auxetic structure designed with circular voids that show negative radial strain under axial compression, (B) Network of nonuniform beams designed with four-fold symmetric voids that exhibits shear (torsion) under axial compression and is capable of programming the sign and magnitude of the shear-induced axial response (See ref. [72]).

cells to follow the exact same rearrangements [79].

In the quest for new robust disordered metamaterials with low sensitivity to imperfections that retain peculiar desired mechanical functionalities, crumpled structures offer a promising perspective for a designer. Crumpled systems can be considered as disordered systems which show a solid-like behavior. Other categories of disordered solid-like systems are glasses [8], granular systems [80], and densely packed (jammed) emulsions containing a high volume fraction of dispersed phase [81], all of which have tremendous applications in life and technology. Crumpled materials exhibit far from equilibrium properties, and thus similarities with jammed and glassy systems have been mentioned before in literature [11, 82]. However, understanding the mechanical responses of crumpled systems based on glassy dynamics theories is still an open question [83].

In this article, our aim is to show the peculiarities of crumpled systems, and how these can be integrated into mechanical metamaterial design. The structure that we follow in this review is to first show the importance of disordered mechanical metamaterials, with examples present in literature. Then we delve into a specific disordered material, crumpled systems, and review the available literature on crumpled materials and their peculiar properties as disordered solids. We highlight similarities that crumpled materials have with other disordered solids in an attempt to shed light on the understanding of crumpled structures from an amorphous material perspective, and remark how crumpled materials serve also as interesting model systems to understand amorphous materials where the constituents are present at a macroscopic level. Then, we provide an overview of how some of these crumpled structures are already being used for different purposes, and at different length scales. Finally, we provide a connection with mechanical metamaterial design, showing how a bottom-up approach can be used to overcome the difficult to control behavior of purely crumpled bulk materials. Based on the state-of-the-art studies on crumpled systems and disordered mechanical metamaterials we introduce a new concept of crumpled origami material as a robust material with low sensitivity to defects for everyday life applications.

2.2 Mechanical metamaterials: order vs. disorder

Most mechanical metamaterials are usually composed of periodically repeating building blocks that can deform, move or rotate, and together with their spacial arrangements and mutual interactions define the overall response of the material to the applied stresses or deformations [3]. Auxetic materials are among the most well-known mechanical metamaterials. The unique feature of auxetic systems is their negative Poisson's ratio. The Poisson's ratio is the ratio between the perpendicular and the axial strains in the direction of compression, $\nu = -\varepsilon_P/\varepsilon_A$ [84]. Most of the conventional materials have a positive Poisson's ratio meaning that they orthogonally expand/contract in response to a uni-axial tension/compression. Conversely, auxetic materials expand in both orthogonal directions while they are subject to a uni-axial tension. These materials were first observed in the 19$^{\text{th}}$ century, and since then a plethora of work has been dedicated to studying and designing auxetic structures [79, 84–91]. Re-entrant [92, 93] and chiral networks [94] are two examples of auxetic structures, shown in Figure 2.2. The building

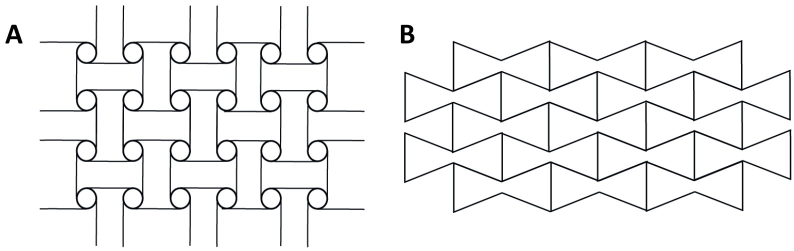

Figure 2.2: Schematic representations of chiral (A) and re-entrant (B) networks.

blocks in a re-entrant structure are bow-tie shapes that can be formed by protruding two opposite angles of a hexagonal honeycomb (Fig. 2.2B). When a horizontal tensile force is applied, the lateral ribs of each cell can move vertically which results in a vertical expansion and consequently, a negative Poisson's ratio [95–97]. On the other hand, chiral networks are composed of bendable ligaments tangentially attached to nodes (Fig. 2.2A). An extensive review on chiral networks has been recently done by Wu *et al.*, [98]. Based on how many ligaments are attached to each node (order of symmetry) different types of chiral tessellations can be formed [99]. Under mechanical loading the ligaments slightly bend around the nodes and, depending on the spatial arrangements of the nodes, this can lead to a negative Poisson's ratio. In addition to re-entrant and chiral tessellations, in recent years advances in additive manufacturing techniques have allowed for other topologies with different stiffness and compressibility to be designed as auxetic materials. These materials exhibit a high indentation resistance [100], which promotes their utility in the production of shock-absorbing structures for many different industrial purposes [95].

The Japanese art of paper folding, origami, has recently attracted much interest in designing mechanical metamaterials with programmable functionality and negative Poisson's ratio [101–104]. Origami structures exhibit exceptional mechanical properties that can be used to tailor the mechanical response and shape of the structure. The importance of origami design for manufacturing metamaterials can easily be seen from the tremendous amount of reviews on the topic in only the last ten years [105–127]. However, highly ordered origami structures have both advantages and disadvantages. The most important advantage is that they are simple to model and relatively easy to customize or manufacture. On the other hand, origami structures, like other ordered metamaterials, are typically constrained by strict geometric relationships and symmetries, which can easily be violated in real-life applications; random dislocations and imperfections introduced during the manufacturing process or under working conditions affect their mechanical functionality [57, 128–130]. The effect that small imperfections have on the performance of Miura-ori origami structures was recently studied [130], and the authors found that random geometric imperfections resulted in large variability of the subsequent performance. At the same time, the imperfections could also be exploited to increase the stiffness [130], and hence might be interesting for tuning the amount of energy stored or dissipated. An extensive body of work is available to describe how the imperfections influence the general response of various ordered metamaterials [96, 131–135]. One should note that the transition from delicate laboratory-level production to industrialized manufacturing and real-life application of metamaterials, requires a certain level of robustness against defects and imperfections. Therefore, designing metamaterials with low sensitivity to randomness and dislocation is of great importance and opens the way for practical metamaterial designs. For this reason, a family of metamaterials has been introduced that intrinsically contain imperfections and these defects can be even employed to improve their functionality [96, 132, 136].

2.3 Disordered mechanical metamaterials

Disordered mechanical metamaterials can be generated through different methods. One strategy is to start from a perfectly ordered structure and rationally introduce topological defects. For instance, in a perfect re-entrant network, we can randomly select some of the unit cells and replace them with conventional hexagonal honeycombs [96]. In another scenario, defects were introduced in a perfect re-entrant tessellation by moving vertices of the cells randomly by a displacement vector [136]. The latter method has been also adapted to form disordered chiral networks [132]. Pozniak *et al.*, [134], had introduced disorder to anti-chiral structures by a stochastic distribution of nod sizes. The degree of randomness and number of defects, of course, will be a determinant factor in the final mechanical parameters of the structure, which has been thoroughly discussed in the mentioned studies. In another study, Meeussen *et al.*, [137], started with an anisotropic triangular network with auxetic properties, since the symmetry of this system can be locally broken by rotating two adjacent unit cells. It was shown that such imperfections can be employed to guide the applied stress or deformations to a complementary part of the network.

A second approach to build randomness in networked materials is based on starting from a completely random structure and employing a correction protocol to adjust a certain mechanical property of the system to the desired level. An example is a system of random nods and springs that are pruned by removing the weakest connections at each level until each node has a maximum of three connections. Simulations have shown that such a system exhibits a negative Poisson's ratio [138]. By determining different bond-removing protocols, one can deliberately introduce a variety of disorders into the system and exploit them to obtain specific mechanical qualities [139–141].

Another family of metamaterials is a perforated system with different shapes of holes and patterns of slits in a lattice of specific symmetry which results in auxetic behavior [86, 142], in some cases even with a very large negative Poisson's ratio (close to -12 for a microporous anisotropic model [143]). Grima *et al.*, [144], showed by randomly orienting cuts in an elastic sheet, auxetic behavior can be easily achieved. This proves that the lattice of specific symmetry is not always needed to harness auxetic behavior. Later, Chaudhary *et al.*, [145], used geometric concepts to design random kirigami (japanese art of paper cutting) 3D structures with different regimes of deformations. They provided scaling arguments describing different regimes by approximating the loaded sheets as a composition of developable units such as cylinders, flats, compressed elasticae, and cones. Their simple approach facilitates the design of novel random kirigami for engineering applications.

Most of the above-mentioned methods of designing disordered metamaterials are based on advanced computation, complicated modeling, and difficult fabrication processes for scaling up. In contrast to these systems, we can consider a completely random structure made by crumpling and confining a thin sheet. In the following, we review interesting properties of the crumpled systems that can be exploited for metamaterial design and explain design principles for using crumpling as a method of designing robust random metamaterials.

2.4 The prospect of crumpled materials

Crumpling of objects is a common phenomenon that happens over a wide range of length scales, from DNA packing inside viral capsids [146] protein folding [147, 148], and crumpled graphene [149, 150], to geological plates [151, 152]. Every day we form crumpled structures by crumpling paper balls [153] or aluminum foils [154]. Our own brains present folded cortices which show similarities with crumpled papers [155], and even the vehicles we use are designed so that, upon impact, the mechanical energy can be dissipated through crumpling to reduce the damage to the passengers [156]. Some examples of crumpled systems are shown in Figure 2.3.

The interest in studying crumpled materials arises from their exceptional properties. These materials present low-density structures; for instance, crumpled papers contain more than 75% air in their structure [13] and often show complex fractal topology [153, 158–164]. Crumpled materials, furthermore, present similarities with cellular materials such as solid foams [165]. For instance, when using crumpled paper for creating low-cost bio-based materials, Martoïa *et al.*, [166], reported the crumpled papers to have mechanical properties similar to those of flexible and rigid

Figure 2.3: (A) Scanning electron microscopy images of crumpled graphene oxide balls. Figure reprinted with permission from ref. [157]. Copyright 2021 Elsevier. (B) Crumpled geological strata. (C) Crumpled flower petals. (D) Butterfly wings still crumpled while leaving a cocoon.

foams. However, contrary to the complicated manufacturing process of cellular materials, crumpling is based on a simple process [167], thus resulting in reduced manufacturing costs [154] to create structures with low density and a remarkable ability to absorb mechanical energy [13, 168–171].

Crumpled structures are often made by deforming elastoplastic sheets while applying a high level of confinement. Elastic plates can deform in

3.2.2 Shear rheology measurements

A standard Anton Paar rheometer (Anton Paar MCR 302, Graz, Austria) with a 50 mm parallel plate geometry was used for applying shear deformation on the samples. After placing the sample in between the plates covered with double-sided tape, the measuring system was lowered to the desired level of compaction. The maximum normal force of the rheometer (50 N) determined also the maximum possible lowering of the probe, achieving a gap which was around the level of compression made with the texture analyzer.

When the probes were positioned, a time sweep at constant amplitude (0.1 % strain) and frequency (1 Hz) was started for 30 min, where further relaxation of the sample occurred. The values of the storage modulus G' after the 30 minutes pre-shear were used as the storage modulus shown in this study. The diameter of some of the paper crumpled disk samples was slightly smaller than the diameter of the plates. For those samples the shear modulus was corrected to G_{real}, defined by [286]

$$G_{real} = G_{app} \left(\frac{R_{app}}{R_{real}} \right)^2, \tag{3.1}$$

where G_{app} is the shear modulus as obtained by the rheometer, R_{app} is the radius of the plates (2.5 cm), and R_{real} is the radius of the crumpled disk as averaged from 10 lateral measurements after compression. Eq. 3.1 was checked with experimental data for polydimethylsiloxane (PDMS) disc samples with known G_{real} (Data provided in Supplementary Information).

After the time sweep, an amplitude sweep with increasing strain (0.01% to 5 %) and constant frequency (1 Hz) was performed to observe the LAOS region, when higher harmonics can affect the oscillatory response [62]. The strain stiffening ratio (S-factor) was used as a quantitative measure in the LAOS regime, and defined as [63]

$$S = \frac{G'_L - G'_M}{G'_L}, \tag{3.2}$$

with $G'_L = \frac{\sigma}{\gamma}|_{\gamma=\gamma_0}$ being the shear elastic modulus at the largest strain and $G'_M = \frac{d\sigma}{d\gamma}|_{\gamma=0}$ the shear elastic modulus at the minimum strain. σ corresponds to the shear stress, γ the shear strain, and γ_0 the shear strain amplitude in the oscillation cycle. The second parameter used is the dissipation ratio (Φ) defined as [67]

$$\Phi = \frac{E_d}{(E_d)_{pp}} = \frac{\pi \gamma_0 G''_1}{4\sigma_{max}}, \tag{3.3}$$

with $E_d = \oint \sigma d\gamma = \pi\gamma_0^2 G''_1$ being the energy dissipated per unit volume within a LAOS oscillation cycle (area within a stress-strain Lissajous plot), and $(E_d)_{pp} = (2\gamma_0)(2\sigma_{max})$ the possible maximum energy dissipated by a perfect plastic material in LAOS. G''_1 corresponds to the first harmonic loss modulus, which is the only one contributing to the total energy dissipation as mentioned in refs. [67, 68].

3.2.3 Compression experiments

The compression of the samples was performed using a texture analyzer TA.XT plus (Stable Micro Systems-SMS, Surrey, United Kingdom) with a circular plate of diameter 50 mm, and 50 Kg load cell. The slow compression (with a speed of 0.1 mm/s) of the samples was confined inside a cylinder with a diameter of 50 mm, to prevent the sample from coming out or expanding more than the diameter of the plate. From the compression of the hand crumpled sheets in the cylinder, an apparent Young's modulus (E_{app}) was obtained as

$$E_{app} = \frac{d\sigma_{app}}{d\varepsilon_H}, \tag{3.4}$$

where σ_{app} is the apparent stress considering the whole area of the plate as the contact area, and ε_H is the Hencky strain. The modulus was calculated from 6 repetitions.

For determining the Young's modulus, E_{mat}, of the different sheets, extension experiments were performed on a ribbon shape sample and analyzed as

$$E_{mat} = \frac{\sigma}{\varepsilon_E}, \tag{3.5}$$

with ε_E being the engineering strain. A rectangular piece of material with dimensions 18x40 mm was fixed between two clamps, and stretched at a speed of 0.01 mm/s. The measurements were performed in triplicate.

3.2.4 Verticality index

We performed a relative quantification of the vertical orientations in the cross-section of a crumpled disc by means of image analysis. The crumpled materials were prepared as indicated in section 3.2.1, and then compressed and hold with a bench vise. The sample was cut at the middle, and the images of the cross-section were collected for further analysis.

A procedure similar to that used in [287] for measuring the alignment of fibers was used here. First, the images were filtered using a Laplacian filter to reduce noise with the *OpenCV.Laplacian* function from OpenCV library [288] in Python. A 2D Fast Fourier Transform (FFT) was then computed on the filtered images using the Python function *numpy.fft.fft2* from the Numpy library [289], resulting in a matrix with the same dimension as the original image, but with the information in the frequency domain (FFT power spectrum). By performing an azimuthal summation across the FFT spectrum, the intensity for each angle was obtained (See Fig. 3.3 as an example). Intensities close to 0 and π radians correspond to repetitive vertical elements, and intensities close to $\frac{\pi}{2}$ to repetitive horizontal elements. The sum of all intensities between 0 to $\frac{\pi}{4}$, and $\frac{3\pi}{4}$ to π was taken as quantification of vertical elements (I_V), and between $\frac{\pi}{4}$ and $\frac{3\pi}{4}$ as quantification of horizontal elements (I_H). A simple verticality index, θ_V, was then defined as a ratio between the vertical and horizontal orientations:

$$\theta_V = \frac{I_V}{I_H}, \tag{3.6}$$

with $\theta_V > 1$ indicating a dominance of vertical (normal to shear direction) orientations, $\theta_V \approx 1$ a similar amount, and $\theta_V < 1$ a dominance of horizontal (parallel to shear direction) orientations. The measurements were performed in triplicate.

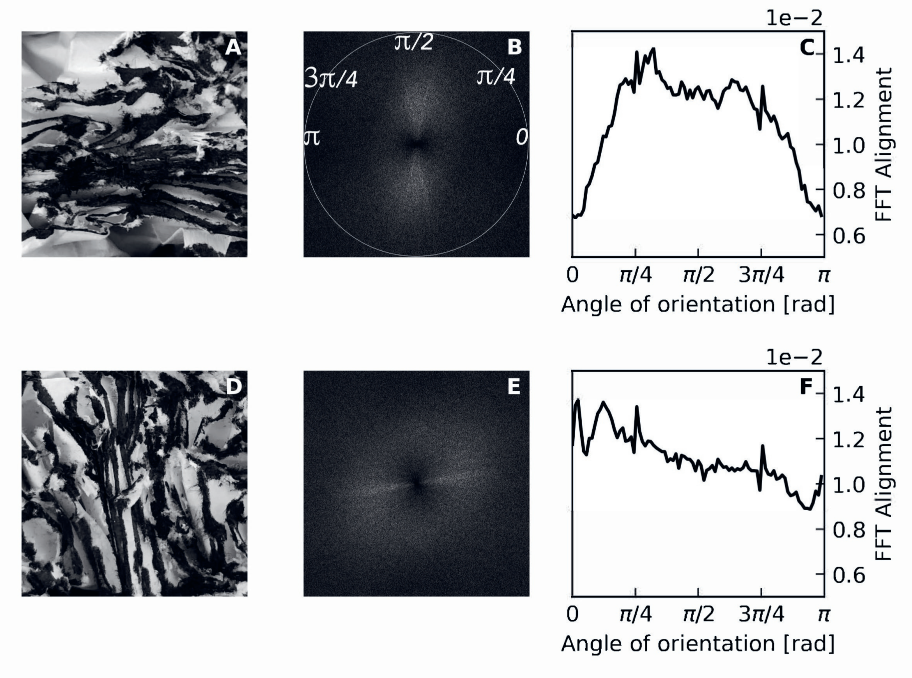

Figure 3.3: Example of middle section of randomly crumpled paper compressed to a disk of 20 mm thickness (A) and semi-random crumpling (D), the corresponding 2D FFT spectrum (B, E), and the alignment plots obtained performing the azimuthal summation (C, F). The height of the peak (y axis) in the 2D FFT alignment plots represents the relative degree of alignment.

3.2.5 Friction measurement

The friction coefficient of the polymeric sheet was measured using the same protocol as van Bruggen *et al.*, [215]. In short, a glass sphere was attached to a rheometer plate. Both the sphere and the bottom plate were covered with the sheet. The upper plate was then lowered until a certain normal force, and then rotated. The torque τ was converted to shear force $F_S = \tau/r$. By using F_S and the normal force F_N, both measured during shear, a friction coefficient was calculated as $\mu = F_S/F_N$. μ exhibits a peak at small deformations, which corresponds to the static friction, μ_s, followed by a slip and a lower plateau representing the dynamic friction, μ_k. Measurements were performed in triplicate.

3.3 Results and discussion

3.3.1 Sheet training and orientation

In Fig. 3.4 the shear storage modulus, G', over the elastic modulus of the sheet, E_{mat}, and the apparent elastic modulus of the crumpled structure, E_{app}, are plotted as a function of the compaction level for the printing paper samples. The compaction level is represented in a dimensionless form based on the ratio of the area of the sheet over the area of the imaginary encompassing cylinder, A/A_{cyl}. Here G' represents the storage modulus; the loss modulus G'' was accounted in the dissipation ratio (see eq. 3.3) and will be discussed later.

In Fig. 3.4A, G' over the Young's modulus of the paper ($E_{mat} \approx 0.9 GPa$) is shown as a function of compaction level. The ratio G'/E_{mat} remains mostly constant with increasing compaction for paper samples, and it shows a slight increase on compaction for trained paper samples. This small dependency of the shear moduli on compaction was unexpected since, according to literature, the force needed to compress crumpled paper balls shows a large dependency on compaction, yielding a scaling with the size of the ball in a power-law manner: $F(\Delta) = \alpha(\Delta/D)^{-\beta}$, where α is a characteristic force coefficient that depends on the bending modulus of the sheet, Δ is the size of the compact object, and D is its initial size [168, 277]. The exponent β depends on material properties, self-avoiding constraints, and dimensionality of compaction [167, 168, 171, 215, 277]. Therefore, the force increases significantly upon compaction, as can be observed also from the $\sigma - \varepsilon_H$ curves in Fig. 3.5A in our experiments. Thus, our findings indicate that the shear modulus is

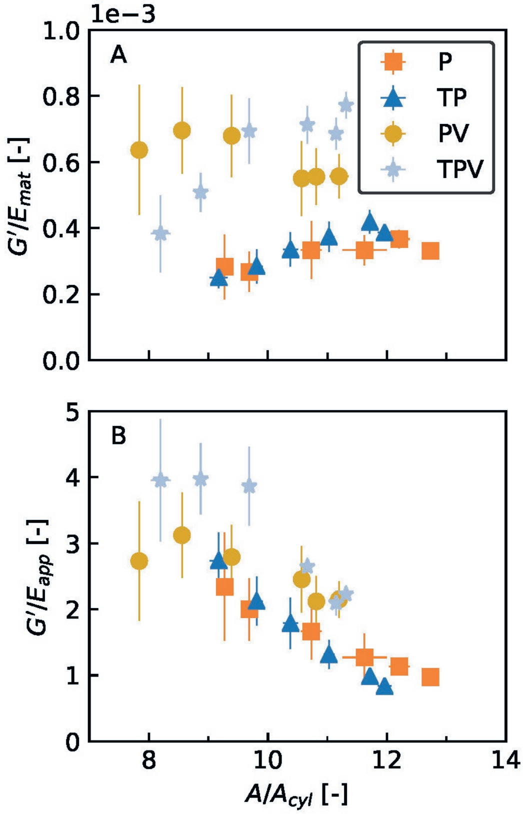

Figure 3.4: (A) Storage modulus (G') over the elastic modulus of the material (E_{mat}), and (B) storage modulus over the apparent elastic modulus (E_{app}) of the crumpled structure for paper samples at different compaction levels (A/A_{cyl}). P: Paper, TP: Trained Paper, PV: Paper with Vertical layers, TPV: Trained Paper with Vertical layers.

not as sensitive to compaction as the compression modulus is. A consequence of this is that the ratio G'/E_{app} decreases monotonically as the compaction increases for the paper samples (Fig. 3.4B). Although these two moduli have the same order of magnitude, G' is larger than E_{app} for low compaction levels and it becomes almost the same as E_{app} at the highest compaction. The results are unexpected, as the shear modulus rarely is larger than the compression modulus for most materials. This exemplifies the interesting properties of crumpled materials for developing new applications. Furthermore, the level of compaction allows for tuning the ratio between the shear and the compaction modulus.

For an isotropic bulk material in small deformations, the shear modulus is defined as [71]

$$G = \frac{E}{2(1+\nu)}, \tag{3.7}$$

where the Poisson's ratio ν ranges from 0-0.5 for most conventional materials, and therefore the shear modulus G should be lower than Young's modulus E. When $G > E$ [249], the above relation predicts a negative Poisson's ratio for the material and the material is known as an auxetic material. The auxetic property is considered as a peculiar property and is mostly observed in rationally designed metamaterials [290]. Auxetic materials often expand perpendicular to the direction of extension. Expansion and lateral unfolding of a crumpled ball while stretching perpendicularly is a signature of auxetic property, which has been observed experimentally [245]. Such an inhomogeneous unfolding was also observed while stretching crumpled balls, from two sides due to long-range correlations [247]. For our crumpled samples, using G' instead of G, and E_{app} as E in eq. (3.7) predicts a Poisson's ratio ranging from -0.9 to -0.3 with increasing the compaction level. However, it is important to mention that eq. (3.7) is valid on isotropic materials, and can only be used to have a rough estimation of the Poisson's ratio of crumpled systems. A negative Poisson ratio of $\nu \sim -0.65$ was also reported in literature for crumpled samples with a relative density (ρ_0/ρ_S) of 0.05 upon unloading [165], where ρ_0 is the sample density and ρ_S the bulk material density. Only at $(\rho_0/\rho_S) > 0.15$ ν was reported as positive [165]. In our crumpled paper experiments, (ρ_0/ρ_S) ranged from $\sim 0.1 - 0.4$ with only negative Poisson's ratios going from -0.9 to -0.3 with increasing compaction. Even though the Poisson's ratios estimated by eq.

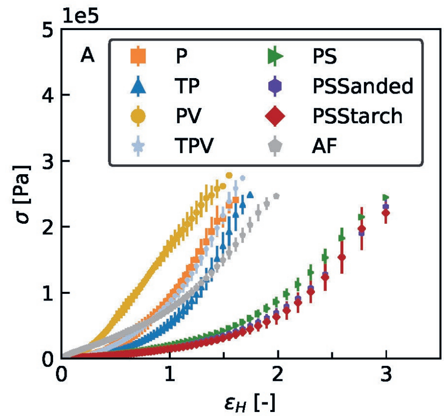

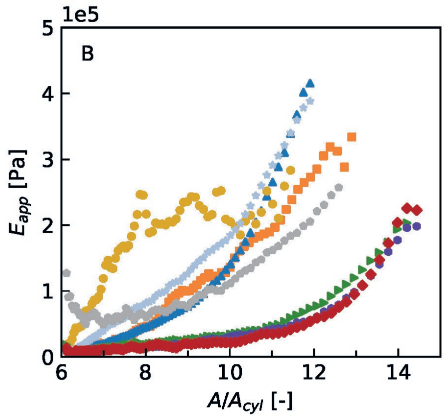

Figure 3.5: (A) Stress (σ) as a function of strain (ε_H) in uniaxial compression, and (B) apparent elastic modulus (E_{app}) for the compaction level (A/A_{cyl}). P: Paper, TP: Trained Paper, PV: Paper with Vertical layers, TPV: Trained Paper with Vertical layers, PS: Polymeric Sheet, PSSanded: Polymeric Sheet Sandblasted, PPStarch: Polymeric Sheet Starch-coated, AF: Aluminum Foil.

(3.7) are only rough estimations and have to be taken with caution, they clearly reflect the auxetic nature of crumpled materials. Recently, disordered mechanical metamaterials have been fabricated using 3D printing, so that a negative Poisson's ratio could be achieved for efficient stress distribution [255]. Mechanical metamaterials with the negative Poisson's ratio have been also designed for cushioning and vibration damping applications [254]. Therefore, our results remark the possible use of crumpled (disordered) mechanical metamaterials with a negative Poisson's ratio as viable options for mechanical energy absorption applications.

The differences in the magnitude of G'/E_{app} between paper and trained paper experiments are small and within the experimental error bars (Fig. 3.4B). However, for trained paper, the G' show a slight increase with increasing A/A_{cyl}, while for the paper without training, data points are scattered and do not show a clear trend with increasing A/A_{cyl} (Fig. 3.4A). This is most likely due to the presence of long-range correlation in the crumpled paper without training. Long-range correlations were also shown to guide the complex unfolding of crumpled balls [247]. These correlations are reduced for the trained paper, where a network of creases is extensively developed by successive crumpling-unfolding [177]. In the study by Gottesman *et al.*, [291], the authors demonstrated that the total crease length that increases upon subsequent compactions can capture the crumpling dynamics. To have an increase in the total length of the creases, new creases should be created by folding previously flat facets over subsequent compactions or repeated crumpling. By folding large facets, long-range correlations in the structure will be reduced. The increase in the total crease length is significant for ≈10-15 times unfolding and crumpling, and then approaches a saturated value [291]. More steps of crumpling and unfolding would result in small changes in the facet sizes, and therefore smaller differences in their mechanical response. Crumpling and unfolding the paper many times can also cause fracture formation, which we wanted to avoid. Therefore, in our study, we crumpled and unfolded the paper 10 times, and compared the mechanical responses of this system with a paper that is crumpled only once. A schematic representation is included in Fig. (3.6), where for paper without training, the network of creases due to plastic deformations is less developed (Fig. 3.6A). When the paper is trained, the network of creases is much more developed, with no remaining big facets and thus having no creases that span a long distance, capable of holding the stress (Fig. 3.6B).

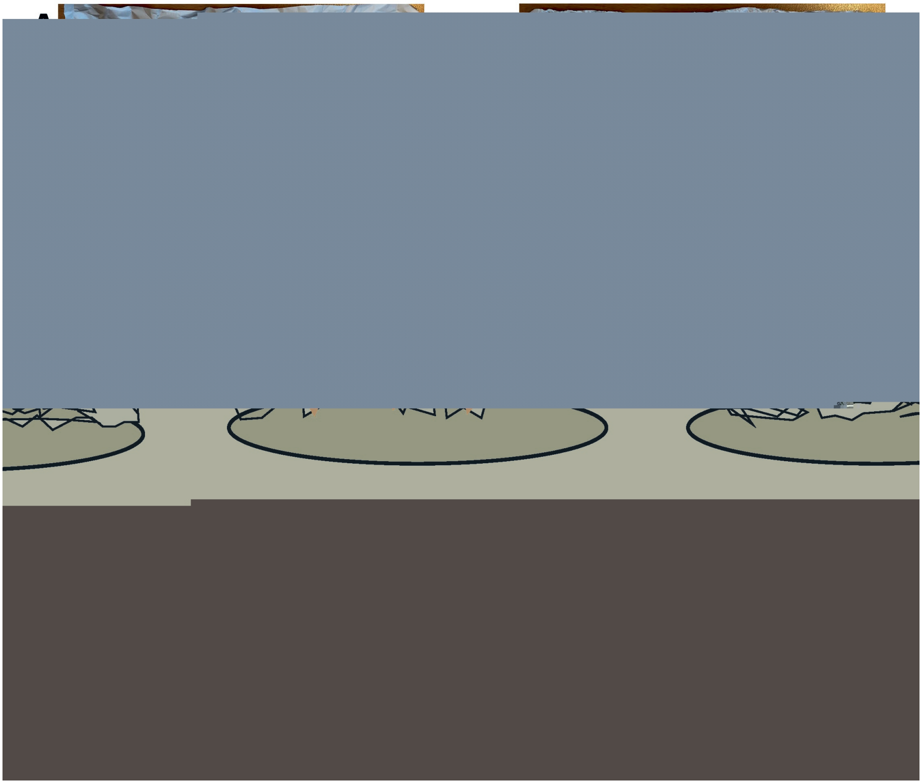

Figure 3.6: Schematic representation of the long-range correlations resulting in force chains for (A) paper without training, having less and larger creases, and (B) trained paper, having a well-developed network of creases.

Regarding the internal orientation, the semi-random crumpling with more layers perpendicular to the shear plates results in higher G' (Fig. 3.4B). Equivalently, more layers with parallel orientation to the shear direction results in higher dissipation through friction and lower G'. The presence of layers positioned vertically in the semi-random crumpled pa-

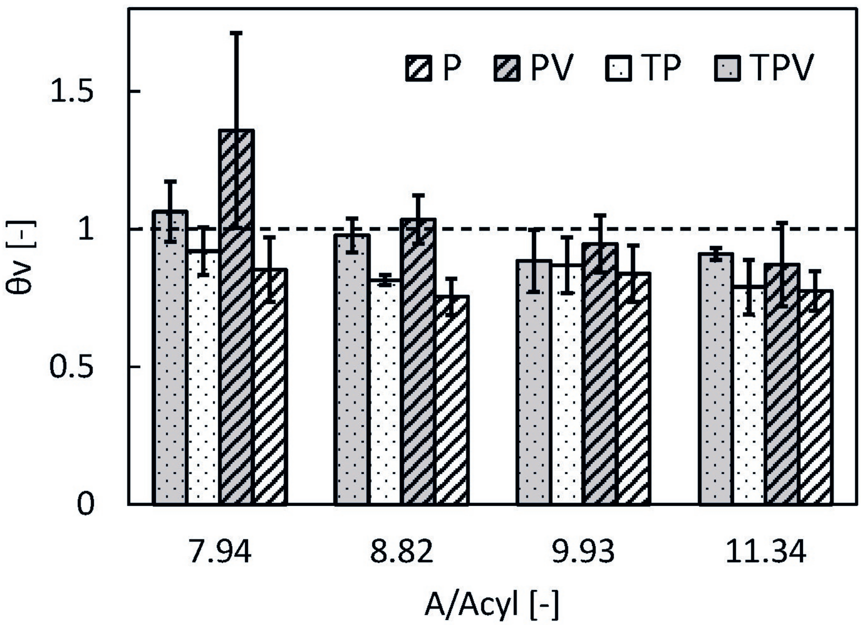

Figure 3.7: Verticality index θ_V of paper and trained paper with the different layer orientations. P: Paper, PV: Paper with Vertical layers, TP: Trained Paper, TP: Trained Paper with Vertical layers.

per is confirmed by doing image analysis of the material's cross-section after cutting and using the verticality index θ_V (eq. 3.6). The difference is more noticeable at the lower A/A_{cyl} values of 7.9 and 8.8 for the semi-random crumpled samples, with $\theta_V \sim 1$, indicating a large intensity for vertical orientations in the sample. For samples with higher compaction (A/A_{cyl} between 9.9 and 11.3) $\theta_V < 1$, indicating that orientations parallel to the shear plates are dominant. For randomly crumpled samples, $\theta_V < 1$ over the whole range of compression, indicating formation of layers parallel to the plates even at small compression levels. These results further confirm the previous findings by Cambou and Menon [258, 259] and Lin *et al.* [256] on the existence of nematic (stacked) domains inhomogeneously distributed, even at volume fractions as low as 8-20% [259]. The presence of stacking domains in the crumpled paper was observed also experimentally when creating low-cost bio-based materials [166]. Furthermore, simulation of crumpled balls with sticky adhesive layers predicted the occurrence of more ordered lamellar patterns [260], due to significant self-contact and self-folding [261].

Even though from the image analysis, the dominance of vertical orientation characterized by $\theta_V > 1$ does not happen at larger compression levels of $A/A_{cyl} = 9.9$ and 11.3, θ_V is still larger than the randomly crumpled samples (within experimental error). This indicates that even at large compression levels, the structures in semi-random crumpled samples show fewer stacked layers in the direction of shear than the random crumpled samples. Because of that, the semi-random samples exhibited a larger G' than the randomly crumpled samples over the whole range of A/A_{cyl} (Fig. 3.4A).

For samples with more layers parallel to the shear direction it is expected that a higher dissipation of energy through friction occurs, which will be more pronounced for larger deformations. In Fig. 3.8 the dissipation ratio, Φ as defined by Ewoldt *et al.*, [67], in strain sweeps is plotted as a function of the shear strain and compaction level. It is important to note, that for the larger A/A_{cyl}, some samples could not reach the imposed shear strain of 5 % due to the maximum torque limit of the rheometer, and therefore the data points stop before strain of 5 %.

For all paper samples, with increasing shear strain, the dissipation increased. A larger deformation implies that either the samples yield by creating new creases, or that the layers slide over each other, dissipating energy via friction. For the samples which were randomly crumpled and contained more layers parallel to the shearing plates (Fig. 3.8A,B), the dissipation increases with the compaction, ranging from $\Phi \sim 0.23$ to 0.33 for paper, and from $\Phi \sim 0.18$ to 0.27 for trained paper, for small strains. The increase of dissipation by compaction is due to the fact that the contacts and forces between sliding layers increase by compaction, and thus more energy is dissipated through friction even at small strains. When the samples are semi-randomly crumpled (Fig. 3.8C,D), the presence

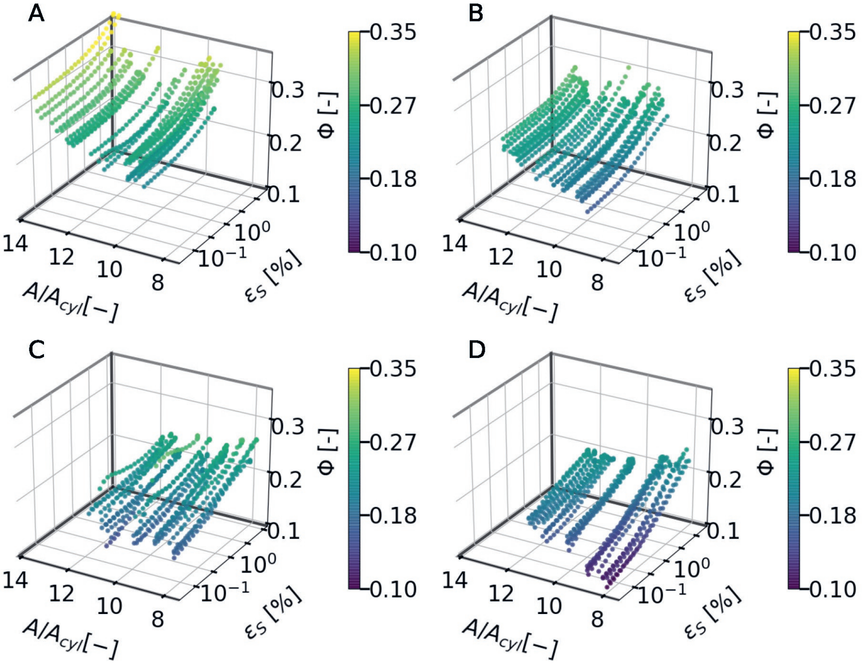

Figure 3.8: Dissipation ratio (Φ) as a function of shear strain (ε_S) and compaction level (A/A_{cyl}) for paper (A), trained paper (B), paper with vertical layers (C), and trained paper with vertical layers (D).

of layers with orientation normal to the shearing plates resulted in less sliding and lower dissipation ratios, while the storage modulus was larger (Fig. 3.4A). Here, applying a shear deformation on the structures with more layers perpendicular to the shear direction, tilting and bending of the vertical layers is induced, resulting in larger G' and lower dissipation. In micro and nano systems such as fluids containing glass fibers [292], carbon nano-tubes [293], and flexible fibers [294], reorientation of the micro-structures parallel to the shear field reduces the resistance to shear. This is similar to what we observe in crumpled systems with layers parallel to the shearing plane exhibiting a lower G'.

3.3.2 Effect of friction

To unravel the effect of friction on shear resistance of crumpled systems we used polymeric sheets with modifications to achieve different friction properties. We chose polymeric sheets, instead of paper or aluminum, to study the effect of friction because polymeric sheets exhibit the least plastic response compared to paper and aluminum, and their friction coefficient changes significantly by treatment with a powder, allowing us to disentangle the effect of friction from plasticity. We measured the friction coefficient of the polymeric sheet without any treatment, after sandblasting, and after starch powder treatment. The results are shown in Table 3.1, including the static μ_s and dynamic μ_k friction coefficients. In Fig. 3.9 the ratios G'/E_{mat} and G'/E_{app}, are plotted as function of A/A_{cyl} for these samples. Contrary to the paper samples, for the polymeric sheet samples the σ requires a larger ε_H before it increases noticeably (Fig. 3.5). This translates in the E_{app} being much lower at A/A_{cyl} values comparable to the paper samples. At the same time, the G'/E_{mat} increases linearly with A/A_{cyl} (Fig. 3.9A).

Table 3.1: Static and dynamic friction coefficients for the polymeric sheet (PS), sanded polymeric sheet (PSSanded) and starch coated polymeric sheet (PSStarch).

Sample	**Static friction μ_s**	**Dynamic Friction μ_k**
PS	0.70 ± 0.14	0.49 ± 0.05
PSSanded	0.60 ± 0.03	0.38 ± 0.05
PSStarch	0.18 ± 0.02	0.15 ± 0.01

As a result, the G'/E_{app} for polymeric sheets exhibits a non-monotonic decrease, with a maximum peak at A/A_{cyl} between 9 and 10. Once the E_{app} increases, the G'/E_{app} shows the same decreasing trend as the paper samples (Fig. 3.4). The higher values of G'/E_{app} compared to paper samples result in estimated ν (based on eq. 3.7) ranging from -0.97 to -0.91 with increasing A/A_{cyl}, indicating an even more pronounced auxetic behavior for polymeric sheets than paper.

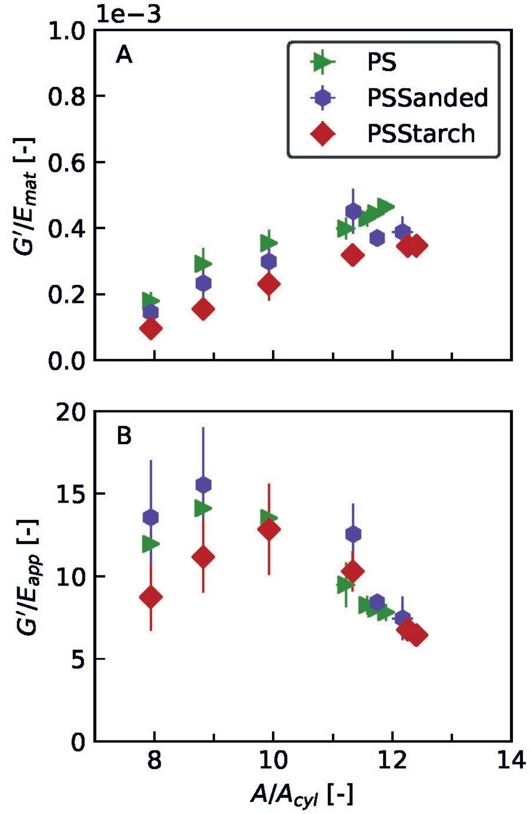

Figure 3.9: (A) Storage modulus (G') over the elastic modulus of the material (E_{mat}), and (B) storage modulus over the apparent elastic modulus (E_{app}) of the crumpled structure for polymeric sheet samples at different compaction levels (A/A_{cyl}). PS: Polymeric Sheet, PSSanded: Polymeric Sheet Sandblasted, PSStarch: Polymeric Sheet Starch-coated.

By applying a starch coating, both μ_s and μ_k greatly decreased. Surprisingly, sandblasted samples, also show smaller friction coefficients compared to non-treated samples. This can be attributed to microparticles being formed during sandblasting, which lubricate the movements of layers. As shown in Fig. 3.9 the starch coating resulted in a decrease of both G'/E_{app} and G'/E_{mat}, demonstrating that friction plays an important role in the shear resistance of crumpled systems. Alternatively, it is shown when the adhesion of a PDMS crumpled system is increased by adding a sticky coating, the compression modulus increases both in experiments and in simulations [260]. This is complementary to what we observed here, as by decreasing the friction, we observed lower E_{app} (Fig. 3.4B), as well as the lower G'/E_{app} (Fig. 3.9B). This means that an easier sliding of the material results in lower moduli both in compression and shear. Previous numerical studies have also predicted that plasticity and friction [188, 189], resulted in less effective packing with respect to pure elastic frictionless crumpling [187]. This is mostly due to easier movement of energy-focusing regions in frictionless sheets, thus minimizing their energy more easily by rearrangements. It was also observed experimentally that the bending energy increases slower than the predictions due to local relaxations in the form of rearrangements of energy-focusing regions [190]. Van Bruggen *et al.*, [215] also observed higher energy storage and less rearrangement in high friction samples, compared to starch coated crumpled samples. In general, lower friction facilitates sliding between layers and rearrangement of the layers which results in lower shear strengths and lower elastic energy.

In Fig. 3.10, the dissipation ratio and strain stiffening factor (S-factor) are plotted as function of compaction level. Interestingly the dissipation ratio Φ does not change appreciably for the samples with different friction coefficients. The starch coated samples exhibit a low friction coefficient (cf. Table 3.1), but a dissipation ratio equal to the high friction samples. From energy conservation this means that more rearrangement events must occur.

In order to further study the response in LAOS, the S-factor was used. This is used to look at the raw oscillation data, as the typical plots for amplitude sweeps show storage (G') and loss (G'') modulus as a function of strain obtained only from the first harmonic. The S-factor is a measure for the intracycle strain stiffening or softening. This may give additional information to the overall strain behavior in typical am-

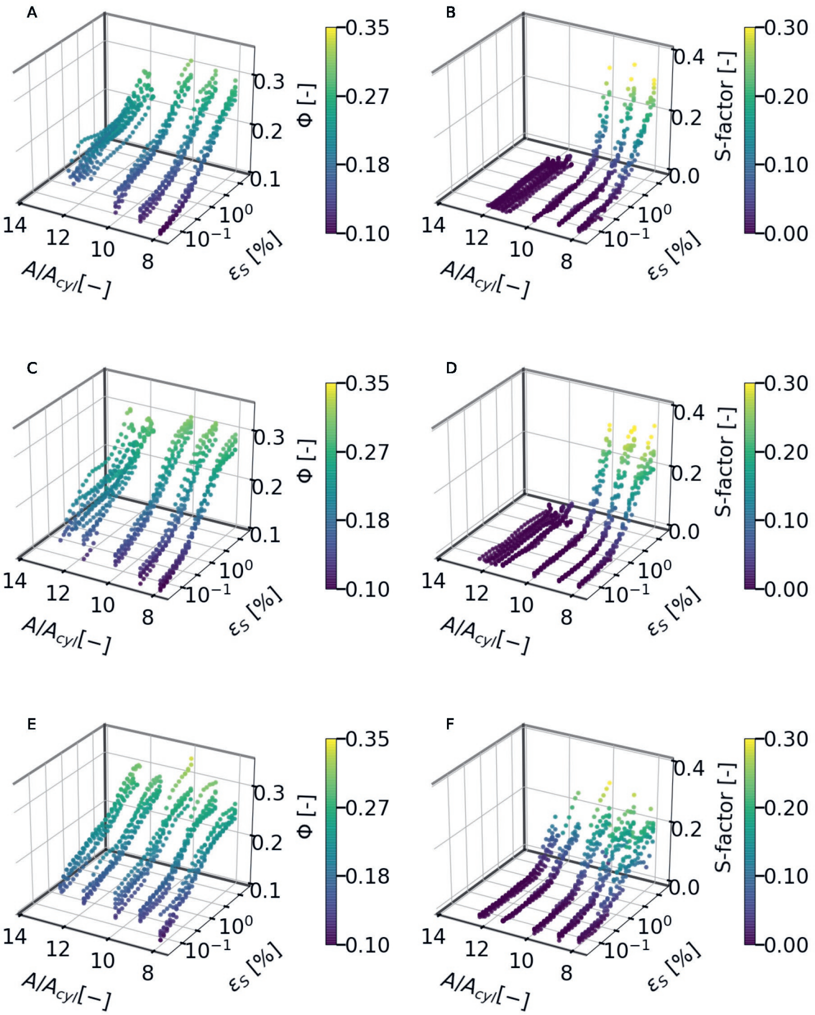

Figure 3.10: Dissipation ratio (Φ, left figures) or S-factor (right figures) as function of shear strain (ε_S) and compaction (A/A_{cyl}) of polymeric sheet (A-B), sand blasted polymeric sheet (C-D), and starch-coated polymeric sheet (E-F).

plitude sweeps plots in the form of higher harmonics [63]. When looking at the S-factor in our samples, we observe values around 0 at low strains. This is characteristic of the sample being in the linear viscoelastic regime, where the $G'_L = G'_M = G'$. As the strain increases, the S-factor values become positive, meaning that there is intracycle strain stiffening. Intracycle strain stiffening has been observed before, for instance, in colloidal glasses [295], gelatinized crosslinked starch [296], and debranched waxy rice starch [297].

The S-factor shows a similar increase for both untreated and sandblasted polymer sheets (Fig. 3.10B,D) at $A/A_{cyl} < 10$, and did not increase at $A/A_{cyl} > 10$ due to reaching the maximum torque. However, there is a noticeable change for the lowest friction sample (starch-coated, Fig. 3.10F). In this case, the S-factor starts increasing already at lower strains than for the other samples. In other words, already at smaller strains, the sample exhibits intracycle strain stiffening. The stiffening in crumpled materials arises from the stretching of the planar facets within the crumpled structure. An explanation for the earlier onset of strain stiffening for the starch coated, low friction sample, could be that in this case, less energy has to be overcome before a stretching deformation occurs. Another reason for an early onset of strain stiffening is that the material contains less creases due to a better packing with the low friction allowing for rearrangements [189, 215, 277]. For crumpling of 2D macro-molecular sheets, it is also reported that an increase in self-adhesion results in a less efficient packing [262], which is not only in line with our findings, but also suggests the validity of these results at much smaller length scales.

We note that the starch low friction sample can rearrange even at high compaction levels, and show stiffening, while higher friction samples do not show any rearrangements (cf. 3.10 F versus B and D, respectively). This is due to the fact that in the experiments with untreated and sandblasted samples a maximum torque was reached during the experiment, and that this torque was not large enough to induce rearrangements.

3.3.3 Effect of plasticity

In this section, we compare the results for different materials to understand how the plasticity of the material can affect the shear strength of a crumpled system. In Fig. 3.11 G'/E_{mat} and G'/E_{app}, are plotted as function of A/A_{cyl} for paper, polymeric sheets, and aluminum foil; all randomly crumpled, without training nor modifying the friction properties. The ratio G'/E_{mat} is also plotted as a function of the normal force (NF) measured by the rheometer at the moment of shearing. The three samples have different material properties such as elasticity and plasticity/ductility. The polymeric sheet exhibits less plasticity than paper and aluminum foil. The elastic modulus of aluminum foil, as obtained from literature, is $E_{mat} = 69GPa$, about an order of magnitude larger than that of paper and polymeric sheets with, $E_{mat} = 0.9GPa$ and $E_{mat} = 1.2GPa$, respectively. According to Fig. 3.11B, G'/E_{app} for aluminum foil falls in between those of the paper and polymeric sheet. Aluminum foil exhibits a monotonic decrease upon increasing compaction, similar to paper. In contrast, a polymeric sheet, with its very low ductility, shows a non-monotonic trend for G'/E_{app} as a function of compaction. This can be attributed to the low E_{app} of crumpled polymeric sheets at low compaction levels, as noted already above 3.3.2.

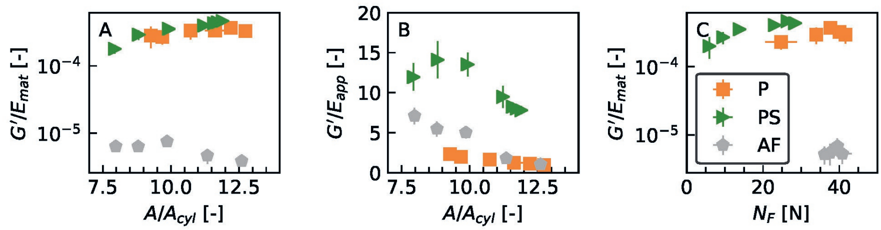

Figure 3.11: (A) Storage modulus over the elastic modulus. (B) Storage modulus over the apparent elastic modulus of the crumpled system. (C) Storage modulus over the elastic modulus of the material as a function of the normal force measured by the rheometer during determination of G'. P: Paper, PS: Polymeric Sheet, AF: Aluminum Foil.

3

When considering the effect of the Young's modulus of the material, we observe that the aluminum foil shows a much lower G'/E_{mat} compared to the other materials (Fig. 3.11A), caused by high E_{mat}. G' of the aluminum foil slightly decreases by increasing the compaction, in clear contrast to the increase for the polymeric sheet and a non-changing value for the paper (Fig. 3.4). The behaviour of aluminum foil and paper is suspected to be caused by the presence of long-range correlations that hold the stress independent of compaction level. In ref. [277] a number between 0 and 1 is introduced as a foldability index representing the degree of ductility of the material. The foldability index is lower when the material is less ductile. The foldability index was quantified for aluminum foil, printing paper, and mylar sheets as 0.86, 0.74 and 0.55 respectively [277]. Since the three materials used in our study are of the same type we assume that the reported foldability indexes hold for our work.

In numerical simulations, Tallinen *et al.*, [189], found that the relaxation of deformation towards a lower energy minimum is hampered by plasticity. In turn, this results in a less effective packing, i.e. a lower fractal dimension. It also leads to a more heterogeneous structure, and likely to more force chains, analogous to those found in granular materials [298]. Although the presence of force chains in granular materials is well known, these chain forces have been reported recently for other types of materials, such as topologically interlocked assemblies [299], or disordered heterogeneous materials consisting of fiber networks [300] or extracellular matrix bridging cells [301]. We thus expect that in our aluminum foil and paper samples more force chains would arise than in a polymeric sheet (See scheme in Fig 3.6 made for paper). Visualization experiments during the shear deformations would be a direct method to confirm the presence of such force chains. Unfortunately, we were not able to visualize the force chains in our systems. To find indications for the presence of the force chains in our structures, the shear modulus G'/E_{mat} was measured and plotted as a function of the normal force as measured by the rheometer during the shear deformation (Fig. 3.11C). For both paper and aluminum foil, all the G' values are measured at high normal forces and show very little dependence on the compaction. This is not the case for the polymeric sheet, where G' monotonically increases by increasing the normal force, due to the lack of force chains that would hold the stress and keep the normal force high. We conclude that force chains are likely to be present in the case of aluminum foil and paper, and not in a polymeric sheet. It is important to note that the materials used here had different thicknesses: paper = 100 μm, polymeric sheet = 30 μm, and aluminum foil = 20 μm. It is shown that the crumpling force scales with the thickness of the plate in a quadratic way [277]. Therefore, the effective stiffness of the crumpled structure is scalable with the thickness of the sheet. However, the crumpling exponents and general behavior do not change [277]. Besides, dimensionless parameters such as G'/E_{app} are independent of the thickness of the sheet. We believe that, while differences in the thickness of our samples would affect the overall magnitude of the response, this would not affect the trends that we observe, nor our interpretation of the results.

3.4 Conclusions

In conclusion, we investigated the shear response of different crumpled materials at different compaction levels, using oscillatory rheology measurements. We compared the shear resistance with the compression stiffness. In contrast to compaction stiffness, the shear modulus is not very sensitive to the compaction level. Although these two moduli have the same order of magnitude, often the shear modulus is larger than the stiffness modulus at low compaction levels, and they become comparable at high compaction levels. In addition, we estimated the Poisson's ratio of crumpled systems which shows an auxetic nature. The effect of training, orientation, friction and plasticity on the shear response were studied systematically. We found that the shear response is affected by all parameters. Some of these parameters are largely omitted in other crumpled material studies, such as friction and internal orientation of the stacked layers.

The effect of training and internal orientation was studied using regular printing paper. By randomly crumpling the paper balls, the structure revealed stacked layers parallel to the shear direction, which resulted in lower resistance to shear, and higher energy dissipation through internal sliding, compared to semi-random crumpled samples. By training the paper through folding-unfolding, the samples exhibited a more clear increase in G' with increasing compaction, which is likely the result of less long-range correlations compared to paper without training (due to the more developed network of creases).

The effect of internal friction in the crumpled sample was studied by treating a polymeric sheet with sandpaper and applying a starch coating. We greatly reduced the friction with the starch coating, which resulted in a lower G' while at the same time not increasing the dissipation. The lower friction allowed for more internal rearrangements in the sample, and was argued to result in strain hardening behavior.

These results further deepen the current knowledge of crumpled materials, which so far have been studied only under compression or extension experiments. By changing the different parameters, including compaction level and orientation of layers the ratio of shear-to-compression response can be tuned. This is important in developing new robust crumpled materials for shock-absorbing applications or designing sustainable lightweight packaging materials to reduce manufacturing and recycling energy costs.

3.5 Supplementary Material

The calculation of the real complex modulus G^* for sample with a radius smaller than the radius of the plate was done as [286]

$$G_{real} = G_{app} \left(\frac{R_{app}}{R_{real}} \right)^2, \tag{3.8}$$

where G_{app} is the shear modulus as obtained by the rheometer, R_{app} is the radius of the plates, and R_{real} is the radius of the sample.

To check the validity of this correction with experimental data we used two polydimethylsiloxane (PDMS) discs with two different diameters and measured their shear modulus using a 25 mm diameter plate-

plate geometry. One of the disc has the same diameter as the plate geometry and the other one has a diameter of $20mm$. We used the above equation to recalculate the shear modulus of the smaller disc and compared it with the value found for the larger disc. The results are shown in Figure 3.12 where measured and corrected values of G^* are shown as a function of the ratio of radius of the sample over radius of the disc.

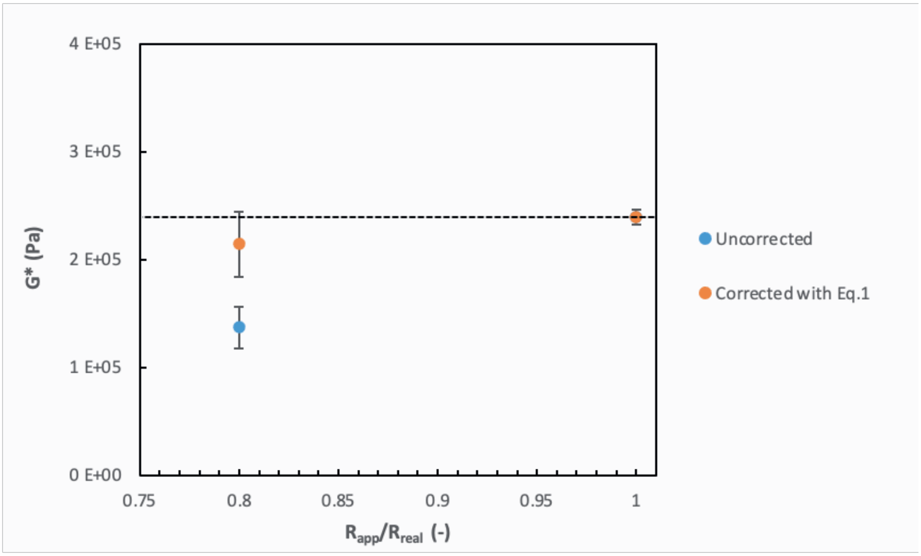

Figure 3.12: Complex modulus G^* as function of the ratio of the sample radius over radius of the plate, for apparent (blue) and corrected (orange) data. Dashed black line shows the value of G^* of PDMS as measured for the sample with the same radius as the radius of the plate.

As the G^* of the PDMS is the same for both samples, the corrected value should be comparable to the value measured for the larger disc in the range of experimental error bars. The horizontal dashed line represent the real G^* of the PDMS. Without any correction, the shear modulus reported by the rheometer for the smaller sample was greatly underestimated (blue data point) due to the consideration of a full plate by the rheometer for calculating the modulus. The slight deviation and the experimental error are expected to be from the small deviation between the position of the center of the disc respect to the center of the plate upon loading the samples. There is no wall slip effect due to strong adhesiveness between PDMS and steel plates.

Chapter 4

Universal Transition to Wide Shear Zones in Entangled Macroscale Chains or Ropes

This chapter has been submitted as:
Shaebani, M. R.*, **Giménez-Ribes, G.**,* Zondervan, S., Sagis, L. M. C., van der Linden, E., & Habibi, M. Universal Transition to Wide Shear Zones in Entangled Macroscale Chains or Ropes. *arXiv:2208.13516* (2022)
*Co-first authors

Abstract

Macroscale chains have been proposed to give insight into the physics of molecular polymer systems. Nevertheless, understanding the rheological response of systems of quasi-one-dimensional semiflexible materials, such as bead-chain packings, is currently a great challenge. We study the nonlinear rheology of random assemblies of macroscale chains— including steel bead chains and cooked spaghetti— under oscillatory shear. We show that a universal transition from localized to wide shear zones occurs upon increasing the strain amplitude, for a wide range of lengths, flexibilities, and other structural parameters of the constituent elements. The critical strain amplitude coincides with the onset of strain stiffening development in the system. We obtain scaling laws for transition sharpness, shear-zone width, and stiffness enhancement as a function of chain length. Our findings suggest that the entanglements between the constituent elements strengthen when approaching the critical strain amplitude and rapidly become long range, even spanning the entire finite system for long enough chains. We show that the nonlinear rheological response is governed by the interplay between increasing stored elastic forces due to entanglements and increasing contribution of dissipation with shear rate and interlocking between chains.

4.1 Introduction

Disordered assemblies of long semiflexible objects are a class of materials ubiquitously observed in nature and daily life. Examples are bird nests [302], aegagropila networks [303], and unwoven textiles [58]. An intriguing and important property of such entangled assemblies is their mechanical response and yielding when subject to external stresses. For example, packings of bead chains exhibit a striking strain stiffening under shear [304, 305]. The complexity arises from the presence of topological constraints such as (semi)loops, knots, and interlocking between the constituent elements [18, 33, 305–309]. The behavior differs considerably from that of packings of rodlike objects, where the physics is mainly governed by frictional interactions, volume exclusion, and aspect ratio of rods. Despite the analogies with polymeric materials [310, 311], developing a quantitative theory of stability and unjamming response of macroscale chain assemblies requires a detailed understanding of the roles of entanglements and friction, which is still lacking. The insight from the mechanical response of entangled-driven athermal systems of long semiflexible objects can guide future design of new smart unwoven textiles [312–314], knitted fabrics [315], and artificial mussels and tissues [316].

Upon yielding, slowly sheared packings of individual beads often form rigid regions separated by narrow shear zones near moving boundaries where the material flows with a shear-rate-independent profile shape [317, 318] (though wide shear zones have also been reported when shearing the bulk material away from the boundaries [319, 320]). While shear banding in frictional granular materials can be understood based on energy dissipation considerations [321, 322], much less is known about the yielding of semiflexible chain assemblies, particularly, whether and how far entanglements and chain length and flexibility broaden the shear zones and extend them into the bulk. Since shear zones mark regions of material failure and energy dissipation, understanding the yielding behavior of chain assemblies is crucial in industrial processes and for design of new disordered meta materials [58, 284, 303, 323]. As a daily-life application, by twisting cooked spaghetti on a plate with a fork, an interesting question is how the amount of rolled spaghetti around the fork depends on length, softness, and adhesion of the strands?

The rheological response of viscoelastic materials is of fundamental importance in physics, engineering, and biology. There has been growing interest in nonlinear viscoelastic responses to large strains [324–327], e.g., to differentiate between materials with similar linear but drastically different nonlinear responses.— A highly informative protocol is to apply an oscillatory shear strain [326–328]: After many cycles to become independent of the prior history of the sample, the steady-state stress response can be probed over a wide strain range from below to above the yield point.— Nevertheless, the rheology of macroscale chain assemblies remains less explored [22]. It is unclear how the interplay between topological constraints and dissipation governs the nonlinear rheological physics of these systems.

In the present work, we study the rheological response of bead-chain assemblies to oscillatory shear deformations in experiments and numerical simulations and compare it to that of cooked spaghetti. We observe a striking universal transition from narrow shear zones at small amplitude oscillatory shear (SAOS) to wide shear zones at large amplitude oscillatory shear (LAOS). Increasing the length of the constituent elements sharpens the transition and enhances the extent of the wide shear zone, for which power-law scaling relations are obtained. Our results show that the system undergoes a rather sharp crossover from inactive entanglements in SAOS to system-spanning activated entanglements in LAOS. We demonstrate that the nonlinear rheological physics of macroscale chain assemblies is governed by the competition between stored elastic and dissipative (viscous) forces: The applied shear strain enhances the elastic contribution to stress by strengthening the topological constraints while the contribution of dissipation— which is proportional to the shear rate— grows above the yield point and also with increasing the interlocking between the constituent elements.

Our rheometer setup shown in Fig. 4.1A consists of a cylindrical container of inner radius R and a rotating four-blade vane with blade radius

R_v, which applies a sinusoidal deformation

$$\phi = \phi_\circ \sin(2\pi f t), \tag{4.1}$$

where ϕ is the deflection angle, and $\phi_\circ$ and $f = 0.1$ Hz denote the rotation amplitude and frequency, respectively. As a model material, we use either cooked spaghetti (which is cut into equal pieces) or bead chains consisting of hollow spherical beads with diameter d flexibly connected to each other by enclosing dog-bone-shaped links. The induced gap size ℓ between the neighboring beads varies in the range $0 \leq \ell \leq \ell_{\mathrm{max}}$. The links also limit the local turning angle θ of the chain to $0 \leq \theta \leq \theta_{\mathrm{max}}$; see Fig. 4.1B and *Materials and Methods* section for details. An instantaneous persistence $p = \cos(\theta)$ can be assigned to the chain nodes [329] from which the local persistence length ℓ_p can be obtained via $p = \mathrm{e}^{-\ell/\ell_p}$ [6, 26, 311]. We also perform extensive contact dynamics (CD) simulations [330] of spherical rigid beads in a setup similar to our experiments. We impose upper bounds on the distance between the centers of neighboring beads and on the angle between lines connecting three neighboring beads along the chain. This concept is suited very well to the CD method where interparticle forces are handled as constraint forces [331, 332].

4.2 Materials and methods

4.2.1 Vane rheometer

A rheometer measuring head (Anton-Paar DSR 502, Austria, Graz) was mounted on a vertically moving frame with a digimatic indicator (ID-H Series, Mitutoyo, The Netherlands, Veenendaal) to accurately adjust the height of the probe. A custom made cup, consisting of a 250 mL glass beaker roughened with bead chains, was attached to the bottom plate. A four-blade vane (ST22-4V-40, Serial No.: 18180, Anton-Paar, Austria, Graz) of 22 mm diameter and 40 mm height was used. To record the movements at the top surface, a GoPro Hero 4 Silver camera (GoPro, U.S., San Mateo) was used with a frame rate of 25 frames/s. The probe was first inserted into the cup and secured by hand while loading the sample. To avoid exceeding the maximum torque that the rheometer could apply, the bead chains or spaghetti were loaded into the cup up to 2 cm and 4 cm height, respectively. After loading the spaghetti samples, they were gently pushed downwards without being fractured. For experiments with spaghetti a lid, made of a low-density polyethylene petri dish and secured between an additional layer of chains on the beaker wall, was used to prevent the samples from ascending above the probe. In case of bead chains, the beaker was vibrated for 2 mins on a Vortex-Genie 2 test tube shaker (Scientific Industries, U.S., Bohemia) to reach the maximum possible packing fraction. Next, the probe was connected to the rheometer head and pre-sheared at 1 Hz frequency and 63 mrad rotation amplitude for 4 mins. Finally, the oscillatory shear tests were carried out at 0.1 Hz frequency and over a rotation amplitude range limited by the maximum torque that the rheometer could apply ($\phi_\circ \leq 0.6\,\mathrm{rad}$ for bead chains and $\phi_\circ \leq 1.9\,\mathrm{rad}$ for spaghetti).

4.2.2 Bead chains

Stainless steel granular bead chains (Grootspul, The Netherlands, Driebergen) were used with a bead diameter of 2.4 mm, a maximum distance of 2.8 mm between the centers of neighboring beads, and a maximum turning angle of 40°, resulting in a minimum loop circumference of 9 beads. The bead chains were cut into lengths of 3, 9, and 45 beads, as well as monomers. Sunflower oil (Vandemoortele Nederland BV, The Netherlands, Zeewolde) was used as a lubricant to reduce the friction coefficient to $\mu \approx 0.2$; the chains were coated by shaking them for 10 mins in plastic containers using 0.02 mL of oil per gram of beads.

4.2.3 Cooked spaghetti

Dehydrated dry spaghetti (Jumbo Spaghetti Naturel, The Netherlands, Veghel) were cut into lengths of 1.0, 3.0, 9.0 and 15.0 cm. Excess starch was cleaned by submerging the spaghetti in cold tap water for 10 s twice, while gently stirring using a spatula. The samples were subsequently boiled for 9 mins and cooled in a sieve using running cold tap water. The majority of the water was drained. Next, sunflower oil (Vandemoortele Nederland BV, The Netherlands, Zeewolde) was used as a lubricant; the samples were coated using 0.02 mL oil per gram of boiled spaghetti by stirring and subsequent shaking by hand for 5 mins in a closed plastic container. Due to swelling of the spaghetti during cooking, the final strand lengths were 1.3 ± 0.2, 3.5 ± 0.1, 12.3 ± 0.2 and 19.6 ± 0.2 cm. The spaghetti samples were stored in closed containers at room temperature and measured within eight hours after preparation.

4.2.4 Image processing

Particle image velocimetry (PIV) was performed using PIVlab 2.55 plugin [333], a tool developed for MATLAB R2019b (MathWorks, U.S., Natick). The settings for PIVlab were used as described in [334]. Four passes were applied for PIV estimation with the first being approximately four times and the last about a half of the bead diameter. The images were calibrated for time and space using the time between successive frames and the width of the beaker at the sample surface, respectively.

4.2.5 Simulation method

Simulations of bead chains were performed using the contact dynamics (CD) method [330, 331]. To construct the chains, spherical rigid beads of diameter d were connected to each other by imposing an upper bound on the distance $d{+}\ell$ between the centers of neighboring beads, with ℓ being the gap between the surfaces of the two beads. The maximum gap size $\ell_{\max}$ varied within $0 \leq \ell_{\max} < 0.4\,d$ in different simulations; thus, the gap between beads on the same chain was always smaller than the bead radius to ensure that the neighboring beads remain so close to each other that the imaginary bonds between the beads of different chains never touch. To tune the flexibility of the chains, the angle θ between the lines connecting the centers of successive bead pairs on the chain was limited to an upper bound $\theta_{\max}$ ($\theta_{\max} \in \{20°, 30°, 40°, 50°, 60°, 70°\}$ in different simulations). The bead chain length was varied from $N{=}1$ (individual beads) to $N{=}100$.

4

A layer of beads was fixed at the lateral and bottom walls of a cylindrical container of height $20d$ to provide rough boundaries. The inner diameter of the container was $29d$ and a rotating four-blade vane of diameter $9d$ was constructed by touching rigid beads. The container was first loaded with chains of equal size and relaxed into equilibrium under gravity. Next, the vane was rotated in an oscillatory fashion with 1Hz frequency and $\pi/50$ rad amplitude for 240 s. The oscillatory shear tests were carried out at 0.1Hz frequency and for different amplitudes. The total torque exerted on the vane was measured after each $\Delta\phi$=10^{-3}rad change in the deflection angle.

4.3 Results and discussion

4.3.1 Universal transition to wide shear zones

We start the experiments in the SAOS regime, i.e. with small rotation amplitudes. In this regime, the surface velocity profiles reveal that the movements diminish rapidly with increasing distance from the rotating blades, independent of the chain length N; see e.g. the experiments at $\phi_\circ = 0.063$ rad in *Suppl. Movie S1.* Denoting the mean velocity at the radial coordinate r with $v(r)$, Fig. 4.2A shows that v decays fast with r; a jammed immobile region is reached after 1-2 bead diameter distance. The velocity fluctuations are relatively small and the profiles are reproducible to a large extent independent of the initial conditions. Formation of narrow localized shear zones near moving boundaries was observed in quasistatic shear of granular materials [317, 318]. Here, the independence of the results from N indicates that the topological constraints have not been activated yet and do not play a role in the SAOS regime.

To quantify the extent of the shear zone, we assign a width r_c to the shear zone as the radial distance from the cylinder axis at which the velocity drops below a threshold value; see Fig. 4.2B. Here we report the results for the threshold velocity $v_\mathrm{c} = 4\times10^{-5}$ m/s; however, we checked that the observed trends and our conclusions are insensitive to this choice in a moderate range of velocities.

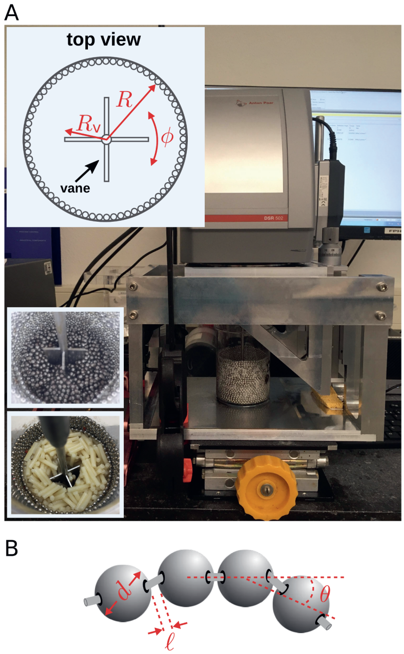

Figure 4.1: Setup and bead-chain geometries. (A) Four-blade vane rheometer setup. Upper inset: top view of the cell, not to scale. $R_\mathrm{v} = 11\,\mathrm{mm}$; $R \simeq 34\,\mathrm{mm}$. Lower insets: images of shear experiments with steel bead chains or cooked spaghetti. (B) Schematic of the bead chain with ℓ and θ indicating the bond length and turning angle, respectively, and $d = 2.4\,\mathrm{mm}$ being the bead diameter. ℓ is variable from 0 to $\ell_{\mathrm{max}} = 0.4\,\mathrm{mm}$ and θ from 0 to $\theta_{\mathrm{max}} \simeq 40°$ in experiments.

The behavior is markedly different in the LAOS regime: The shear zone extends to the bulk of the system, as shown in Fig. 4.2A (see also *Suppl. Movie S1* for experiments at $\phi_\circ = 0.632\,\mathrm{rad}$). It was previously reported that oscillatory shear of granular materials with large amplitudes broadens the shear zone up to a few bead diameters, as the shear stress drops at the shear direction reversals [335]. Our notable observation is the influence of chain length on the shear deformation at large strains: With increasing N, the shear zone becomes much wider, the velocity profile strongly depends on the initial condition, and large velocity

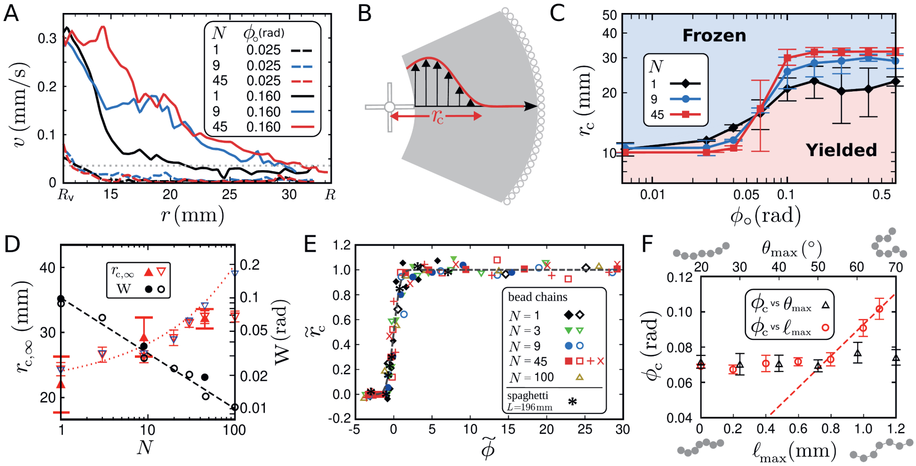

Figure 4.2: Chain dynamics in oscillatory shear. (A) Mean bead velocity v as a function of distance r from the cylinder axis for different values of rotation amplitude ϕ_o and chain length N. The dotted line denotes the threshold velocity v_c. (B) Definition of the shear-zone width r_c. The velocity field is sketched with vertical arrows. (C) Shear-zone width r_c versus rotation amplitude ϕ_o. The yielded and frozen regions for N=1 are indicated with different colors. (D) Saturation width $r_{c,\infty}$ of the shear zone and transition sharpness W (indicating the range of rotation amplitudes over which the transition occurs) in terms of N. Full (open) symbols correspond to experimental (numerical) results. Blue open symbols represent the simulation results for a larger container with $R \simeq 100$ mm. The black dashed line is a fit to Eq. (4.2), and the red dotted line represents a growth according to Eq. (4.3), as a guide to the eye. (E) Collapse of all rescaled shear-zone widths $\tilde{r}_c = \frac{r_c - r_{c,0}}{r_{c,\infty} - r_{c,0}}$ as a function of rescaled rotation amplitude $\tilde{\phi} = \frac{\phi_o - \phi_c}{W}$, obtained for different chain lengths in experiments (full symbols) and simulations (open symbols). The simulation results for a chain with zero bond length $\ell_{max} = 0$ (pluses) or high flexibility $\theta_{max} = 70°$ (crosses) at N=45 are also presented. The dashed line is a fit to the error function (4.4). (F) Transition center ϕ_c versus maximum bond length ℓ_{max} or maximum turning angle θ_{max} obtained from simulations for N=45. The line represents $\phi_c = \ell_{max}/R_v$.

fluctuations along the radial coordinate are observed even for a single experiment.

To understand how the system crosses over from narrow shear zones in SAOS to wide system-spanning ones in LAOS, we vary systematically $\phi_\circ$ for different chain lengths and repeat the measurement for different non-consecutive cycles in each sample to smoothen the velocity fields. The width r_c of the shear zone as a function of $\phi_\circ$ is shown in Fig. 4.2C. Interestingly, the change of r_c when moving from the SAOS to the LAOS regime is not gradual but happens over a narrow range W of rotation amplitudes. For longer chains the transition is sharper, corresponding to a smaller W. By fitting each r_c–$\phi_\circ$ curve to an error function, we assign a W to it. The plot of the resulting W values in terms of N in Fig. 4.2D implies that W scales as

$$W \sim N^{-\alpha}, \tag{4.2}$$

with the exponent $\alpha \simeq 0.5$.

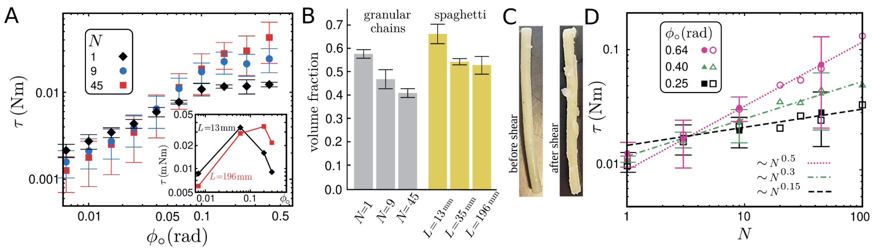

Figure 4.3: Stiffening of macroscale chains. (A) Torque τ versus rotation amplitude $\phi_\circ$ for different bead chain lengths. Inset: τ vs $\phi_\circ$ in shear experiments with cooked spaghetti of length L. (B) Volume fraction of bead chain or spaghetti assemblies. (C) Example of surface roughening of spaghetti due to oscillatory shear. (D) τ versus N for different values of $\phi_\circ$ in experiments (full symbols) and simulations (open symbols). The lines represent power-law fits to $N \geq 3$ data.

Figure 4.2C also reveals that r_c reaches a plateau level at large $\phi_\circ$, which is higher for longer chains. Denoting this maximum shear-zone width with $r_{c,\infty}$, Fig. 4.2D shows that $r_{c,\infty}$ initially grows with N but gradually approaches the inner radius R of the container (full triangles). The saturation behavior at larger N is more visible in the simulation results (red open triangles). The question arises whether the shear zone for long chains can penetrate further into the bulk of the system in an infinite system (i.e. when $R \to \infty$). To answer this, we perform simulations with chain lengths up to $N=100$ and increase the container radius from $R \simeq 34$ to 67 and 100 mm. As the resulting $r_{c,\infty}$ values for the two latter system sizes are the same (within the error bars), we conclude that the shear zones for chain lengths $1 \leq N \leq 100$ cannot be wider if the system size is further increased beyond $R = 100$ mm. A comparison between the results at $R = 34$ (open red triangles) and $R = 100$ mm (open blue triangles) in Fig. 4.2D shows the finite-size effects on $r_{c,\infty}$ values for longer chains. The system-size-independent width of the shear zone (blue symbols) can be approximately described by

$$r_{c,\infty}(N) - r_{c,\infty}(N=1) \sim N^{\beta}, \tag{4.3}$$

with $\beta \approx 0.5$. The radius of gyration of a flexible chain similarly scales with $\sqrt{N}$ [6]. This suggests that in the LAOS regime the topological constraints are fully activated along the entire length of the chains that are moved by the rotating blades. As a result, their motion can influence a bulk region of size proportional to their radius of gyration, i.e., $\propto \sqrt{N}$.

Figure 4.2E illustrates our main result: After proper rescaling, all $r_c - \phi_\circ$ data collapse on a universal curve which is well fitted by an error function. We introduce the rescaled shear-zone width $\widetilde{r}_c = \dfrac{r_c - r_{c,0}}{r_{c,\infty} - r_{c,0}}$, with $r_{c,0}$ being the minimum shear-zone width. Thus, the dimensionless number $\widetilde{r}_c$ takes values in $[0, 1]$. All rescaled shear-zone widths follow a universal master curve

$$\widetilde{r}_c = \frac{1}{2}\Big(1 + \mathrm{erf}\big(\frac{\phi_\circ - \phi_c}{\mathrm{W}}\big)\Big), \tag{4.4}$$

where W is the range of amplitudes over which the transition occurs (transition width) and ϕ_c is the rotation amplitude at the center of the error function (transition center). We checked that the spaghetti data and also simulation results for $1 \leq N \leq 100$ and other values of the maximum bond length in the range $0 \leq \ell_{\max} < d/2$ or maximum turning angle in the range $20° \leq \theta_{\max} < 70°$ are well fitted to Eq. (4.4).

From the fits of r_c–$\phi_\circ$ curves to an error function, we find that the transition center ϕ_c does not depend on N. This can be also seen from Fig. 4.2C; we get $\phi_c \simeq 0.07$ rad by averaging over experiments with different N. Simulations with different values of $\theta_{\max}$ or $\ell_{\max}$ shown in Fig. 4.2F reveal that ϕ_c is independent of the chain flexibility $\theta_{\max}$. Moreover, ϕ_c is insensitive to variation of $\ell_{\max}$ for small bond lengths but grows approximately linearly for $\ell_{\max} \gtrsim 0.8$ mm.

A plausible scenario is that the transition center ϕ_c is the onset at which the shearing brings the bonds between neighboring beads to their maximum possible length $\ell_{\max}$ quickly after each shear direction reversal. Above this threshold rotation amplitude, the chains are in a stretched form in the absence of the internal degrees of freedom of having variable bond lengths. This would lead to the prediction $\phi_c \approx \frac{\ell_{\max}}{R_v}$, i.e. a linear increase of ϕ_c with $\ell_{\max}$. Figure 4.2F shows that this simple model captures the behavior for long bonds. But why does not ϕ_c grow proportionally to $\ell_{\max}$ for short bonds? From simulations with N=1, we observe that a minimum rotation amplitude of the order of 0.06–0.07 rad is required to generate wide shear zones in packings of individual beads. That is why the increase of ϕ_c with $\ell_{\max}$ is only visible for bond lengths $\ell_{\max} \gtrsim 0.8$ mm for which $\phi_c \gtrsim 0.07$ rad.

4.3.2 Stiffening upon increasing strain amplitude

The crossover from narrow to wide shear zones suggests the presence of entanglements above the transition threshold ϕ_c. One of the entanglement mechanisms is the interlocking between the beads of different chains. We expect that stretching of bonds to $\ell_{\max}$ at ϕ_c immediately activates this type of topological constraints for all chain lengths $N \geq 3$. Formation of (semi)loops is another entanglement mechanism, which strengthens with increasing N and/or $\phi_\circ$ above ϕ_c. Note that a full ring requires a minimum chain length N=9. The fact that the shear-zone width rapidly saturates above ϕ_c for all N shows that interlocking is the major entanglement mechanism affecting the flow properties of chain assemblies. Loop formation induces weak entanglements for N<9

4

and, moreover, should lead to $\phi_\circ$-dependent wide shear zones which is not observed. It is however expected that semiloops play the major role in the strain stiffening phenomenon [304, 305].

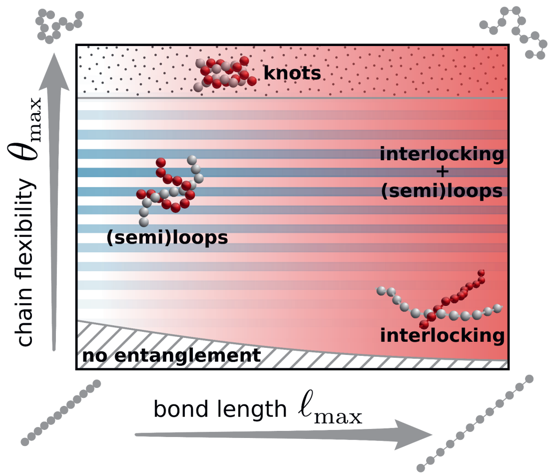

Figure 4.4: Schematic phase diagram of entanglement mechanisms at a given chain length. The contribution of (semi)loops grows with increasing chain flexibility from rod-like chains; however, extremely flexible chains promote knot formation. Increasing bond length gradually enhances the contribution of interlocking between chains. Gradients of red and blue colors qualitatively indicate variations in the contributions of interlocking and semiloops, respectively.

As a direct proof of the activation of entanglements, we probe the mechanical response of the system upon increasing $\phi_\circ$. By measuring the maximum exerted torque τ by the rheometer on the system in an oscillatory shear cycle for a given rotation amplitude $\phi_\circ$ and repeating it for different $\phi_\circ$ values, we plot τ as a function of $\phi_\circ$ in Fig. 4.3A. In the absence of entanglements at small strains, shearing the packings of individual beads (N=1) requires a larger τ compared to long-chain packings, due to having a higher packing fraction; see Fig. 4.3B and Ref. [306] (Although packing structure strongly depends on the interparticle friction [336–338], we assume that it affects the assemblies with different N in a similar way). In contrast, at large amplitude oscillations, yielding occurs for N=1 while assemblies of longer chains exhibit shear stiffening. The crossover point in Fig. 4.3A interestingly coincides with the onset ϕ_c of the transition to wide shear zones. We observe a similar transition point and mechanical response trend in the case of spaghetti (inset of Fig. 4.3A), even though they cannot sustain large torques in the strain stiffening regime: Large amplitude shear of spaghetti leads to roughening of strand surfaces (Fig. 4.3C), cutting of strands into shorter pieces, and ascending and ordering of strands above the probe. Moreover, it was previously reported that shear rate (which increases with $\phi_\circ$ in our experiments) and interfilament overlap length enhance the sliding friction between filaments [339]. Nevertheless, observing a similar onset of stiffening for bead chains and spaghetti is striking and it possibly points to a universal mechanical response of assemblies of long semiflexible objects.

Figure 4.3A shows that the degree of stiffening not only depends on $\phi_\circ$ but also on N [304]. When plotting τ vs N for different $\phi_\circ$ in Fig. 4.3D, we find that τ scales as a power-law with the chain length (for $N \geq 3$)

$$\tau \sim N^{\gamma(\phi_\circ)}. \tag{4.5}$$

The exponent γ depends on $\phi_\circ$; it increases from $\gamma = 0$ at $\phi_\circ = \phi_c$ and reaches, e.g., $\gamma \simeq 0.5$ at $\phi_\circ \simeq 0.64$ rad. By varying $\ell_{\max}$ in simulations from 0 to $\sim d/3$ to increase the contribution of interlocking, we find a nearly 20% increase in τ, reflecting the greater contribution of semiloops to the mechanical response. For a given chain length, Fig. 4.4 summarizes the effective entanglement mechanisms in the ($\ell_{\max}$, $\theta_{\max}$) space, i.e. upon varying chain flexibility and interparticle bond length.

4.3.3 Nonlinear rheological response

To clarify the similarities and differences between the rheological response of bead-chain and spaghetti assemblies, we apply many cycles of oscillatory shear to reach the steady-state stress response. Next, we plot the torque τ and the deflection angle ϕ in one shear cycle in the form of parametric Lissajous-Bowditch curves, similar to the stress vs strain curves commonly used in the literature [63] (As the calculation of stress and

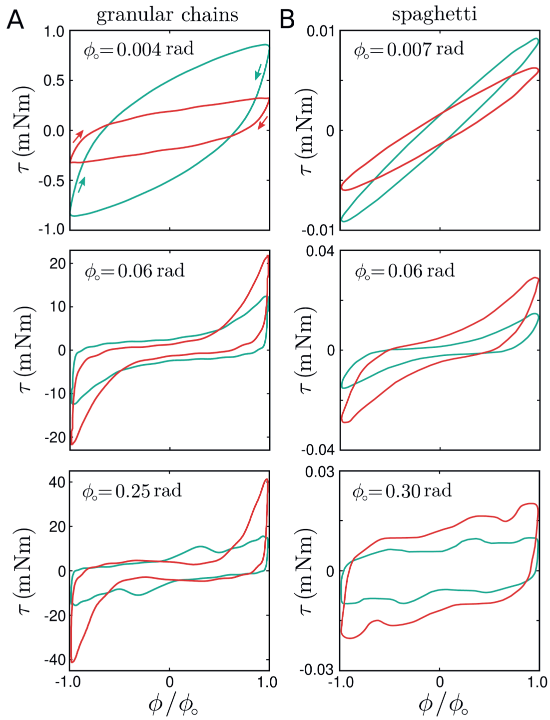

Figure 4.5: Elastic Lissajous curves of sheared bead chains and spaghetti. (A) Lissajous plots of torque vs deflection angle ϕ (scaled by $\phi_\circ$) for bead chains of length N=1 (green) and N=45 (red). (B) Similar plots for assemblies of spaghetti with length L=13 mm (green) and L=196 mm (red).

strain in our inhomogeneously sheared system involves approximations, here we use raw τ-ϕ data to avoid approximation errors). In the SAOS regime (Fig. 4.5, top row), we observe that the spaghetti data display an ellipsoidal shape, characteristic of a linear viscoelastic response. The response of granular chains displays a rhomboidal shape. The nonlinear behavior indicates that higher harmonics are present in the signal. The degree of stiffening is larger for shorter constituent elements (being bead chains or spaghetti strands) in agreement with Fig. 4.3A. Around the transition amplitude ϕ_c (middle row), a highly nonlinear torque re-

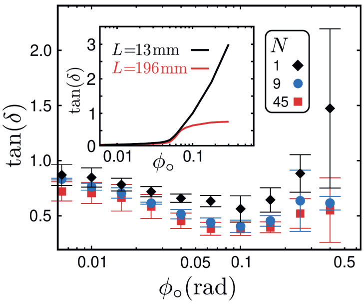

Figure 4.6: Chain-length dependence of the loss tangent. The main panel represents the loss tangent $\tan(\delta)$ versus rotation amplitude $\phi_\circ$ for different bead chain lengths. The inset represents a similar comparison between assemblies of spaghetti with different lengths.

sponse develops in both systems, evidencing the emergence of intracycle stiffening. Here, the curves develop a larger degree of stiffening for assemblies of longer constituent elements. We also note that the stiffening in bead-chain Lissajous curves is more pronounced due to the simultaneous formation of loops and activation of interlocking; the latter is absent in spaghetti assemblies. The main difference between the rheological response of bead-chain and spaghetti assemblies arises in the LAOS regime (bottom row): In bead chains, while packings of individual beads (N=1) yield, assemblies of longer chains exhibit an even stronger response. In contrast, spaghetti assemblies are unable to develop higher stress and yield at all strand lengths; still, the response remains steeper for longer spaghetti strands.

Finally, we clarify how viscous stresses develop with increasing the rotation amplitude $\phi_\circ$ in macroscale chain assemblies. This can be achieved, e.g., by analyzing viscous Lissajous curves of τ vs $\dot{\phi}$. Here, we alternatively consider the loss tangent, $\tan(\delta)$, which is a dimensionless parameter that measures the ratio of dissipated to stored energy in one cycle of oscillation. The results shown in Fig. 4.6 reveal that packings of individual beads dissipate a larger fraction of energy compared to chain assemblies, even in SAOS. The difference becomes more pronounced in

LAOS due to the frictional flow of the yielded assemblies of individual beads as well as the increased contribution of the stored elastic energy in chain packings upon strengthening the entanglements. A similar trend is observed in shearing of spaghetti, i.e., longer strands dissipate less energy. Here, the role of the stored elastic energy is less important since longer strands fail to develop entanglements at large shear strains. Instead, the frictional flow of shorter strands is more dissipative.

4.4 Conclusions

In conclusion, we have studied the nonlinear rheology of entangled assemblies of long semiflexible objects. Unveiling the rheological response of externally-driven interacting particle assemblies— particularly quasi-1D materials such as (bio)polymers and granular chains— is currently a great challenge for statistical physics. Our results demonstrate a universal transition from narrow shear zones at low amplitudes of oscillatory shear to broad ones at large amplitudes with a width that scales with the chain length. We have linked this intriguing rheological response to the development of topological and geometrical constraints: The system undergoes a sharp crossover from lacking entanglements to a highly entangled environment. Nevertheless, entanglements are not the only influential factor in determining the mechanical response and yielding of macroscale chain assemblies. Friction is known to play a crucial role in packings of individual beads and networks of fibres [340–342]. Understanding how the interplay of friction and entanglements governs the rheological response of chain assemblies is a future challenge toward answering the question of how assemblies of long flexible objects flow. The insight from the present study can also help for better understanding the compaction and packaging of quasi-1D semiflexible objects [171, 343, 344] and can be used as a guide to design the micro/nano-structure of new materials.

4.5 Supplementary Material

Video 1. Examples of oscillatory shear experiments with chain length N=1 or 9 and rotation amplitude ϕ=0.063 or 0.632 rad. Link to video.

4

Chapter 5

Effect of fiber orientation on the shear rheology and Poynting effect in meat and meat analogues

This chapter has been submitted as:
Giménez-Ribes, G., Oostendorp, M., van der Goot, A. J., van der Linden, E., & Habibi, M. Effect of fiber orientation on the shear rheology and Poynting effect in meat and meat analogues.

Abstract

The development of plant-based meat analogues is an important aspect of the transition towards using more plant based proteins. Production of such structures with texture, rheology, and sensory properties adequate for consumer acceptance similar to meats is a great challenge. An important step is to quantify the similarities and differences of plant-based meat analogues and whole cut meats. However, there is a current lack in quantitative methods that compare whole cut meats and plant-based analogues taking into consideration the effect of fiber orientation. We tackled this problem by combining the non-linear shear rheology and shear-induced normal stress measurements on whole cut meats (beef and chicken) and plant-based fibrous model systems for meat analogues made with soy or pea protein isolates combined with wheat gluten (SPI-WG and PPI-WG, respectively) via shear cell technology. We found differences in G' and G'' between different fiber orientations for beef, chicken and SPI-WG. Meat samples showed rearrangements at small strains, whereas at large strains exhibited a lower energy dissipation and higher intracycle strain stiffening than plant-based fibrous systems, likely due to more elastic fibers. The plant-based fibrous products behave more solid-like until a larger strain, but the fibrous structures break down at large deformations resulting in higher energy dissipation than meat. The more elastic fibers in meat samples also exhibited a larger normal stress response (larger Poynting modulus) and showed large differences in magnitude between different fiber orientations. We therefore explore the importance of fiber orientation on the nonlinear rheology of fibrous model systems for meat analogues which has been largely ignored previously. We also provide a robust methodology combining nonlinear shear rheology with the measurement of shear-induced normal stress to quantitatively compare different mechanical responses of meat and fibrous plant-based meat analogues (that contribute to sensory perception), thereby allowing to compare and possibly tune the mechanical responses of plant-based meat analogue products towards real meat.

5.1 Introduction

Research on plant-based meat analogues has increased tremendously in recent years. The main reasons prompting a transition from meat products to plant-based analogues are from environmental and sustainability [345], ethical [346], and health [347, 348] concerns. However, one of the ongoing problems in producing meat analogues that consumers like, is achieving a texture which resembles that of real meat. This can be seen by the number of methods developed for mimicking meat texture including shear cell technology and high-moisture extrusion [349, 350]. Current meat analogues can be roughly classified into two different types: 1) those that mimic processed meats, such as sausages, hamburgers, or meatballs, and 2) those that mimic the whole cut meats, such as chicken, beef, or pork skeletal muscle cuts. In the case of "processed" meat analogues, acceptability is already high [351], since the structures in the original meat-based products are to a large extent broken down, which facilitates replicating the resulting texture. However, in the case of "whole cut" analogues, a similar experience to their counterparts meat whole cuts remains a great challenge [351], especially concerning the fibrous texture and juiciness.

Meat, or skeletal muscle tissue, has a complex hierarchical structure composed of fibers. Roughly, the fibers are formed by bundled fibrillar structures, myofibrils, which are in the μm range in diameter. The myofibrils are in turn composed of myofilaments, repeating units of sarcomers. If one zooms into the sarcomers, then one would find myosin and actin macromolecues as building blocks [41], which are responsible for the muscle contraction and relaxation. However, the individual muscle fibers (bundled fibrillar structures), are surrounded by endomysium, and in turn several fibers are bundled together by perimysium [42]. Both endomysium and perimysium are not fibers themselves, but connective tissue that allows for the adequate fiber movement upon muscle contraction [42]. While this description is just a generalization of the main muscle structure, and structural differences will always exist between different muscles and species of animals [43], it shows the complex hierarchical structures which composes the whole cut meats. This unique fibrous structure, which is not found naturally in any plant products, significantly determines the sensory perception of meat. Meat consumers often find the presence of fibrous texture very important [352]. Therefore, to mimic real meat such structures should be created by processing plant-based ingredients into fibrous products.

Although the structural characteristics of meat and tissues have been widely studied, comprehensive scientific methodologies that quantitatively compare meat analogues with real meat are still scarce, as pointed out in the review by [44]. In the case of shear deformations of meat samples the Warner-Bratzler test is widely used. This method consists of a V-shaped blade that applies a cutting deformation to a meat product. However, the Warner-Bratzler method applies a combination of shearing, tensile stress and compression, which makes it more a measure for quality attributes than a method to precisely quantify physical attributes [45]. A similar issue is present also with the Kramer Shear Cell, which mimics a bite into a food piece using multiple parallel blunt blades, and therefore results also in a combination of mechanical deformations [44].

Despite the advances in the production of plant-based meat analogues, achieving a texture that mimics that of whole cut meat samples is still an ongoing quest. While the aforementioned methods to assess meat texture have an important body of research available, studies applying purely shearing deformations on meat or meat analogues using a shear rheometer are still scarce. The use of shear rheometers to study several food products from very different natures is widespread, with examples such as cheese [353], plant-based cheese analogues [354, 355], ice-cream [356], or protein oleogels [357]. Even mozzarella cheese, which also has a fibrous structure due to being a pulled-curd type of cheese, was compared with other cheeses using non-linear shear rheology, although the effect of the filaments orientation was not considered [48]. Therefore, shear rheometers can be used to quantitatively measure meat samples, thus allowing direct comparison with meat analogues.

Most of the shear rheology research on soft tissues focuses on organ tissue for medical purposes, such as liver [358–362] or brain tissues [363–

365]. But only a few address the skeletal muscle, which is the vast majority of meats we consume. Furthermore, most of these shear rheological studies, focus on measuring the dynamic moduli in the linear viscoelastic (LVE) region, whereas mastication and many food production processes occur well beyond the LVE regime [46, 47], and thus small deformation rheology does not provide a good approximation to the oral processing [49]. In a study by Melito *et al.* [366], the authors found correlations between the non-LVE regime and certain textural properties perceived in sensory tests, indicating that non-linear rheology is a better fingerprint of food texture than small amplitude rheology. A recent study by Schreuders *et al.* [367], studied the non-linear shear rheology of meat and meat analogue samples using a closed cavity rheometer at 4.5 bar, proving it to be a valuable method for quantitatively comparing the meat cuts and meat analogues. However, in that study the orientation of meat and meat analogue fibers was not taken into consideration. In the study by Tan *et al.* [368], the effect of post-mortem time and fiber orientation in raw bovine skeletal muscle was studied using large amplitude eccentric and Fourier Transform-rheology. The authors found the storage modulus, G', for perpendicular alignments to be higher than for parallel alignments. Therefore, studies on the non-linear shear rheology of cooked meat that compare the results to meat analogue samples considering the effect of fiber orientation are still lacking. Furthermore, the texture of cultured meats was recently measured via shear rheology, albeit focusing only in the small shear amplitude parameters G' and G'' [369], and would benefit from applying non-linear rheology for a deeper understanding of the mechanical properties as well.

For most materials, shearing induces a dilation, which translates as a normal stress response when the sample is sandwiched between parallel plate or cone-plate geometries (and the gap is kept constant). Interestingly, we could not find any literature that studied the shear-induced normal stress response in combination to the shear stress for any food products. Previous literature has highlighted the significance of non-linear shear rheology in improving the correlation between instrumental measurement and sensory properties [46–49, 366]. Therefore, in scenarios involving complex deformations such as chewing the shear-induced normal force would also be expected to play a role in sensory perception. This shear-induced normal stress response is also known in literature as Poynting effect, and has been known for isotropic materials for over a century [69]. When a material is sheared, or a torsional deformation is applied in between parallel plates, it leads to expansion in the normal direction, with the normal stress difference, $N_D = G_N\gamma^2$, thus following a quadratic relation with the shear strain [69, 70]. The coefficient for such quadratic relation, G_N, is known in literature as the Poynting modulus [72], and for most materials it has a positive sign, known as positive Poynting modulus. Only in recent years a negative Poynting modulus, i.e. contraction of the sample, has been observed also for specific biopolymer gel systems, such as fibrin protein gels [73]. Later, this negative Poynting effect was attributed to biopolymer gels, with relatively large pore sizes in the μm range, that are able to expel fluid to relax the pressure gradients [370, 371]. For meat and meat analogues we expect a positive Poynting modulus, since those products do not possess those large pores through which water can freely flow. The question, however, remains on whether the measurement of the Poynting modulus magnitude allows for quantitative comparison of meat and meat analogues samples, including the effect of fiber orientation in the samples.

It is therefore the aim of this study to compare the non-linear shear and shear-induced normal force response of whole meat cuts and meat analogues that contain anisotropic structures trying to mimic the meat fibrous properties. We do so by measuring the shear response both in small amplitude oscillatory shear (SAOS) and large amplitude oscillatory shear (LAOS), as well as the normal stress difference measured by the rheometer during oscillatory measurements. We believe this is relevant for a deeper understanding of meat texture under deformations, and the formulation of meat analogues trying to mimic meat texture. Our results therefore provide a detailed quantitative method to measure plant-based analogues and compare them to meat samples using a shear rheometer.

5.2 Materials and methods

5.2.1 Materials

Beef (Iers rundvlees: Biefstuk) and chicken meat (Scharrelkip: Kipfilet) were purchased from a local supermarket (Jumbo, Wageningen, The Netherlands). For the meat analogues, two types of couette cell shear-structured plant protein blends were used. Soy protein isolate (SPI) SUPRO 500E A (94% DM with 90% protein in dry base) was obtained from WLT distributors inc. (Winnipeg, Manitoba, Canada). Pea protein isolate (PPI) Pisane M9 (96% DM with 85.2% protein in dry base) was purchased from Cosucra (Warcoing, Belgium). Wheat gluten (WG) VITEN Vital (92% DM with 83% protein in dry base) was acquired from Roquette Belgium (Brussels, Belgium). SPI-WG and PPI-WG blends were prepared according to protocols from Schreuders *et al.* [372], with the final composition in the samples as shown in Table 5.1. Briefly, SPI or PPI powder was dispersed in a sodium chloride solution and hydrated for 30 min stirring. Then, WG was mixed into the protein dispersion. To obtain the oriented structures, mimicking meat fibers, the mixtures were added to a high-temperature up-scaled Couette Cell (explained in detail in [373])) based on the concentric cylinder rheology geometry. The protein mixtures were then processed at 120^{o}C for 30 min, at a shear rate of 30 rpm.

Table 5.1: Composition of the samples at the end of processing steps, in %.

Sample	PPI/SPI	Water	Salt	WG
SPI-WG	15	69.5	0.5	15
PPI-WG	17.5	64.5	0.5	17.5

For the meat samples, raw and heat treated samples were studied to mimic the state of the fiber structures upon consumption. The heat treatment was performed by placing the samples in plastic bags, removing as much air as possible by submerging it in water, after which the product was placed in a water bath for 60 min at the chosen temperature. Cooking temperatures for the meat were chosen based on literature at

70^{o}C for beef [374] and 66^{o}C for chicken [375]. For comparison, SPI-WG samples were also given heat treatment at 66^{o}C.

Samples were cut into the right size for rheology tests by first slicing 3 mm thick slices with a meat slicer (Solida 4, Ritter, Germany), cutting either parallel to the fiber orientation or perpendicular to the fibers. Then, disk-shaped slices were cut with a cylindrical cheese slicer of 25 mm internal diameter. A schematic representation of how the samples were position under the rheometer geometry, as well as the coordinates used for the rheological study are shown in Figure 5.1.

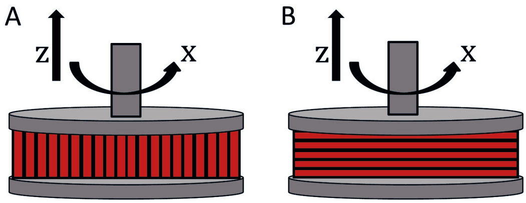

Figure 5.1: Schematical representation of the fiber orientations studied in the plate-plate geometry, with fibers perpendicular (A) or parallel (B) to the shear direction. The coordinates considered in the geometry are also indicated, with x being the azimuthal (shear) direction, and z being the shear gradient direction.

5.2.2 Shear rheological experiments

A standard Anton Paar MCR rheometer (Anton Paar MCR 301, Graz, Austria) was used together with a 25mm diameter plate-plate geometry. To avoid wall slip, grooved plate geometries were used in combination with a 10% preload. This was done by lowering the plate until a 0.1 N was reached, to ensure homogeneous contact with the sample, then the upper plate was lowered until achieving the 10% compressive strain [368].

We employed two different oscillatory protocols on the samples. First, a standard amplitude sweep, performed at constant frequency of 0.1 Hz with increasing strains from 0.01 % to 100 %. During the amplitude sweeps, the oscillatory signal of the shear stress σ_s was defined as

$$\sigma_s\ (t) = \sigma_{xz}\ (t) = \sum_{n=1,\ odd} \sigma_n \sin(n\omega t + \delta_n), \tag{5.1}$$

where σ_n represents the shear stress amplitude of the n harmonic, and δ_n the phase shift of the n harmonic. For each strain amplitude point, the oscillatory stress and strain data were used for plotting Lissajous curves and calculate the LAOS parameters strain stiffening ratio, $S-ratio$, and dissipation ratio, Φ. Both of these parameters are defined, respectively, as [63]

$$S = \frac{G'_L - G'_M}{G'_L}, \tag{5.2}$$

and [67]

$$\Phi = \frac{E_d}{(E_d)_{pp}} = \frac{\pi\gamma_0 G''_1}{4\sigma_{s,max}}, \tag{5.3}$$

where $G'_L = \frac{\sigma_s}{\gamma}|_{\gamma=\gamma_0}$ is the large-strain modulus at γ_0 and $G'_M = \frac{d\sigma_s}{d\gamma}|_{\gamma=0}$ the shear elastic minimum-strain modulus, and $E_d = \oint \sigma_s d\gamma = \pi\gamma_0^2 G''_1$ being the energy dissipated per unit volume within a LAOS oscillation cycle, and $(E_d)_{pp} = (2\gamma_0)(2\sigma_{s,max})$ the possible maximum energy dissipated by a perfect plastic material in an oscillation cycle.

To obtain also the oscillatory normal stress difference N_D during the strain oscillations we performed a second protocol with a built-in project for sine-wave generator from the RheoCompass software (Anton Paar GmbH, Graz, Austria), as done by Martikainen *et al.* [376]. This allowed us to perform oscillations and record all the parameters in real time during 10 cycles of oscillation, at 5 different strain points (0.05%, 0.1%, 0.5%, 1%, and 5%), which were selected from the amplitude sweep curves. The N_D, is then [377]

$$N_D = N_1 - N_2 \approx G_N \gamma^2. \tag{5.4}$$

It is important to note that for plate-plate geometries, deformation across the sample is not uniform, and thus the first normal stress difference (N_1) is not explicitly given by the measured normal force divided by the area of the sample. Therefore, we use a normal stress difference, given by $N_1 - N_2$ in parallel plate geometry, as reported from the rheometer and as used before in literature [378]. Previous literature has also mentioned that the normal stress difference as determined from parallel plate geometry is a good approximation of N_1 [46].

5.3 Results and discussion

5.3.1 Shear stress response: SAOS and LAOS

The amplitude sweeps for the four raw samples, *i.e.*, beef, chicken, SPI-WG, and PPI-WG are shown in Figure 5.2. The values of storage modulus G' for all the samples are similar, with values around 10-20 kPa, and larger than the loss modulus G'' indicating the solid-like behavior. Furthermore, for all samples the moduli are larger for perpendicular fiber orientations (with respect to the shear direction), indicating a stiffer response. Only in the case of PPI-WG, for both orientations the moduli are comparable with overlapping of the experimental errors. In the case of raw chicken samples, the orientation parallel to shear have the lower moduli, which indicates more mobility of the structural components in the direction of the shear. While the amplitude sweeps were performed up to γ =100%, we observed wall slip at $\gamma >$ 20%, and thus used that cut-off value for our interpretations. Therefore, besides the case of chicken with parallel orientations, all samples behave similarly when comparing the G' and G'' in the LVE regime when the meat samples are not cooked.

Differences became apparent between the meat and plant-based fibrous samples in the extent of the LVE regime. For the meat samples both G' and G'' start decreasing at lower strains, indicating a softening of the sample. On the contrary for the plant-based samples G'' remains constant until a larger strain, indicating a decrease of elasticity, and a more dissipative behavior than meat samples.

Since in most cases meat samples are not consumed raw, we studied the effect of heating to temperatures commonly used for cooking the

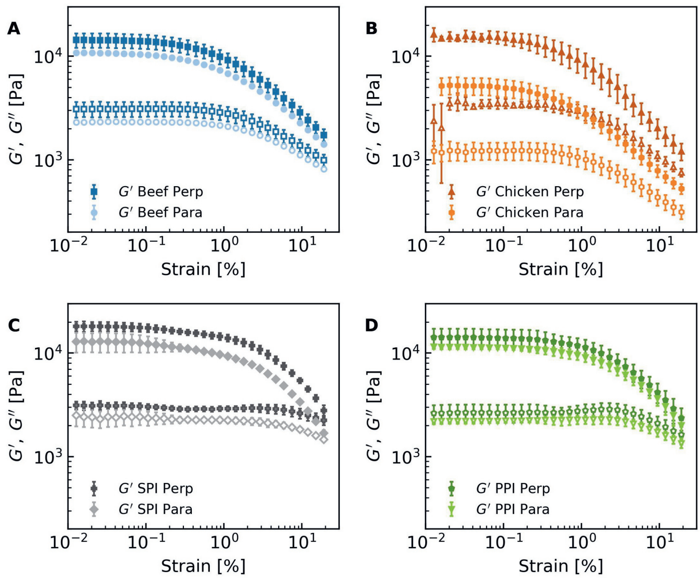

Figure 5.2: Amplitude sweeps curves for raw beef (A), raw chicken (B), raw SPI-WG (indicated as SPI, C), and raw PPI-WG (indicated as PPI, D). Closed symbols indicate the storage modulus G', and open symbols the loss modulus G''. Darker colors used for the samples oriented perpendicular to shear direction, and lighter color for the samples orientated parallel to shear direction.

meat. The results for cooked beef, chicken and SPI-WG are shown in Figure 5.3. In the case of meat it is well known that cooking affects its structure [379], as we see also in our results where the G' increases $\approx$ 5-fold for beef and $\approx$ 2-fold for chicken. Meat is very sensitive to temperature, due to different chemical reactions occurring upon heating such as hydrolytic degradation or protein denaturation [379] which significantly changes its mechanical properties. On the other hand the mechanical properties of our meat analogue samples do not change significantly after heating process and remain almost the same within the experimental errors. This is in accordance with previous studies comparing meat and meat analogues [367], and is not unexpected considering that these plant-based samples have been processed at 120^o C, and their proteins have already been denatured. Therefore, one could consider these plant-based fibrous systems to be already cooked during the fabrication step. For this reason, in the remaining of the paper we compare mostly the overall rheological behavior of cooked meat and "uncooked" plant-based fibrous model systems.

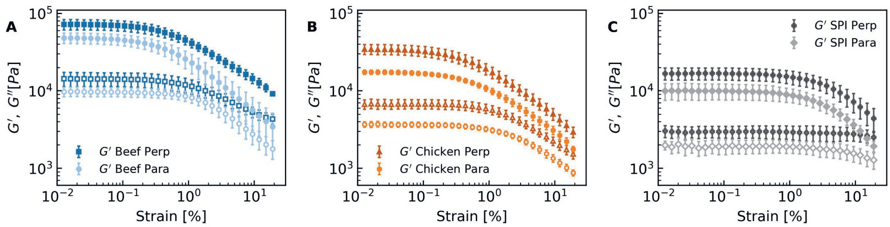

Figure 5.3: Amplitude sweeps curves for cooked (heat treated) beef (A), cooked chicken (B), and cooked SPI-WG (indicated as SPI, C). Closed symbols indicate the storage modulus G', and open symbols the loss modulus G''. Darker colors used for the samples oriented perpendicular to shear direction, and lighter color for the samples orientated parallel to shear direction.

From Figs. 5.2 and 5.3 we clearly observe differences in the mechanical responses for different orientation of the fibrous structures. The orientations perpendicular to shear exhibit a stiffer response compared to the parallel ones. However the information provided in the LVE regime is always limited. The NLVE regime provides crucial information for studying the mechanical responses of food products under large deformations such as mastication or processing [47, 366]. Plotting the intracycle stress oscillations as a function of the strain in the form of Lissajous plots is one way to study the nonlinear properties. In Figure 5.4 we show the Lissajous plots at selected strains.

Lissajous curves provide a clearer indication of why the storage modulus is larger for the fiber orientations perpendicular to the shear direction. The samples with perpendicular orientations, in orange in Fig. 5.4, give a higher maximum shear stress response than parallel for all samples except PPI-WG. This is an indication of the strong anisotropy in these samples, as deformation in different directions result in different mechanical responses. Furthermore, the Lissajous curves for meat samples are much thinner than those of SPI-WG and PPI-WG, indicating less relative energy dissipation and a more elastic response. This is quantified by the dissipation ratio Φ in Figure 5.5.

For the meat samples at about 1% strain the Lissajous curves start showing a slight pointing shape at the extremes. This becomes more pronounced when looking at 5% and 15% strains, resulting in an inverted sigmoidal shape. This is an indication of intracycle strain stiffening, and is quantified in the strain stiffening ratio, $S - Factor$, below in Figure 5.5. In contrast, for the plant-based analogues at low strains they still have more ellipsoidal shape with respect to beef and chicken. This again indicates that the nonlinear regime starts at larger strains for the plant-based analogues, as was observed from the amplitude sweeps as well. Interestingly, we observed superimposed oscillations in the Lissajous for SPI-WG and PPI-WG at the strain of 0.5% and 1% (Fig. 5.4). Often superimposed oscillations are considered as unwanted inertial effects [380]. However, in this case, considering the low strain amplitude at which we observe the superimposed oscillations, low frequency, and relatively high G' (in the range of 10 kPa) of the samples, the inertial effects are negligible. We therefore expect that the superimposed oscillations in the Lissajous curves are due to the presence of relatively large voids in the samples. The size of the voids are comparable to the deflection angle exerted by the rheometer at low amplitudes, and at large deformations their effect become less pronounced in the Lissajous curves. The presence of voids in this type of SPI-WG and PPI-WG samples has been mentioned before in the literature, and is considered to be an essential structural component contributing to the anisotropy of these samples [372]. For example in Figure 4 of ref. Schreuders *et al.* [372] the X-ray microtomography of such samples was shown, where the voids are clearly visible.

In Figure 5.5A and C, the Φ is shown for the meat samples and plant-based analogues, respectively. In the case of beef and chicken, Φ starts increasing at smaller strains, in line with the smaller range of LVE for this

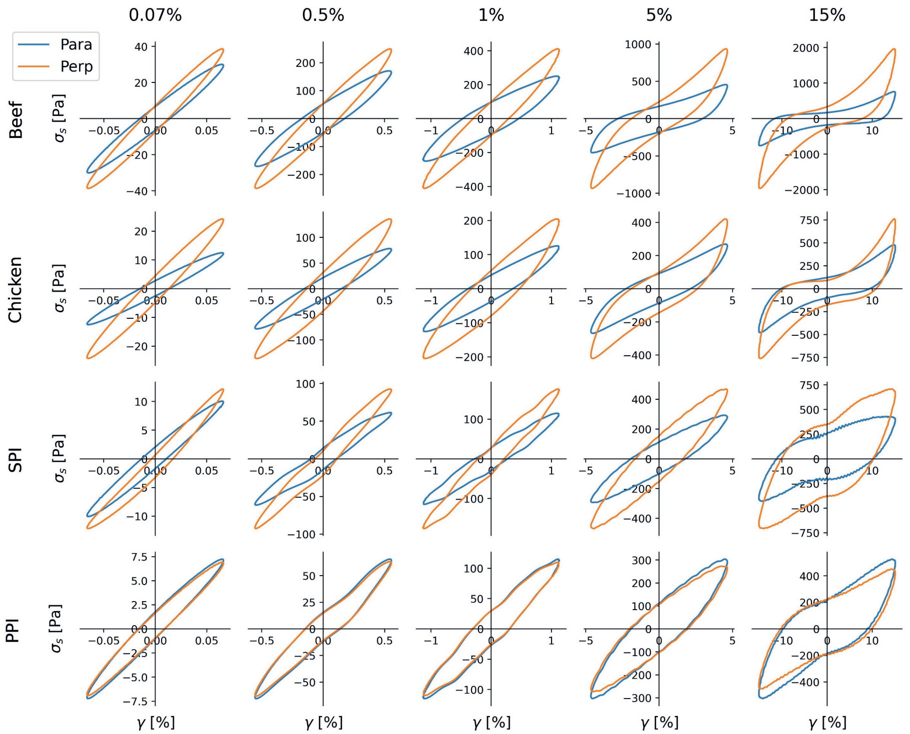

Figure 5.4: Elastic lissajous curves of shear stress, σ_s, versus shear strain for cooked beef, cooked chicken, SPI-WG (indicated as SPI), and PPI-WG (indicated as PPI), at 5 different strain points.

samples. While for chicken the fiber orientation does have a considerable effect to cause differences in Φ values, in the case of beef the perpendicular fiber orientation shows lower energy dissipation than the parallel one. At the same time, the perpendicular beef fiber orientation exhibited a larger G'. These effects were observed before for sheared crumpled materials with orientations perpendicular or parallel to the shear direction [173], and were attributed to sliding of stacked layers over each other, parallel to the shear direction. The sliding movement of fibers will result in a higher Φ than perpendicular ones.

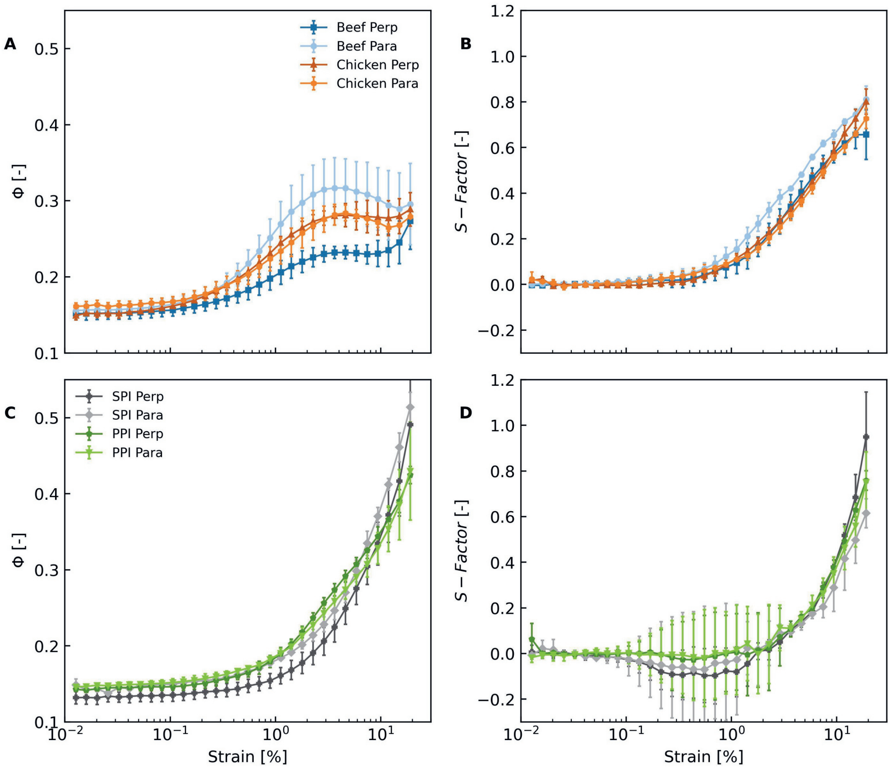

Figure 5.5: Dissipation ratio (A) and strain stiffening ratio (B) for cooked meats, and dissipation ratio (C) and strain stiffening ratio (D) for meat analogues.

For the meat samples, Φ exhibits a plateau at ≈0.3 for strains > 2%, whereas for the plant-based analogues Φ starts increasing at larger strains, but then increases very steeply to values between 0.4-0.5. This results indicate that for the meat samples, some breakage of weaker fibers or connective tissue takes place at small strains, but at larger strains the stronger meat fibers withstand the deformations without increasing the relative dissipation. On the other hand, the plant-based analogues behave more elastically until larger strains, but once a critical strain is reached, the fibrous structures break down to a larger extent than meat fibers. Therefore, the structures in meat are stronger at large deformations, and behave more elastically than the plant-based analogues, as seen also in the Lissajous curves in Fig. 5.4. The large error bars ranging from around 0.1 to 3% in 5.5 D are attributed to voids being present in the meat analogue samples, as has been discussed earlier. This results in slight changes of the local slopes of the Lissajous at small deformations (See 5.4), and becomes less pronounced at larger deformations.

For the strain stiffening ratio (Fig. 5.5B and D), a similar situation to Φ occurs, with $S-factor$ increasing earlier for meat than meat analogues. However, at the maximum studied strains, the meat samples and plant-based analogues show a similar $S - Factor \approx 0.8$. These results are similar to those shown in [367] for meat, fish, and commercially available meat analogues. While at $\approx 20\%$ strain the $S - Factor \approx 0.8$ for both meats and plant-based analogues, the Lissajous curves for meat indicate a more pronounced stiffening. Therefore, the increase of the $S - Factor$ observed for the meat analogues comes from an artifact in the definition on the $S-Factor$, as discussed in the paper from Mermet-Guyennet *et al.* [381]. This is mainly due to considering the local moduli for calculating the $S-Factor$. Therefore, the combination of Φ and $S-Factor$, together with a critical evaluation of the Lissajous curves themselves is necessary, when interpreting the data. Considering only the $S-Factor$ could cause a misinterpretation of the results.

Overall, the LAOS results together indicate that the fibrous structures in meat show a more elastic behavior, with real intracycle strain stiffening. In the study of García-Segovia *et al.* [382], beef meat microstructure cooked at 70^oC was investigated, where shrinkage of meat fibers and the shortening and solubilization of connective tissue were observed, causing the creation of small voids in between the muscle fibers. Furthermore, for raw skeletal muscle under large shear deformations, Tan *et al.* [368] observed connective tissue damage above 10% strain, being explained by the authors at the onset of microstructure rearrangement. In their study, the authors found that for parallel orientations, the stress is localized in the extracellular matrix around the muscle fibers, resulting in a degradation of the endomyssium [368]. Therefore, together these results support our hypothesis that, at relatively small deformations $\gamma \approx 0.5\%$, meat samples have some rearrangement due to the strain localization in already damaged connective tissue, increasing the dissipation due to sliding of the fibers. Then, at larger strains exhibit a plateau due to stretching of fibers which had become stronger after shrinkage during cooking. We did not observe the plateau in the dissipation ratio for the raw meat samples (provided as Supplementary Materials), remarking the importance of having damaged connective tissue and fiber shrinkage for the plateau in Φ.

It is important to remark the differences between overall softening with increasing strain amplitudes (intercycle softening), as seen in the amplitude sweeps, from the local intracycle strain stiffening, observed in the Lissajous curves [381]. If the Lissajous curves were to be plot with the same Y axis limits, the overall softening would become more clear, at the expense of not showing clearly the Lissajous shapes. Therefore, the overall behavior of these samples is still strain softening.

5.3.2 Normal stress response

While measuring the non-linear shear rheology of meat samples is still scarcely found in literature, it is becoming more popular for other sorts of food products. Shear deformation can induce dilation or contraction perpendicular to the shear direction. This highly nonlinear response is known as Poynting effect. Dilation and contraction can represent themselves as normal force when the sample is sandwiched between two plates with a fixed gap. Interestingly, there is no study of the shear-induced normal stress response in any food products. However, since previous literature remarks the importance of non-linear shear rheology to better correlate instrumental measurements with sensory properties [46–49, 366], it is expected that the shear-induced normal force would also play a role in the sensory perception with complex deformations such as mastication.

The normal force response data can be already measured by most commercial rheometers, and allows to analyze the non linear response of the material. This normal response can unravel more information about the anisotropic structure of the samples such as meat and plant-based analogues with anisotropic fibrous structures. To record the normal force response of the sample under shear deformation in a cycle an oscilloscope can be used [371]. In our study we performed a built-in project template available in RheoCompass software consisting of a sine wave generator as done by Martikainen *et al.* [376], which allows to manually instruct the rheometer which strain amplitude, frequency, and number of cycles to perform. Using this approach, the normal force data (or stress) is collected in real time during the whole oscillatory test, thereby allowing for representation of the data also as Lissajous curves, in this case by plotting normal stress versus strain, as shown in Figure 5.6.

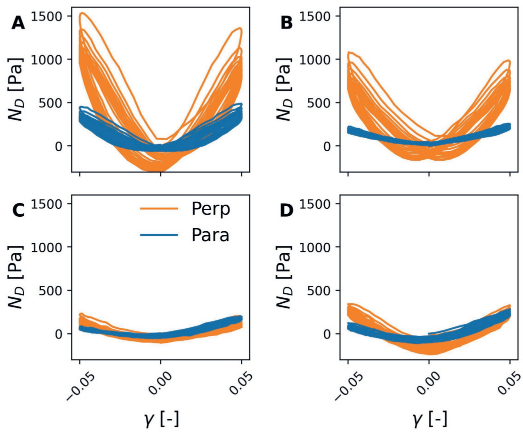

Figure 5.6: Lissajous curves of the normal stress difference, N_D, for the cooked beef (A), cooked chicken (B), SPI-WG (C), and PPI-WG (D) during the oscillatory shear strain deformations at 5% strain.

In Fig. 5.6, not only the differences between whole cut meats and plant-based analogues become clear, but also the fiber orientations for the meat cuts show differences. In the case of cooked beef and chicken, the parabola (quadratic response) is more pronounced for the orientations perpendicular to shear, represented in orange in Fig. 5.6AB. On the contrary, for the plant-based analogues the differences between orientations were much smaller. The differences between N_D in these Lissajous can also be quantified by fitting the quadratic equation 5.4 to the parabola to obtain the Poynting modulus G_N. The resulting G_N are shown in Figure 5.7. In all our results we observed a positive Poynting modulus, as observed before for instance from brain soft tissue [383].

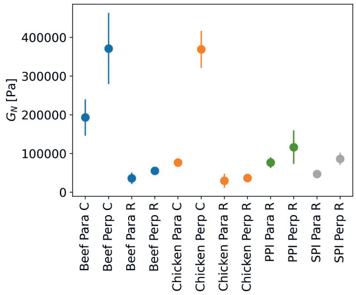

Figure 5.7: Poynting modulus, G_N, calculated from the oscillatory normal stress difference, N_D, using equation 5.4. C: Cooked, R: Raw

G_N shows clear differences between the fiber orientation for cooked meats, as already inferred from the Lissajous shapes. SPI-WG, also shows difference in G_N for the different orientations, which coincides with this sample also having more clearly defined fibrous structures and showing differences in G' and G'' for the two different orientations. In the case of PPI-WG, G_N also increases for the perpendicular orientations, the differences are small and within experimental error. In the study of Schreuders *et al.* [372] who studied the macro- and microstructure of these plant based analogues, it is observed that while both samples produced fibrous structures at 120^{o}C, the SPI-WG produced more fibrous materials. Furthermore, the authors found the SPI-WG sample to entrap more air and have more extensive deformation of the air bubbles than PPI-WG when sheared at 120^{o}C, which also contributes to the production of more clearly observed fibers [372]. Therefore, the presence of more fibrous structures for SPI-WG, together with the larger amount of deformed air bubbles, explains the more anisotropic structure that results in a different G_N for the different orientations. Further studies comparing the shear-induced normal force response to sensory tests is needed to shed more light on this relation.

As we already observed in the amplitude sweeps data, the different fiber orientations result in different mechanical responses for the whole meat cuts. These differences, which we observe also for the G_N, are a result of the complex hierarchical structure present in the whole meat cuts, which is not present in plant-based analogue samples. Furthermore, from the shear Lissajous at 5%, which are at the same shear strain as the N_D Lissajous in Fig. 5.6, we observed the meat samples to present more elastic behavior, with intracycle stiffening due to stiffer fibers of meat. Therefore, the larger G_N for the meat samples is also due to the stiffer fibers and the parabolic curve appears complementary to the intracycle strain stiffening. While we performed the sine-wave generator experiments also at smaller amplitudes of 0.05%, 0.1%, 0.5%, 1% strain, these samples did not show a quadratic response (Provided in Supplementary Material), and thus remarks the need of an intracycle strain stiffening behavior to clearly observe the quadratic response in N_D in our samples. The main rheological results obtained in our study are briefly summarized in Table 5.2

5.4 Conclusions

We quantitatively compared whole cut meat samples (beef and chicken) with couette cell shear-structured plant-based fibrous products, which are model systems for meat analogues made of soy protein isolate or pea protein isolate in combination with wheat gluten (SPI-WG and PPI-WG, respectively). To have a comprehensive analysis we developed a new rheological methodology and investigated the shear induced normal response and Poynting effect along with analyzing shear moduli and Lissajous curves. The storage, G', and loss, G'', moduli in the linear viscoelastic

	G', G'' (Orientations)	LVE Region	Φ	$S-Factor$	G_N
Cooked Beef	Different	Shorter	Increase early, plateau	Increase early, true stiffening	Large magnitude
Cooked Chicken	Different	Shorter	Increase early, plateau	Increase early, true stiffening	Large magnitude
SPI-WG	Different	Longer	Increase late, steeply	Increase later, artifact	Small magnitude
PPI-WG	Not Different	Longer	Increase late, steeply	Increase later, artifact	Small magnitude

Table 5.2: Summary of the results obtained for each rheological parameter from the different tests performed.

(LVE) regime allowed for studying the effect of orientation in the fibrous structures. The raw meat samples exhibited similar G' and G'' to the studied plant-based fibrous analogues, but differences became apparent after cooking. When the fibers were oriented perpendicular to the shear direction, G' and G'' were higher with respect to parallel orientations for beef, chicken and SPI-WG, whereas PPI-WG samples did not show significant differences beyond the experimental error. The use of large amplitude oscillatory shear (LAOS) allowed to further differentiate the role of structural components. The dissipation Φ and strain stiffening $S - Factor$ ratios showed the onset of non-linearity for meat samples at small strains due to rearrangements of fibers and breakage of weaker components such as connective tissues. At large strains the stiff elastic fibers resulted in lower dissipation and stronger intracycle stiffening than the plant-based analogue samples. On the contrary, the plant-based analogue samples showed a more solid-like structure at small strains than meat, but at larger strains the weaker fibrous structures broke down, increasing the energy dissipation.

The fiber orientation for the different samples resulted also in quantitative differences in their normal stress responses via studying the oscillatory normal stress difference N_D. Via fitting a quadratic relation to the N_D vs strain Lissajous curves, we obtained the Poynting modulus G_N, which showed differences for beef, chicken and SPI-WG for the two different orientations. As with G' and G'', the meat samples had a stronger G_N than those of plant-based analogue samples.

Besides the differences between whole meat cuts and plant-based analogues, the results also indicated differences between SPI-WG and PPI-WG. For SPI-WG, in all tests we found differences between the two different orientations, indicating that the anisotropy in SPI-WG is more predominant than in PPI-WG, and thus exhibits a behavior somewhat closer to meat samples, albeit at different magnitude. These differences were likely to be due to the stronger structures and the presence of more voids in the SPI-WG samples than in PPI-WG, as also mentioned in earlier studies. Therefore, not only the strength of fibrous structures, but also their orientation together with distribution of voids play roles in the nonlinear mechanical response due to structural anisotropy.

Based on our study we suggest that the efforts to mimic the whole cut meat structure should be directed to reinforce the strength of fibers, and anisotropic distribution of pores with specific size in the structure. Our novel rheological approach based on analyzing both shear and shear induced normal responses opens an avenue for comprehensive and quantitative comparison of mechanical responses of meat and plant-based counterparts. This approach facilitates future research into the effect of formulations and structuring processes to create new generations of plant-based meat analogues.

5.5 Supplementary Material

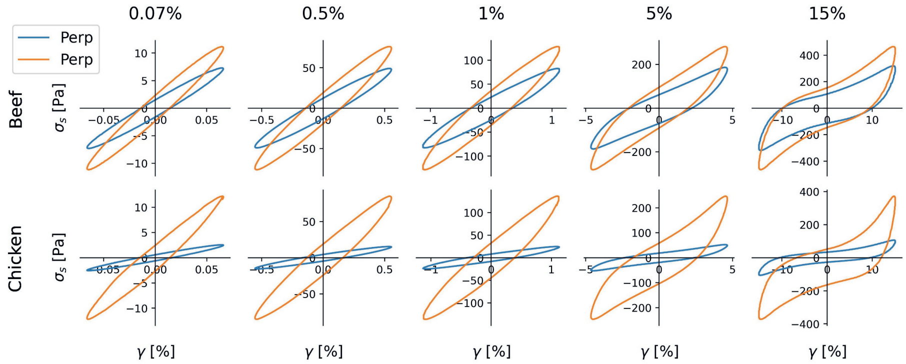

Figure 5.8: Elastic lissajous curves of shear stress, σ_s, versus shear strain for raw beef and raw chicken, at 5 different strain points.

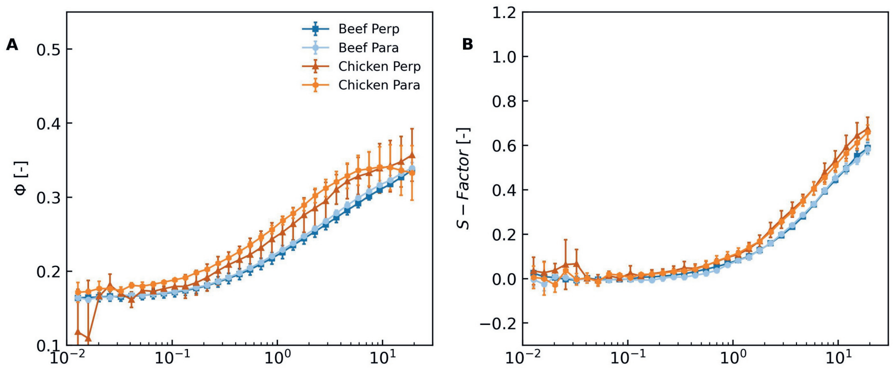

Figure 5.9: Dissipation ratio (A) and strain stiffening ratio (B) for raw meats.

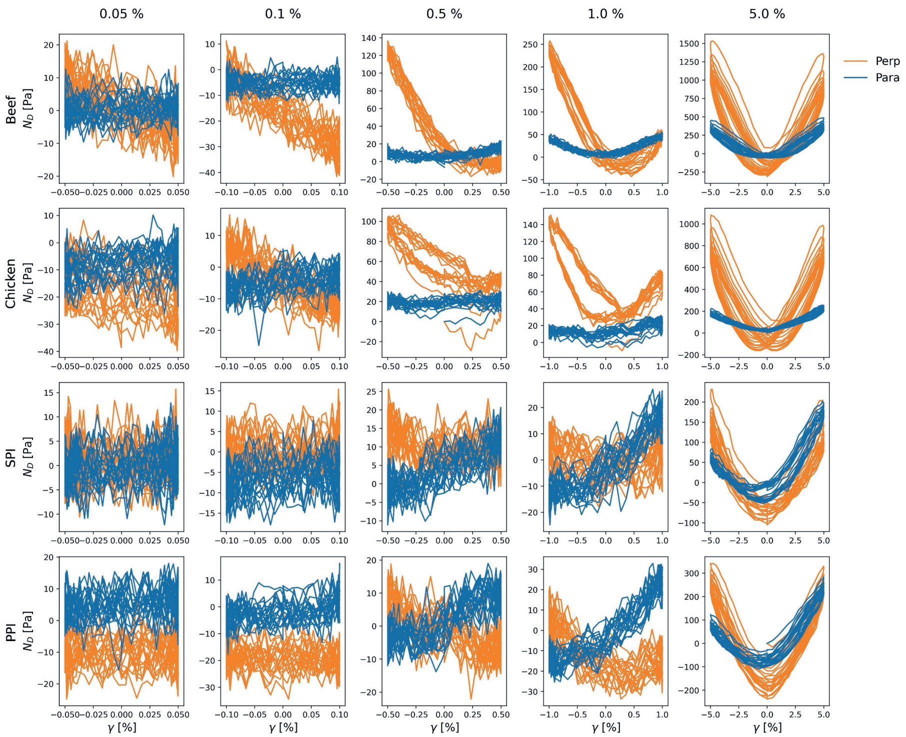

Figure 5.10: Lissajous curves of the normal stress difference, N_D, for the cooked beef (A), cooked chicken (B), SPI-WG (C), and PPI-WG (D) during the oscillatory shear strain deformations.

Chapter 6

Shear and shear-induced normal responses of origami cylinders

6

This chapter is to be submitted as:
Giménez-Ribes, G., Ghorbani, A., Teng, S. Y., van der Linden, E., & Habibi, M. Shear and shear-induced normal responses of origami cylinders: normal response reveals structural asymmetries.

Abstract

The interest in mechanical metamaterials such as origami structures with desired mechanical properties has increased in recent years. For example, origami bellows have been used for diverse applications and often studied under uni-axial deformation, however their mechanical response under shear, is poorly investigated. Specifically the shear-induced normal force response of such structures has received little attention. In this study, we investigated the shear and shear-induced normal response (Poynting effect) in structured thin cylindrical origami shells based on well-known Yoshimura and Kresling origami designs, experimentally and theoretically. Both designs present ordered structural arrangements, but with different symmetry with respect to the shear direction. In addition, we studied a third type of cylindrical shell made by crumpling a thin paper cylindrical shell under uni-axial compression, which presents semi-ordered patterns in the form of crumpled unit cells. The normal stress response of the Yoshimura design under shear was well fit with a quadratic relation, whereas the asymmetric Kresling cylinder showed a linear relation with a positive or negative normal force depending on the direction of shear. For the Crumpled cylinders the level of asymmetry in the semi-random folds pattern was quantified via an asymmetry index from the 2D Fast Fourier transform spectrum of the crease pattern images, which was well correlated to the asymmetry of the normal force response. We found that the shear-induced normal force in all structures is linked to the structural arrangement and asymmetry. In addition, we suggested opportunities of programming the Poynting response via origami design. Our findings provide a deeper understanding of the nonlinear mechanical response of origami bellows and the role of structural arrangements and (a)symmetry in their Poynting response. These findings provide opportunities for programming the shear and shear-induced normal responses of origami cylinders, and using crumpling as a design principle for fabricating meta structures. Potential applications of our findings range from soft robotics to sustainable design of packaging materials and medical devices.

6.1 Introduction

In recent years, research on mechanical metamaterials has gained increased popularity. This is mostly because these designed materials have exceptional mechanical properties and functionality that arise from their structure and conformation after processing rather than the composition of the material itself [3]. Origami structures are well-known examples of mechanical metamaterials. These days material engineers use the ancient Japanese art of paper folding to design structures with exceptional ability to absorb mechanical energy or adaptability to morph complex shapes and curvatures [384] and expressing a negative Poisson's ratio [385]. The properties of origami structures arise from their predefined periodic pattern of folds, on an initially flat surface with creating so-called unit cells [127].

Among origami structures, origami cylinders, also known as origami bellows, have found interesting applications in diverse fields of research. Examples include shock and energy absorption [50, 386], soft bistable electricity generator [51], self-deployable stent grafts for medical applications [52], origami swimming robots [387], dynamically dexterous robots [388], or even functional structures for cryogenic applications [389], just to name a few. Understanding the mechanical responses of such structures plays a crucial role in adapting them for a specific application. However, origami structures are mostly studied under uni-axial compression [50, 390] and hardly under torsion deformations. In all above examples, the origami bellows were investigated only under uni-axial compression or extension. Using such structures in real life applications means that torsional deformations coupled to uni-axial deformations would be unavoidable. This remarks the need to understand how origami bellows behave under shear deformations and how their unit cells contribute to their shear mechanical responses.

The most commonly used origami cylinder is designed based on the Yoshimura pattern [391]. This design consists of a diamond (rhomboid) pattern with mountain diagonal folds and horizontal valley folds, which interestingly often arises naturally upon compression of a thin confined cylindrical shell, given appropriate conditions of strain and compression rate [53] (Fig. 6.1). By tilting the Yoshimura patterns, a so-called Kresling pattern arises [54] (Fig. 6.1), with a diamond pattern similar to Yoshimura but with a certain angle of inclination. Both the Yoshimura and Kresling patterns therefore feature an identical structural order of folds, consisting of rhomboid unit cells, but present different symmetries in the shear direction: while Yoshimura is symmetric in both shear directions, the Kresling pattern is asymmetric. These properties make the Yoshimura and Kresling patterns ideal candidates for studying the effect of structural asymmetry with different structural orientations under torsional deformations.

Already in 1909 Poynting demonstrated that a steel piano wire under torsion exhibited a shear-induced positive normal force, leading to its elongation [69, 70]. This result translates in the material exhibiting positive normal stress when twisted, and is known as the Poynting effect. The positive normal stress follows a quadratic relation with a positive coefficient, which has recently been named in the literature the Poynting modulus [72]. This inherently nonlinear response of the normal stress upon shear therefore differs from the linear shear stress response commonly studied at small deformations. Such Poynting modulus has, to the best of our knowledge, never been studied before for origami designs of any nature. Origami bellows have the potential to also exhibit a Poynting modulus which can be programmed for sign and magnitude, but first the torsion-induced normal response of the origami and its unit cells require a deeper understanding. Taking inspiration in methodology from the study of Ghorbani *et al.*, [72], where the Poynting modulus was characterized for 3D printed cylindrical shells, we aim to study the Poynting moduli of Yoshimura and Kresling origami shells and compare them with their shear moduli. In this regard, combining the study of shear and shear-induced normal stresses offers a comprehensive approach to characterize the response of origami cylindrical structures under shear and at the same time shed light on the interplay between their structural asymmetries and mechanical responses.

Origami structures, like other highly ordered metastructures with well-defined unit cells, are sensitive to imperfections [128–130], and therefore are vulnerable to defects introduced under working conditions or manufacturing processes. Designing robust origami materials for real-life applications with a simple design principle is a goal for origami designer. Therefore, beside the two well-known origami cylinders, we introduce a third system which presents some level of inherent randomness: a crumpled cylinder. While a perfect Yoshimura pattern might be obtained under certain conditions as mentioned above, most often a crumpled pattern roughly resembling the Yoshimura arises for some materials such as paper. Similar phenomenon has been studied by Gottesman *et al.*, [56], when crushing paper conical shells. Therefore, via a uni-axial compression of cylinders, we can obtain a semi-ordered pattern (from now on referred as crumpled pattern) that resembles the Yoshimura design, but still contains a level of disorder in its structure via crumpled unit cells, as opposed to a perfectly designed Yoshimura bellow. To the best of our knowledge, no attempt has been made to study the mechanical response of such easy to manufacture structure with a semi-random pattern. This crumpled cylinder will therefore also be present some order (semi-order), as the Yoshimura and Kresling designs, but the asymmetry of the design is *a priori* unknown, due to the inherent level of randomness that arises when compressing a the initial cylindrical shell. We expect the mechanical response of the crumpled cylinder to depend to a large extent on this semi-random pattern of crumpled creases and vertices. For this reason, we combine the study of the mechanical response with an analysis of the crease pattern images, in an attempt to connect the morphology of patterns to its mechanical response.

Despite the interesting characteristics of these cylindrical structures made with different patterns, namely Yoshimura, Kresling, and crumpled cylinders, their non-linear response has so far been studied to a limited extent, and their shear-induced normal force response remains largely unexplored. In this research, our aim is therefore two-fold. First, to characterize the shear and shear-induced mechanical responses of ordered origami bellows in connection to structural ordering of folds and (a)symmetry, both experimentally and via modeling. Second, to investigate the shear and shear-induced response of crumpled bellows containing some level of disorder, and connect such response with the structural asymmetry present in the crease patterns measured via image analysis. All together, we perform a comprehensive study of how structural arrangements in cylindrical shells, both ordered and disordered, affect their shear and shear-induced normal responses. Our results provide new insights into the nonlinear mechanical response of origami bellows, as well as the role of structural asymmetry in the shear-induced normal force response. These results are relevant for diverse applications, ranging from soft robotic elements to sustainable packaging materials or medical origami devices.

6.2 Materials and Methods

For our experiments, paper sheets of A4 standard size (UPM, Lahti, Finland), density 80 g m^{-3}, and 0.1 mm thickness were used. The different designs were made so that they could be adjusted to the A4 paper sheets.

6.2.1 Cylinder structures

We made the samples by folding the paper into specific origami patterns (Yoshimura, Kresling), or by compressing a paper roll with a thickness of 3 layers inside a plexiglass cylinder (15 mm radius) using a texture analyzer TA.XT plus (Stable Micro System – SMS, Surrey, United Kingdom). The three different types of cylinders are shown in Figure 6.1. Both Yoshimura and Kresling cylinders were fixed via a small overlapping area glued together. The crumpled cylinder was made by rolling a paper to obtain three layers, and fixing the edges with a very thin cellophane tape. This was done to favor the formation of the pattern, as using a single layer of paper resulted in more random crumpling of the whole structure upon compression in the plexiglass cylinder. The cylinder was then compressed from an initial height of 70 mm to 10 mm at a slow compression of 0.5 mm s^{-1}. We performed pretests to compare the effect of gluing or fixing with thin cellophane tape the edges of the cylinders under compression and found no significant difference.

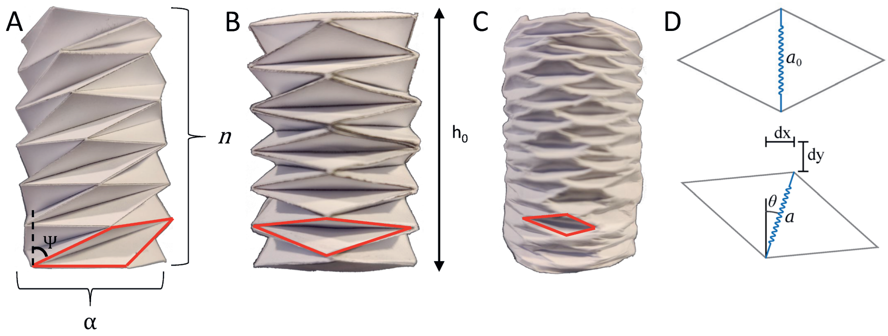

Figure 6.1: Example of the unit cells (red) accounted for the Kresling (A), Yoshimura (B), and Crumpled (C) cylinders. The parameters n and α represent the cells in the vertical, and horizontal directions, respectively. h_0 shows the height in the resting state. (D) Unit cells used for the numerical calculations, with the diagonal spring at initial length, a_0, and after shearing deformation, a.

6.2.2 Rheological experiments

All the measurements were performed using a standard Anton Paar MCR rheometer (Anton Paar MCR 302, Graz, Austria), with a 50 mm parallel plate geometry. Both plates were covered with double-sided tape to prevent any wall slip.

Shear deformation

The three types of cylinders were subjected to a small deflection angle, φ, of 30 or 100 $mrad$ in both clockwise and counterclockwise shear directions. For each sample and repetition, the zero compression strain, $\varepsilon_c = 0$, was defined as the gap where the compression force was 0 N. We performed the torsional deformations for all samples at $\varepsilon_c = 0$ and also at increasing ε_c for the Yoshimura and Kresling cylinders, whereas the crumpled cylinder exhibited a large effect of relaxations, as will be discussed below. To reduce any torsional stress build-up, the compression between gaps for Yoshimura and Kresling was performed at a low speed of 0.01 mm s^{-1} and the upper plate was let to rotate freely. Before starting to apply the shear deformations, all the samples were let to relax for 1 h. All measurements were performed at least in triplicate.

For each gap, the resulting Poynting modulus, G_N, was calculated as

$$F_N = G_N J \left(\frac{\varphi - \varphi_0}{h} \right)^2, \tag{6.1}$$

where F_N is the normal force, $J = (\pi/2)(R_{max}^4 - R_{min}^4)$ the second moment of area of the cylindrical shell, φ the deflection angle, φ_0 the deflection angle at the center of symmetry, and h the gap [72]. Due to the asymmetry in the Kresling cylinder, the normal force does not follow a parabola, and thus we used a linear approximation of eq. 6.1 via Taylor's expansion:

$$F_N \approx -\left(\frac{G_N J \varphi_0}{h^2} \right) \varphi, \tag{6.2}$$

where φ_0 was calculated as

$$\varphi_0 = \left(\frac{h_u}{\bar{R}} \right) \tan(\psi), \tag{6.3}$$

with h_u being the height of a unit cell, ψ the angle of a unit cell (shown in Fig. 6.1), and $\bar{R} = (R_{max} + R_{min})/2$ the average radius. Since ψ changes at each compression level, as shown in Figure 6.2, this was calculated as $\psi(\varepsilon) = \arccos[(1 - \varepsilon_c)\cos\psi_0]$, with $\psi_0 = 57^o$ being the angle without compression.

Besides the Poynting modulus, also the shear modulus, G_s, was calculated for each cylinder under different compression levels as [72]

$$F_S = \frac{\tau}{\bar{R}} = G_s J \left(\frac{\varphi}{\bar{R} h} \right). \tag{6.4}$$

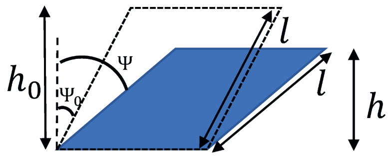

Figure 6.2: Kresling unit cell, with $\Psi_0 = 57^o$ and how it changes (Ψ) upon compression from h_0 to h coupled with torsion. The sides of the unit cell, l, remain constant during the compression.

6.2.3 Image analysis of angle orientation

We performed image analysis on the crumpled cylinder in order to obtain an estimation of the average angle of the diamond shape patterns after the sample is made under compression, as indicated in Section 6.2.1. After measuring the crumpled cylinders under shear deformation, it was cut in half and unfolded to take an image of the crease pattern. The image was analyzed with a method modified from [287], and as previously used also to quantify internal morphology in crumpled materials [173]. The image was first filtered to reduce noise using the *OpenCV.GaussianBlur* filter from the OpenCV library in Python [288]. Then the edges were detected with the *OpenCV.Laplacian* function, and a 2D Fast Fourier Transform was performed on the image using the function *numpy.fft.fft2* to obtain a matrix in the frequency domain (FFT power spectrum) [289]. By performing a summation in the azimuthal direction, we could draw FFT alignment plots where the peaks correspond to the dominating angles.

From the FFT alignment plots, we define an asymmetry index, I, as a percentage

$$I = \frac{A_2 - A_1}{A_1 + A_2}\,100, \tag{6.5}$$

where $A_1 = \int_{-90}^{0} I_{FFT}\,\mathrm{d}\theta$ corresponds to the integrated area from $\theta = -90^o$ to $\theta = 0^o$ of the FFT alignment plots, and $A_2 = \int_{0}^{90} I_{FFT}\,\mathrm{d}\theta$ to the integrated area from $\theta = 0^o$ to $\theta = 90^o$ of the FFT alignment plots.

Table 6.1: Dimensions of the designed cylinders and parameters used for the calculations.

Cylinder	R_{max} [mm]	R_{min} [mm]	n	α
Yoshimura	17.1	8.8	6	3
Kresling	20.15	11.75	6	6

Uniaxial compression

To calculate the spring constants of the unit cells for the designed cylinders, we performed uni-axial compression tests at a constant speed of 0.01 mm s^{-1}. Two different types of compression tests were performed: a rotation-free mode (Free), where the upper plate was let to rotate freely under compression, and a "clamped" compression (Fixed), where the upper plate was fixed. In both types, the normal force exerted during compression was measured, and in the "rotation-free" tests, also the deflection angle of the upper plate was measured. All measurements were performed in triplicate and averaged.

The compression strain was calculated as $\varepsilon_c = (h_0 - h)/h$, where h_0 is the height of the cylinder at $F_N = 0$, and h is the height during compression. The cross-sectional area of the cylinder was approximated as $A \approx \pi(R_{max}^2 - R_{min}^2)$, where R_{max} is the outer radius of the shell, and R_{min} is the inner radius. The compression stress was then calculated as $\sigma = F_N/A$. From the linear σ vs ε_c region before buckling of the cylinder under compression, we calculated an effective Young's modulus, Y_{eff}. The R_{max} and R_{min} for each cylinder are indicated in Table (6.1).

Since the compression is applied uniformly from the top layer of the cylindrical shell, each horizontal layer of cells remains horizontal. An effective spring constant for the whole cylinder is estimated by

$$K = \frac{Y_{eff} A}{h_0}. \tag{6.6}$$

Each layer n of the different cylinders consists of α unit cells, and thus the spring constant of each unit cell is calculated as

$$k = \frac{Kn}{\alpha} \tag{6.7}$$

.

The n and α parameters for each cylinder are indicated in Table (6.1).

6.2.4 Modeling of unit cells

Here we introduce a simple spring model to analytically study our origami systems. The Yoshimura unit cell consists of a rhombus-like design with relatively stiff edges that allow for bending at the nodes. We assume that the edges are infinitely stiff and that bending of the nodes is the only mode of deformation that this unit cell can acquire. As shown in Fig. 6.1D, such a unit cell effectively can be represented by a spring on one diagonal of the rhombus (here the vertical diagonal), where its spring coefficient depends on the bending stiffness of the nodes. In such a system, stretching/contraction and bending stiffness are two parameters that can contribute to the variation of the energy under deformation (Fig. 6.1). We assumed the spring is linear, and its strain (stretching/contraction) and bending coefficients are given by k and k_b, respectively. One can realize that the Kresling unit cell is the same as the Yoshimura unit cell but with a different angle, shown by θ_0. The energy of the system under deformation is given by $E = (1/2)ka_0e_i^2 + k_b(\theta - \theta_0)^2$, where a_0 is the initial length, e_i is the strain, and θ is the deflection of the unit cell. We obtained e_i and θ for different boundary conditions by minimizing the energy function.

The strain coefficient of the Yoshimura ($k = k_Y$ and $a_0 = a_{0Y}$) unit cell is obtained from its force-compression strain data based on the compression experiment under zero rotation (fixed), assuming that the bending of the unit cells is negligible. The strain coefficient of the Kresling unit cell (with $k = k_K$ and $a_0 = a_{0K}$) is obtained by re-scaling k_Y for the initial length of the Kresling unit cell, using $k_K = (a_{0K}/a_{0Y})k_Y$. The bending coefficients are set to reproduce the shear stiffness of the system under small torsional deformations.

6.3 Results and discussion

6.3.1 Shear experiments

We performed the characterization of the mechanical response of the different cylinders under shear, or torsional deformations. In addition to the shear response, we also investigated the normal force response arising from the shear deformation, as this is still scarcely studied in the literature for mechanical metamaterials such as origami cylinders. Examples of the shear-induced normal and shear force responses as a function of the deflection angle for the Yoshimura and Kresling cylinders at $\varepsilon_c = 0$ are presented in Fig. 6.3. The results obtained from modeling unit cells are included as an inset for each figure (the spring constant for the unit cells are included in Supplementary materials). The fit with black lines corresponds to eq. 6.2 (Fig. 6.3A), and eq 6.1 (Fig. 6.3B).

It is evident from Fig. 6.3 how measuring only the shear response from the rheometer measurement results in a loss of valuable information about the structures. While the torque as a function of deflection curves for both cylinders look similar, albeit reaching different magnitudes, their corresponding normal force responses are strikingly different. For the Yoshimura cylinder (Fig. 6.3B), which has a symmetric structure, the normal force response during the torsion experiments follows a parabola, characteristic of the Poynting effect. A concave-shaped parabola, i.e. the cylinder contracts under shear, indicates a negative Poynting modulus, while a convex-shaped parabola, i.e. expansion under shear, corresponds to a positive Poynting modulus. In our experiments, the Yoshimura cylinder measured at $\varepsilon_c = 0$ results in a positive Poynting response. The parabolic shape for the normal force response in the Yoshimura cylinder is due to the quadratic relation in eq. (6.1), where the turning point of the parabola is φ_0. The slight variations of φ_0, as well as the noise around the fit are assumed to be due to imperfections created during hand-folding and gluing the cylinders.

When the origami pattern exhibits asymmetry, as is the case for the Kresling cylinder (Fig. 6.3A), the normal force increases or decreases depending on the positive or negative deflection angle. Therefore, we ob-

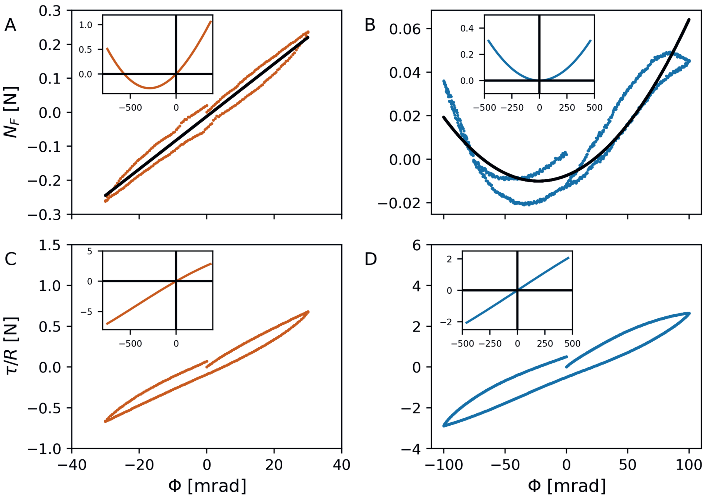

Figure 6.3: Upper row: example of shear-induced normal force responses for Kresling cylinder (A), and Yoshimura cylinder (B). Lower row: example of shear force responses under torsion for Kresling cylinder (C), and Yoshimura cylinder (D). Each shear force showed in the bottom row corresponds to the respective measurement of normal force in the upper row. Insets shows the numerical results of our model.

served a quasi-linear response, with the small deviations from a straight line being due to relaxation of the paper material. Since the Kresling cylinder has an asymmetric pattern, similar to the Yoshimura pattern, but with a certain degree of inclination, the φ_0 is not close to 0. Therefore, we used Taylor's expansion of eq. (6.1), resulting in eq. (6.2), to fit the linear relation of normal force as a function of deflection angle. This can be clearly seen with the inset in Fig. 6.3A, where the φ_0 is shifted to negative deflection angles when modeling a Kresling unit cell. The expansion at $\Phi = 0$ corresponds to the experimental data we observe and confirms the validity of using Taylor's expansion to measure the Poynting modulus of asymmetric samples.

While the crumpled cylinder has a semi-organized pattern that arises naturally from compression, resembling the Yoshimura cylinder, the randomness is still present in the pattern resulting in a more complex response. While we expected to obtain also a parabolic curve of the normal force, similar to that of Yoshimura, this was not the case. Instead, we observed quasi-linear relations of the normal force with the deflection angle with varying slopes, as shown for two different repetitions as example in Fig. 6.4AB. These linear relations resemble that of the Kresling cylinder, and thus are indicative of asymmetry in the crumpled pattern that results from the compression. These differences, as in Fig. 6.3 for Kresling and Yoshimura, would be completely omitted if looking only at the shear response. For the crumpled cylinders the shear responses are strikingly similar, but their normal force responses show even different signs, thereby remarking the importance of measuring the shear-induced normal response for a complete characterization of the mechanical response.

Since both the Yoshimura and Kresling cylinders' mechanical responses agree with the simulations of their unit cells, and therefore with their patterned designs, we would expect the crumpled cylinder response to depend also on the morphology of its crease patterns. However, for the crumpled cylinders the crumpled unit cells exhibit inherent randomness, and therefore, via image analysis of the crease patterns we can get an estimation for the asymmetry in the crumpled pattern. This relation of the normal force with the level of asymmetry in the crumpled pattern is further discussed below. For the crumpled cylinders we first tested large deflection angles, reaching 100 *mrad* as with the Yoshimura cylinder, however, we observed that the samples were sliding at the boundary conditions, rendering the data unusable. Therefore, we decided to limit ourselves to smaller deflection angles.

So far our results remark the usefulness of studying the shear-induced normal force responses to reveal the structural asymmetry and to better characterize the structural arrangement role on the mechanical response. In our particular case, where the materials present markedly ordered design, such as many origami samples, the effect of symmetry/asymmetry can be better understood via the coupling of shear and normal force. This is a topic that has received attention, mostly theoretically, for cylindrical samples presenting anisotropy, such as biological soft tissues [392, 393], but not yet for thin shells. This approach could also be used to understand the effect of orientation and internal rearrangements under shear in disordered bulk materials, such as crumpled balls [173].

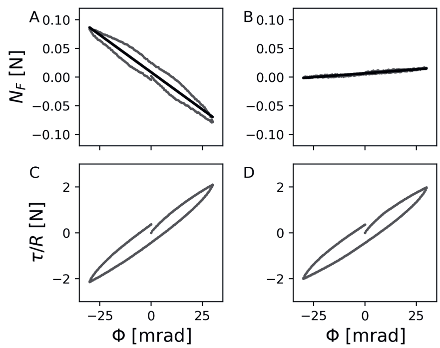

Figure 6.4: Upper row: example of shear-induced normal force responses of crumpled cylinder in two separate repetitions (A, B). Lower row: example of shear force responses upon shear for crumpled cylinder in two separate repetitions (C, D). Each shear force showed in the bottom row corresponds to the respective measurement of normal force in the upper row.

6

6.3.2 Shear and Poynting moduli

The results of the Poynting and shear moduli calculated for the Yoshimura and Kresling cylinders are presented in Figure 6.5A-C, where the values are re-scaled with the Y_{eff} from the compression test with a fixed upper plate before buckling. In order to prevent large relaxations of the sample during the torsional deformations, the sample was left to relax for 1 h before applying torsion at each gap. The lines correspond to the numerical results obtained modeling with unit cells.

The Yoshimura cylinder shows a positive Poynting modulus at gaps corresponding to $\varepsilon_c = 0$, as discussed earlier. If the compression level is increased, the Poynting modulus increases. This behavior is in agreement

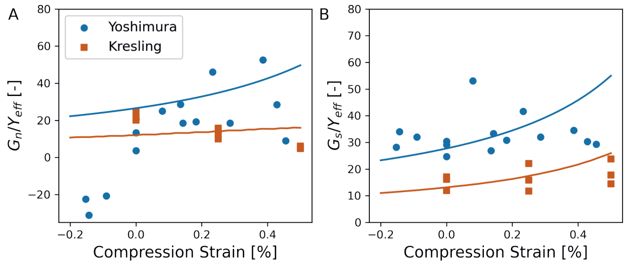

Figure 6.5: Poynting (A) and shear (B) moduli re-scaled by the effective Young's modulus before buckling. Solid lines indicate the numerical results of modeling the unit cells.

with the numerical prediction of our model, indicating that the stress during deformations is localized in the pattern of folds that form the unit cells except for large deformations, where the disagreement indicates possible buckling of the facets due to imperfections. Interestingly, if the Yoshimura cylinder was stretched to $\varepsilon_c < 0$ a negative Poynting modulus was obtained. Transition in the sign of the normal response in the shells can be rooted in the non-linearity of the system. We argue that the extension of the unit cells leads to variation in their elastic coefficients and makes them prone to local buckling when sheared. Such nonlinear behaviors also occur under large shear deformations, where local buckling of facets of the unit cells is expected, which are absent in our simple spring model. We should note that in our model, we only take the strain and the bending coefficients of the unit cells into account, which are constant values. Therefore, the transition in the sign of the normal response cannot be captured by our simple model.

For the Kresling cylinder, the Poynting modulus G_n/Y_{eff} is always positive for the studied gaps, and its magnitude decreases with decreasing the gap. These results therefore differ from the results of the model for the Kresling cylinder, which show a slight increase. The fact that the Poynting modulus for the Kresling cylinder decreases with increasing compression level (decreasing the gap size), can be better understood from the design of its unit cell. At ϵ_c, our cylinder has a $\Psi_0 = 57^o$,

6

which increases upon compression as mentioned earlier due to the torsion coupled with compression. This torsion is shown in Figure 6.6, which corresponds to the decrease of the gap between rheometer plates, with the upper plate being free to rotate and deflection angle being recorded. This causes the unit cell to become gradually more symmetric, with Ψ gradually increasing. Therefore, the φ_0, moves further to the negative strain at each compression level, thereby decreasing G_n as calculated from eq. 6.2. Furthermore, from Fig. 6.6, it is shown that φ changes linearly at the beginning, but becomes sublinear by increasing strains, indicating also how, at larger compression levels, the torsion reduces. This can be translated to the shear-induced normal force in the vertical axis exhibiting less changes when the Kresling cylinder is oscillating by shear around such deflection angle, thereby resulting in the lower G_n/Y_{eff}. Nevertheless, despite the different tendency of the experimental results upon compression and the simulations, the magnitude of G_n/Y_{eff} is well captured by the numerical results.

While the Yoshimura and Kresling cylinders have remarkably different structures and different order of magnitude of normal forces upon shear, they exhibit similar normal force behaviour when their normal forces are re-scaled with their Y_{eff}. These results remark the effectiveness of rescaling by Y_{eff}, to compare the normal force response for different cylindrical origami designs.

When looking at the G_s/Y_{eff} (Fig. 6.5B), clear differences in the magnitude appear between the samples, where G_s/Y_{eff} of Yoshimura is larger than the Kresling. The behavior of both cylinders is very well captured by the numerical predictions as shown in Fig. 6.5B. However, for G_n/Y_{eff}, deviation between experimental data and prediction of the model occurs at the maximum studied strains due to buckling of facets. These local buckling at large deformations cannot be captured by our simple models of unit cells.

Negative Poynting effect (as we observed for the Yoshimura cylinder when the material is stretched) was observed mostly in bio-polymer gels [73, 370, 371, 376]. Besides that it has scarcely been reported in the literature for other systems. For example, in the study by Criscione *et*

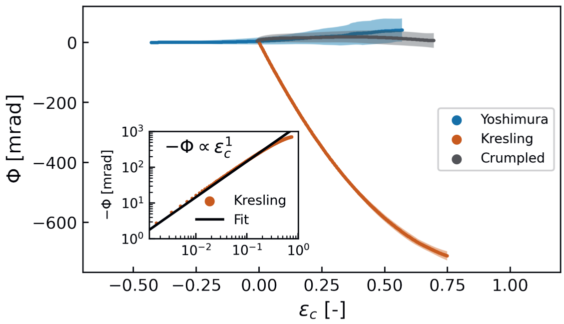

Figure 6.6: Deflection angle of the cylinders upon compression with the upper plate free to rotate. Inset shows the linear change in deflection angle for the Kresling cylinder with the compression strain ϵ_c. This indicates that the coupling between torsion and compression is linear.

al., [394], a negative strain of just 0.04, resulted in the reverse Poynting effect for rabbit papillary muscle, where the muscle fibers tended to shorten on twisting. The data from [394] was also supported later numerically in a study by Horgan and Murphy for anisotropic soft tissues, [395]. Kanner and Horgan, [396], showed that whether an incompressible isotropic cylinder elongates or shortens upon twisting depends on a transition value at strain $\varepsilon = \varepsilon_t$. If $\varepsilon < \varepsilon_t$, or the sample is stretched as in our negative strains, the sample tends to shorten upon twisting (negative or reverse Poynting effect), whereas at $\varepsilon > \varepsilon_t$, or when the sample is compressed, it tends to expand upon twisting (positive Poynting effect) [396]. These results have been validated recently also for isotropic rubber-like tubes [397]. Recently, Ghorbani *et al.*, [72], showed also how the couplings between shear and normal responses can be programmed by using rational design of cylindrical shell mechanical metamaterials. Our results demonstrate that the same is true for origami bellows.

Our results of G_n and G_s, ranging from negative to positive values show how these cylinders can be employed to tune the Poynting modulus, both in sign and magnitude, using the compression level or the orientation of the unit cells. Unfortunately, for the crumpled cylinder we could not obtain values for the Poynting modulus, due to the asymmetries present in the crumpled pattern as mentioned earlier, and will be discussed in the next section.

6.3.3 Pattern analysis of the crumpled cylinder

As mentioned in the introduction, one limitation of origami (or other mechanical metamaterials) is their sensitivity to defects and the role imperfections play on designs of well arranged unit cells [128–130]. A possible solution to these geometrical limitations is to design crumpled structures with randomness in their design, e.g. the crumpled cylinder presented here. Such structures are more adjustable to specific shapes and curvature and less sensitive to imperfections [277]. Crumpled structures are, however, still poorly understood and most of the research on these structures has been focused on uniaxial or isotropic compression of bulk crumpled materials [57, 171, 277, 284]. Only very recently shear response of bulk crumpled materials have been studied [173]. To exploit the advantage of crumpling for designing robust origami structure crumpled origami structure with semi random patterns should be designed. The introduction of crumpling to origami to form so-called origami crumpled surfaces [278] has been used in the past only for artistic purposes, but could provide a new way to design mechanical metamaterials which contain some structural disorder in their periodic patterns. In this section we attempt to study how the semi-random crumpled pattern of our crumpled cylindrical shell affects its mechanical response.

Based on the results of Fig. 6.4, we studied the relation between level of symmetry in the crease pattern of crumple network with the observed mechanical response for several crumpled cylinders. To determine the level of symmetry in the crease patterns we performed an image analysis, and tried to connect the results to its mechanical response. In order to test the validity of our image analysis method, we first studied the well defined patterns for the Kresling and Yoshimura cylinders. The results are shown in Figure 6.7. By applying a 2D Fast Fourier Transform on the image (Fig 6.7, top row), we obtained an FFT frequency spectrum, which we then transferred to an FFT alignment plot via an azimuthal summation (Fig. 6.7, bottom row), as performed in [173] for cross sections of crumpled materials. We checked the method for the asymmetric Kresling pattern, and could confirm that the resulting peaks in the FFT alignment coincide with the angles of the patterns. Furthermore, we tested the method both in the digital fold , before folding, and in cylinders opened after being measured in the rheometer. Using the cylinders after being cut and opened results in the same location of the peaks as the computer based images, but with more noise in the image due to imperfections and lightning effects, validating the method to be used also in cut and opened crumpled cylinders.

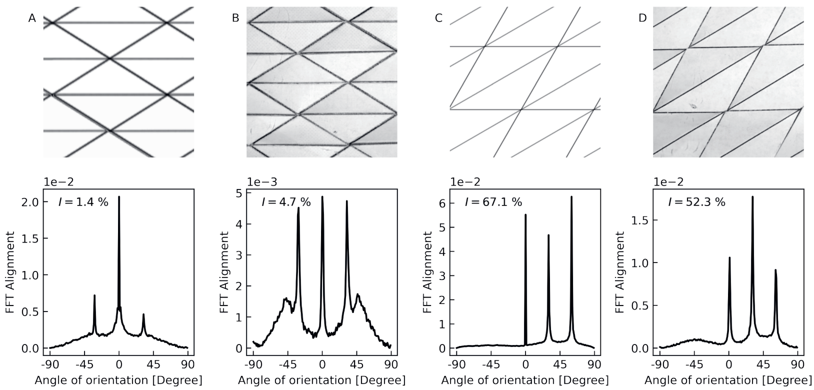

Figure 6.7: Image analysis as measured from the pattern directly on the computer image, or from the opened cylinder of the Yoshimura (A: computer image, B: opened cylinder) and Kresling designs (C: computer image, D: opened cylinder).

When we measured the pattern of creases from the crumpled cylinder (See Fig. 6.8), we observed a distribution, rather than well defined peaks. The distribution was centered at 0^o, and spread almost from -90^o to 90^o, with the distribution decreasing rapidly around $< -45^o$ and $> 45^o$. This means the crumpled pattern shows a distribution of creases that range (approximately) from -45^o to 45^o, with the most abundant orientation being flat lines at $\approx 0^o$. As the crumpled cylinder is formed by compressing uniaxially, it is not surprising that the most creases are found as horizontal lines. In fact, from Fig. 6.6, we observed that when the cylinder is compressed with a free to rotate upper plate, the deflection angle remains close to zero, indicating no torsion induced by the compression, which supports this distribution to be centered around $\approx 0^o$

The asymmetry of the pattern was calculated based on the areas under the distribution curves below and above 0^o, as indicated in eq. 6.5, resulting in an asymmetry index in %. This asymmetry index, I, was then linked to the slope of the F_N vs. Φ curve (Figure 6.8). For a symmetric structure such as Yoshimura, we expect a quadratic relation between normal force and deflection angle with either a positive or negative Poynting moduli. Whereas an asymmetric structure, such as those from the Kresling origami cylinder, would results in a linear response. For our crumpled cylinders we see responses similar to the Kresling origami cylinders, indicating asymmetry in their structure. To understand it better we plotted the slope of the F_N vs. Φ curves as a function of the asymmetry index for seven different cylinders (Fig. 6.8), where we found a good correlation. The individual mechanical response and the 2D FFT alignment plots for the seven cylinders are provided as Supplementary material. Figure 6.8 shows that with increasing the asymmetry index, the slope increases as well. Looking at the uniaxial compression results (Fig. 6.6) or shear responses (Fig. 6.4CD) we do not see significant differences or clear correlations with the asymmetry index. This indicates that the shear-induced normal force is more sensitive to the asymmetry in the structure, while the uniaxial compression results or shear resistance fail to probe the asymmetry in the semi-random structures.

These results, to the best of our knowledge, are the first attempt relating the crumpled structure pattern to its mechanical response under shearing deformations, and indicate that using a simple asymmetry index obtained from image analysis of the patterns, the level of asymmetry in the mechanical response can be predicted to a large extent. These findings can find applications across diverse disciplines. For instance, this approach might extend into areas such as tissue engineering, where random cells, without a clear anisotropic orientation [398, 399], could be analyzed via simple image analysis, to predict the resulting shear-induced normal force response.

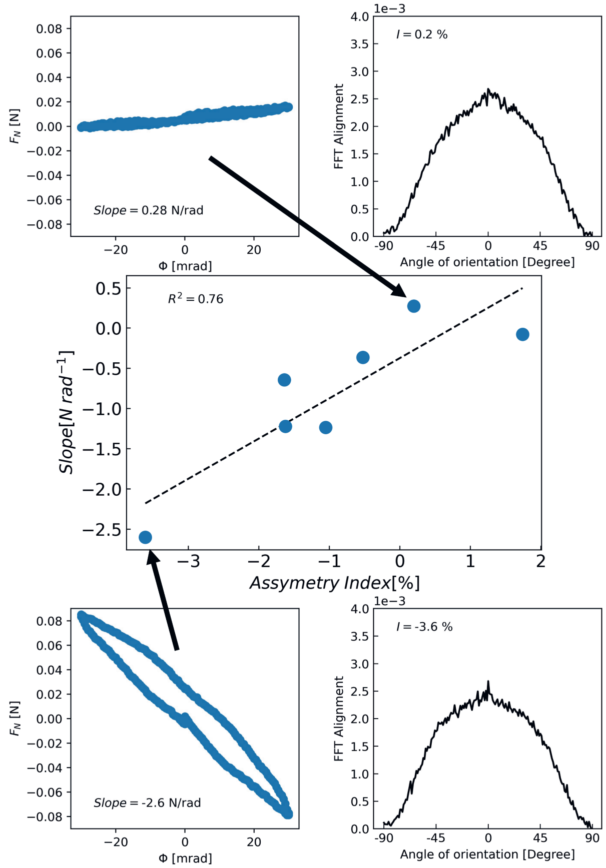

Figure 6.8: Relation between the slope of the mechanical response, and the asymmetry index calculated from the image analysis. Two of the individual tests are included as examples.

Although the asymmetry index of the crumpled patterns predicts the asymmetry in the normal force behavior it does not fully explain the normal force behavior. As discussed in [173], for bulk crumpled papers, force chains can arise due to long range correlations and/or due to formation of large creases. A similar story can be valid for the crumpled cylinders, as all the creases are not likely to play the same role in the mechanical response, and some paths through the network of folds would contribute more to the normal force response than others. Therefore, it would be necessary to determine the stress focusing regions in each of the individual crumpled unit cells to fully understand the normal force response of the crumpled cylinders. However, this is beyond the scope of the current study and offers interesting directions to further elucidate the mechanical behavior of crumpled mechanical materials in future studies.

6.4 Conclusion

In this paper we studied the shear and shear-induced normal stress of three types of origami bellows: Yoshimura (symmetric), Kresling (asymmetric), and crumpled cylindrical shells (semi-random). All cylinders present levels of structural order, with different levels of symmetry (with respect to the shearing direction) and randomness. We show how, by changing the orientation of the unit cell, and therefore changing the symmetry, we can change and tune the Poynting effect (shear-induced normal force) while the shear response remain almost the same.

The normal force response of the symmetric Yoshimura cylinder upon torsion was successfully fit with a quadratic relation, whereas the normal force response of the asymmetric Kresling cylinder was well captured with a linear Taylor's expansion of the Poynting equation at $\phi = 0$. The experimental results of shear and shear-induced normal forces of both origami bellows were well captured by a simple spring model except for the normal force of the Kresling cylinder, due to stress localization in the pattern of folds at large compression levels.

Interestingly, while a symmetric response was expected for the crumpled cylinders due to the resemblance to a Yoshimura pattern, we found slight asymmetry in the distribution of crease angles that was successfully detected via image analysis, and quantified with a simple asymmetry index, I. We linked the mechanical response to the structure by showing that I is correlated with the slope of the normal force response, indicating that the slight asymmetry in the distribution of the crease angles results in asymmetric shear-induced normal force response. This approach may provide a platform for other disciplines (e.g. tissue engineering) to predict the shear-induced normal force responses of random structures such as tissue, by analyzing the orientation distribution of cells.

Our results pave the way for programing the shear and shear-induced normal force response of origami bellows and the coupling between the torsion and compression, based on the geometry of the unit cells. We also showed that structural imperfections in crumpled cylinders control the normal force response under torsion. These finding are essential for designing robust origami bellows for diverse real life applications from soft robotics to sustainable packaging materials or medical origami devices.

6.5 Supplementary Material

Table 6.2: Results for energy dissipation (E), effective Young's modulus (Y_{eff}), spring constant (K), and spring constant per unit cell (k). Name of the cylinders abbreviated as: Crumpled (C), Kresling (K), and Yoshimura (Y).

Sample	E [J]	Y_{eff} $[Pa]$	K $[Nm^{-1}]$	k $[Nm^{-1}]$
Y Free	0.011±0.001	1378.15±107.95	40.24±3.15	80.47±6.3
Y Fixed	0.012±0.001	1477.13±234.35	43.13±6.84	86.25±13.68
K Free	0.007±0.002	536.0±46.08	7.84±0.67	7.84±0.67
K Fixed	0.135±0.011	5115.64±2247.06	74.85±32.88	74.85±32.88
C Free	0.17±0.01	12462.75±1512.41	72.66±8.82	137.58±16.7
C Fixed	0.151±0.045	11402.88±1731.54	66.48±10.1	125.88±19.12

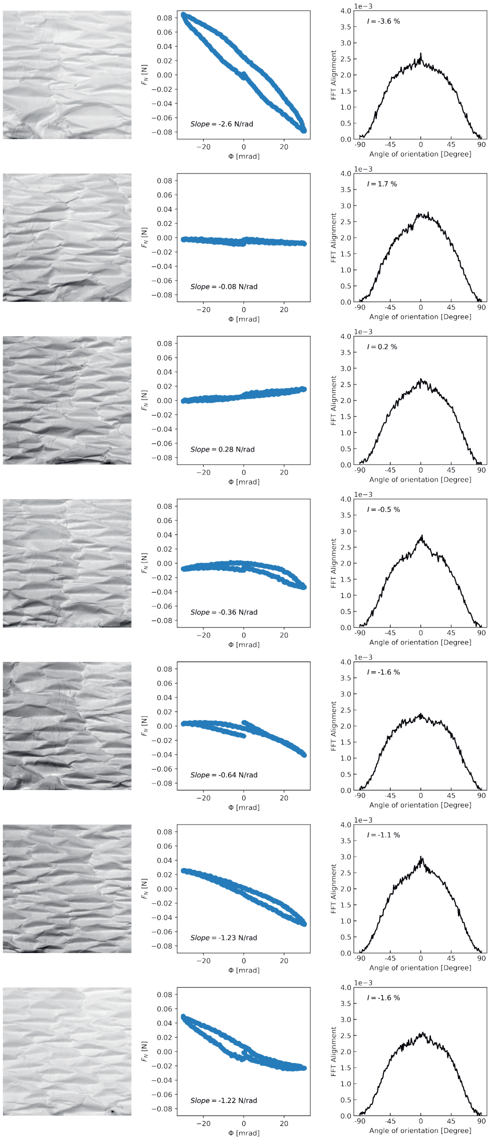

Figure 6.9: Individual repetitions of the mechanical response and image analysis of the crumpled cylinders.

Chapter 7

General discussion

In this final chapter, we present the main results of this thesis and discuss them from an integrated perspective. We also address the implications of our findings from a food science perspective and provide examples of possible future applications.

7.1 Objectives

Understanding how different materials respond under deformations is a paramount necessity to effectively use such materials in real-world applications. From the ongoing quest to find new mechanical metamaterials which exhibit interesting properties, to the protein transition towards more sustainable food products, all fields require a deeper understanding of structure-property relationships to develop and optimize new products. In the case of macroscopically disordered metamaterials, in practical applications, the systems will have to sustain deformations of all kinds. However, these systems are mostly studied under uniaxial deformations, and shear deformations are often ignored. Ignoring the response of these systems under shear can not only cause safety concerns due to material failure, but it also misses the opportunities to exploit their peculiar shear behavior. On the other hand, for ordered structures, studying shear opens avenues for designing new functional materials by elucidating the interplay between structural components under deformations.

In this thesis, we aimed to investigate the shear response of materials containing different ordering level at the macroscopic scale, and relate the response to their structural components. We do so by investigating the systems extensively under direct shear using rotational shear rheometers, focusing on the nonlinear responses. In some of the chapters, shear rheology was also combined with simulations and/or image analysis to better understand the role of particular structural components or topological constraints.

7.2 Overview of the main findings

In this section, we first highlight the main findings of this research. Then, in the next section, we will explain the relation between each chapter and the relevance of each system in a broader perspective. In Figure 7.1 we summarize the systems we studied in this thesis. In the figure we schematically depict the type of deformation studied in each chapter, and how their main structural components locate in the space from disordered to ordered.

In **Chapter 2**, we started by reviewing the state of the art in crumpled materials from an amorphous solid perspective. By doing so, we provided an overview of the interesting characteristics that these systems contain. Crumpled materials are the perfect example of a disordered system, which still lack a clear physical understanding, despite being largely present in our daily lives. The simple act of crumpling a sheet of paper into a ball results in a highly complex structure with inherent randomness in it, and represents a case of highly non-linear physics. When crumpling a paper sheet, we embed a 2D planar shape into a confined 3D space, creating a fractal structure and causing frustrated regions. This causes the crumpled structure to be in a metastable state, where there is a complex energy landscape with local minima that prevent the structure from reaching a global minimum. As a result, the system presents a complex relaxation which has been fit previously in the literature with both stretched exponential and logarithmic models. Both of these relaxation models are amply used for studying also the relaxation dynamics of glassy disordered systems, and other out-of-equilibrium systems such as emulsions, gels, or granular materials.

However, a striking difference between crumpled materials and the other mentioned out-of-equilibrium systems is the scale of its components. In the case of glassy materials, such as those formed by entangled polymers, or colloidal systems, the components are usually at the microscopic or nanoscopic scale, whereas in crumpled materials, the components are at the macroscopic scale. Therefore, this difference makes crumpled systems excellent candidates to study disordered solids, having

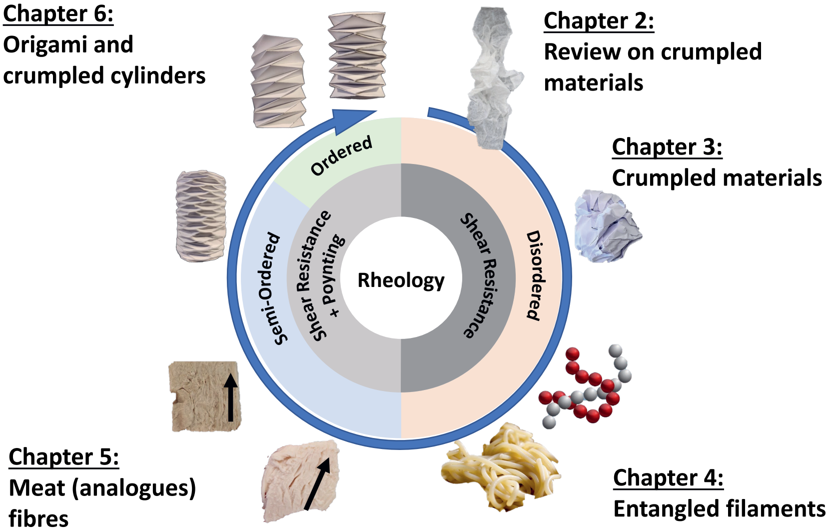

7

Figure 7.1: Overview of the chapters in this thesis and their interrelationships. The inner layer of the wheel diagram shows the type of deformation we used to study each material. The outer layer shows how each chapter is placed from disordered to more ordered arrangements. The pictures indicate the relevant structures of each chapter.

the components much more easily accessed. After reviewing crumpled systems, we provided examples to introduce disorder via crumpling in the design of mechanical metamaterials to create new disordered metamaterials. Such designs are inspired by a bottom-up approach, where crumpled unit cells can be combined to form a mechanical metamaterial, thereby harnessing benefits from crumpled materials such as lower sensitivity to imperfections, while still having systems which are not completely disordered as crumpled bulk materials.

In **Chapter 3**, we studied bulk crumpled materials under shear deformations, which have been largely neglected in previous studies of crumpled materials that used uniaxial or isotropic compactions. Crumpled materials are disordered arrangements of frustrated regions created through random crumpling, and thus formed through bending deformations where the stress is focused in narrow regions where the material yields. During shear deformations, the total density within the crumpled structure remains unchanged in between the parallel plates. Therefore, the mechanical response can be more easily attributed to the movement (or lack thereof) of the internal structures in the crumpled systems. We studied the role of different parameters, i.e. compaction level, sheet training, internal orientation, friction, and plasticity on the shear response. We unraveled how large creases contribute to the creation of force chains, analogously to granular systems, which are decreased by training the paper sheets. Regarding the internal morphology, internal layers parallel to the shear direction resulted in layers sliding over each other, thereby increasing the dissipation compared to layers perpendicular to the shearing plane. Decreasing the friction coefficient of the system facilitates the internal rearrangement of energy-focusing regions. Understanding how the different parameters play a role in the deformation of crumpled materials allows for the fine-tuning and programming of desired responses for practical applications.

In **Chapter 4**, we investigate another fully disordered system: entangled quasi-1D filaments, which in our case consist of granular chains and ropes. As in the case of crumpled materials, where similarities have been drawn in the literature with microscopically disordered solids, the same holds for granular chains. Systems such as granular chains have been used in the previous literature as macroscale analogues of linear polymers to study the effect of topological constraints. And, as with crumpled materials, these systems have been studied under uniaxial deformations, but the shear resistance has been largely neglected. We studied the deformation mechanics under shear, combining shear rheology with image analysis through particle image velocimetry and simulations. We observed a transition from narrow to wide shear zones, which followed a sigmoid curve. We found the width of the sheared area to scale with the length of the chain. Furthermore, the entanglements go from "inactive" in small deformations, to system-spanning "active" in large deformations. At deformation amplitudes where the entanglements are active, we found the stiffness of the system to increase in a power-law manner with the chain length, similarly to polymers.

In **Chapter 5**, we studied whole cut meat samples and plant-based meat analogues of whole cuts. Effectively, this is a system where we increased the order of the basic components in **Chapter 4**: quasi 1D filaments. For meat whole cuts, the filaments are arranged naturally in a particular order within skeletal muscle, whereas for plat-based analogues (soy protein or pea protein mixed with wheat gluten), the structuring process using shear cell technology results in oriented fibrous structures. In both cases, the orientations result in clear anisotropic structures. Via shear rheology, we studied the mechanical response of the samples, taking into account the orientation of the fibrous materials. In addition to shear resistance, we also studied the normal force response to provide a complete mechanical characterization of the sample. Similarly as observed in **Chapter 3** for crumpled materials, we found that the orientations perpendicular to shear result in higher storage moduli, except for the sample with pea protein isolate-wheat gluten, which shows a less marked anisotropic structure. The LAOS methodology allowed us to infer the effect of stronger fibers in meat and the rearrangements occurring at intermediate strains. The more elastic meat fibers also exhibited a larger normal stress response (larger Poynting modulus) and showed large differences in magnitude between different fiber orientations. Therefore, we provided a robust methodology to quantitatively compare whole meat cuts and meat analogues using a combination of shear and normal stresses.

In **Chapter 6**, we studied the more ordered version of the structural components of **Chapter 3**: creases and vertices created by folding a planar shape. We used well-known cylindrical origami designs based on similar unit cells, but being either symmetric (Yoshimura) or asymmetric (Kresling) with respect to the shear direction. This allowed us to observe how the samples exhibit a comparable response in shear force but a radically different shear-induced normal force response. Then, we compared a third type of cylinder that we called crumpled cylinder, made by compressing a paper cylinder, which results in a semi-random pattern of folds arising as a result. We analyzed such pattern or folds via image analysis, and found it to have a good correlation with the shear-induced normal response of the crumpled cylinders, which evidences how the stress is localized in the folds. Therefore, these results facilitate the development of new mechanical metamaterials based on origami bellows and the use of the fold pattern to program the shear-induced normal response.

7.3 Linking shear response to structural components

A common theme encompassing all the chapters in this thesis, as just summarized, is the use of shear rheology to understand the role structural components play in different complex materials. The role of such structural components is inferred from the different stress and/or strain localization in the varied systems, from disordered to ordered arrangements. In this section, we put the results of the thesis in a broader context.

7.3.1 Disordered materials

The study of the deformation of amorphous (disordered) materials that exhibit solid-like behavior has a rich history and encompasses a wide range of materials such as glassy polymers, dense colloidal suspensions, metallic glasses, or biological substances [9]. On the other hand, for completely ordered simple crystal lattices, the lattice dynamics framework provides a good connection between the macroscopic properties and the atomic-level structure [1]. In crystal lattices, a line defect in the form of dislocation is the major deformation mechanism [400]. However, our understanding of the basic deformation event is still limited in systems with significant structural disorder, such as glasses, liquids, emulsions or foams; also known as amorphous solids [401, 402]. For amorphous solids, a similar concept was proposed in analogy to dislocations, the shear transformation zone (STZ) [403], based on previous works on flow-defect theories in metallic glasses [404]. These STZs consist of compact areas, with possibly as few as five to ten particles, in specific spatial configurations that make them more vulnerable to undergo plastic rearrangements upon external stresses than surrounding particles [403]. This defect can be seen as a basic deformation unit or plastic event [405]. One problem is that STZs are not clearly observed under high-resolution electron microscopy, as are the dislocations in crystals [406].

The current theory on STZ introduces a notion of (configurational) effective temperature, T_{eff} as an internal variable, characterizing the state of the material. This effective temperature is then $T_{eff} = \partial U_C / \partial S_C$, with U being the configurational energy of the subsystem, and S its entropy [9]. The concept of effective temperature was developed early on also for athermal systems first by Edwards in his development of statistical mechanics of granular systems [230]. Later, as we indicate in our review in **Chapter 2**, the concept of effective or configurational temperature has also been applied to crumpled networks [170, 229, 238]. In fact, STZ, while extensively researched for disordered *thermal* systems where temperature plays a role, have also been studied for *athermal* systems [407]. At the core, the STZ assume configurational hot spots at the mesoscale, which are more prone to deformation under external stress than the surrounding material [407]. To some extent, this is effectively the same as we observed in **Chapter 3** when shearing the crumpled materials. To perform rearrangements, there is some energetic cost such as frictional interactions [408]. By reducing friction as we did with starch powder, energy foci or energy-focusing regions can move more freely (see Figure 7.2), thereby remarking the resemblance of these areas of localized deformation to STZs. This rearranging of energy foci regions was also previously mentioned for crumpled materials under compression both in simulations [187] and experiments [190]. Therefore, shearing causes local rearrangements, facilitating that the system explores neighboring metastable states, analogously to how temperature would excite molecules in *thermal* disordered systems to other metastable states [408].

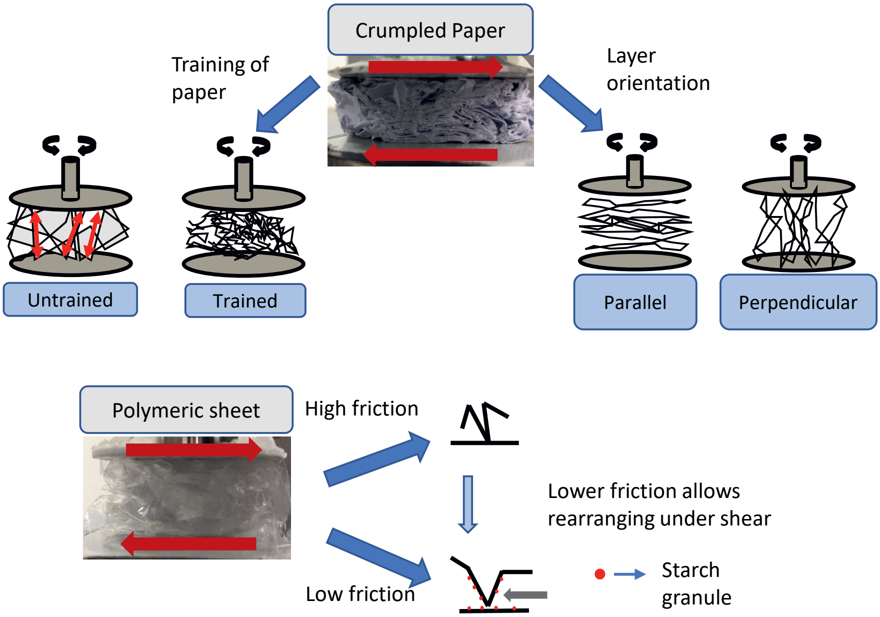

Figure 7.2: Schematic depiction of some of the parameters studied in **Chapter 3**. Part of the graphical abstract used for the publication of the chapter in [173].

In addition to the effect of friction, in **Chapter 3** we also studied the effect of internal morphology and training of the material on the shear deformations. In both cases, we also observed the effect of strain or stress localization. When the internal morphology was parallel to the shear direction, which appears naturally perpendicular to the uniaxial compression after random crumpling [259], we observed the effect of sliding between layers when sheared. This then indicates localizations of strain, which cannot extend to large areas, since the parallel orientations are still located as inhomogeneously distributed stacks, as indicated earlier in literature [259] (See also Fig. 7.2 for the cross-section of crumpled paper at the rheometer). Furthermore, when the strain localization grows enough to form shear bands, previous literature on LAOS has reported the presence of an overshoot in the instantaneous shear stress in the elastic Lissajous curves for worm-like micellar solutions [409], polymers [410] and soft glassy materials [411], which we did not observe. Similar phenomena of strain localization in layers occurs at different length scales. For example, when studying large deformations of calcium silicate hidrates (which form both crystalline and amorphous regions), using simulations the authors in [412] found the strain to localize in interlayer spaces with higher water content, which screens the ionocovalent interactions of the calcium silicates.

In the case of training the material, we hypothesized that the untrained paper presented force chains, which were reduced to a great extent upon training due to the development of a more extensive network of creases and vertices. Force chains are known in other domains to be filament-like regions where the stress is concentrated and have been found in disordered systems as varied as granular materials [413], emulsions [414], foams [415], microbial populations [416], or dense active matter with self-propelled particles [417]. The presence of local rearrangements in crumpled materials, together with strain and stress localization, remarks the example of these systems as a paradigm of complexity, which can be used as a macroscopic model to understand deformations in other amorphous solids.

It is important to note that, while we remark similarities in strain localization in crumpled materials with other amorphous solids, STZs have a microscopic character, and thus we do not intend to claim the presence of STZ in crumpled materials. Nevertheless, STZ have also been used to explain the microscopic physical basis of large-scale events, such as fault gouge causing earthquakes [418]. Daub & Carlson [418] explained how with the STZ theory, dynamic rupture causes spontaneous formation and growth of shear bands, thus providing a description of fault friction based on an effective temperature quantifying configurational disorder. Tectonic earthquakes are different from other types of earthquakes in that they exhibit shear banding effects in addition to seismic vibrations. These shear banding effects can account for up to 90% of the total energy released during the earthquake [419]. In the case of other microscopic disordered materials, STZ *can* explain the spontaneous formation, and subsequent growth of shear bands [407, 420]. Shear bands are a form of strain localization, where the strain can take much larger values than in other zones of the sample. The formation of shear bands is a known phenomenon found extensively in complex fluids, such as polymeric fluids or soft glassy materials [421]. This phenomenon of strain localization is what we studied in **Chapter 4**, with the effect of chain length on the shear rheology of granular chains and spaghetti.

For granular systems, marked rigid regions usually form upon yielding, separated by narrow shear zones, or shear bands, where the strain is localized [317, 318] (see Figure 7.3 AB). Wider shear zones can also arise when shearing the bulk material away from the boundaries [319, 320]. But this behavior is different in the case of disordered assemblies of quasi-1D objects. This is because for frictional granular materials, the shear banding can be explained by considerations of energy dissipation [321, 322]. However, the yielding and shear banding formation for longer, filament-like objects is much less known. In the case of linear polymers, the molecular weight (analogous to the chain length in **Chapter 4**), has been observed before to affect the shear banding phenomena as well. Shearing entangled solutions of low molecular weight polybutadiene (PBD) (1.5 $kg\ mol^{-1}$) wall slip was observed, and thus the stress is not well transferred to the whole sample in the gap. On the contrary, with entangled solutions of high molecular weight PBD (10 $kg\ mol^{-1}$) reduced the slip length, and shear bands appeared in the bulk, indicating the higher transfer of stress to the bulk [422]. This is similar to what we observe with macroscale chains.

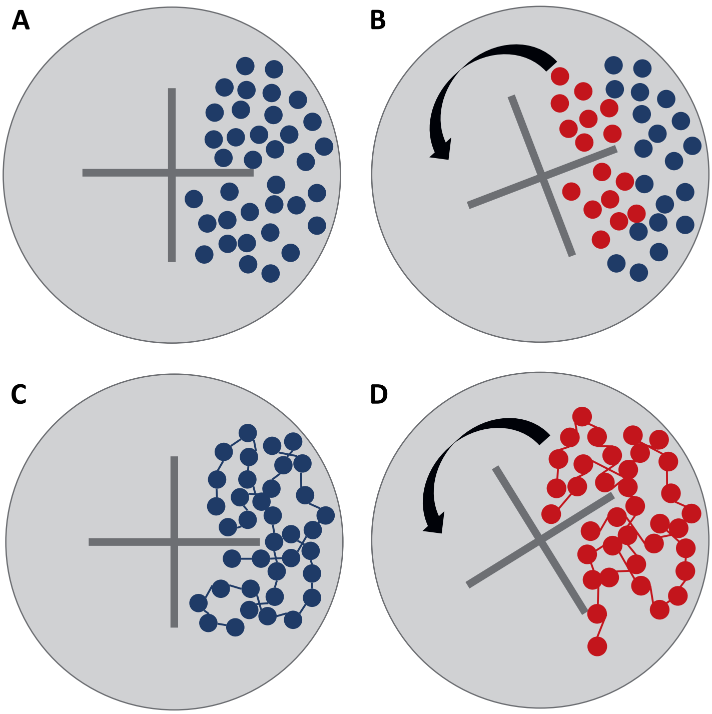

7

Figure 7.3: Schematic depiction of the stress localization in a sample with monomers before (A) and after shear (B), and in a sample with long chains of linked monomers before (C) and after shear (D). Scheme depicted with a four-blade vane geometry as experiments in **Chapter 4**. In blue are indicated the monomers which do not experience stress, and in red the monomers which experience stress.

By analyzing the velocity profiles of the sheared samples in **Chap-**

ter 4 we observed the transition from narrow shear zones in small deformations to wide shear zones in large deformations. This transition followed a sigmoid curve, where the plateau radius at large deformations was lower for the granular material, indicating indeed the narrower shear bands mentioned above. When the chains were longer, the sheared region could extend until the beaker walls, which can be seen as wider shear bands (Figure 7.3). This indicates how, when topological constraints are present in disordered assemblies of semiflexible objects, the stress is more distributed along the network of entanglements, in opposition to the localized yielding and dissipation of the granular systems. We found scaling relations for the width of the area being sheared, as well as the width of the transition from narrow to wide shear zones. Interestingly, both of these relations scaled with $\sqrt{N}$ (with N being the chain length); positively in the case of the shear zone width and negatively for the transition width, i.e., longer chains had sharper transitions. In the case of polymers modeled with flexible chains, the radius of gyration also scales with $\sqrt{N}$ [6]. Therefore, this suggests that for our macroscale models, the topological constraints become active in LAOS deformations along the entire chain length and that these scale as a "radius of gyration" of the macroscale chains.

7.3.2 Ordered materials

In **Chapters 5** and **6** we studied more ordered versions of the previous chapters, but strain or stress localization was still present in our experiments. When studying ordered arrangements of quasi-1D filaments, such as the fibers arranged anisotropically in meat and plant-based meat analogues, the effect of entanglement was not considered, as the formation of knots, loops, or interlocking is not possible. Instead, we observed that the stress was localized in different regions, depending on the sample. For the meat samples after cooking, which contained strong shrunken muscle fibers, we observed by the dissipation ratio that some rearranging ocurred at intermediate strains, meaning that the strain was localized in the connective tissue between the fibers. This was related to the connective tissue having been degraded during cooking [382], allowing the sliding between the fibers in a similar way to how we observed sliding in stacked layers of crumpled papers in **Chapter 3**. But, since in a rotational motion the fibers cannot slide indefinitely due to the twisting motion, at increasing strain the fibers start being deformed, thus resulting in a stress localization in the fibers. This leads to the observed intracycle stiffening in the Lissajous curves and increase in normal force perpendicular to shear. Our elastic Lissajous curves for the cooked meats, which contain elastic fibres as mentioned, look similar to those observed also in LAOS deformations for mozzarella cheese [48]. Mozzarella cheese is a type of pasta filata cheese, also called stretched or pulled curd, which due to its mode of fabrication also contains a macroscopic fibrous protein network. Therefore, observing intracycle strain stiffening in the results of [48], for mozzarella samples positioned perpendicular to the shear direction, agrees with our results indicating fiber elasticity.

As happened with the shearing of crumpled papers in **Chapter 3**, when the orientations are perpendicular to the shear direction, beef showed a lower dissipation and a higher storage modulus G'. This remarks the importance of considering structural components for understanding the shear response of various materials. For both beef and crumpled papers, we observe a stress localization in orientations perpendicular to shear that result in a lower dissipation with respect to orientations parallel to shear. When the samples are parallel to the shear plane, the structural components can slide, thus exhibiting strain localization.

In contrast, for the fibrous plant-based analogues, the connective tissue is not present, and as a result, we do not observe rearrangements nor increase in dissipation at intermediate strains. The samples behave more solid-like until larger strains, when the stress localization in the fibrous structures starts breaking them, indicating weaker structures than the whole cut meat samples. For understanding the differences observed between the meat analogues and the plant-based fibrous structures, the use of non-linear rheology was essential. If one were to compare the linear G' and G'' of the two different types of samples, most of this information would be missed, only finding the cooked meat to behave stiffer than the plant-based fibrous structures.

A similar situation happened in **Chapter 6** with the origami shells that we studied. When comparing the Yoshimura, Kresling, and crumpled shells, studying only the linear shear response of the different designs would render little information beyond the differences in stiffness (G). The case of the Kresling cylinder is notable, where the rotated cells result in anisotropy and asymmetry with respect to the shear direction. This would normally result in different stress responses in the negative and positive shear directions, which we did not observe, as Kresling showed the same shear force response curve as the symmetric Yoshimura cylinder. However, when combined with the study of nonlinear shear-induced normal stress, we could find clear differences between the samples, attributing these differences to the different types of unit cells present for Yoshimura and Kresling, as also shown by the numerical results. For the crumpled cylinder, we found a good correlation between the level of asymmetry in the pattern and the asymmetry in the normal force response. These findings remark, as was the case in the previous chapters, the stress localization in specific regions of the samples when sheared.

The stress distribution in origami is a well-studied phenomenon via numerical simulations [50, 386, 423], where most simulations show the localization of stress in the networks of folds. This is also true in our samples, where the modeling of unit cells using springs is in good agreement with the shear and shear-induced normal stress responses. In the case of the crumpled cylinder, the fact that we observed a good correlation between the pattern asymmetry and the mechanical response confirms that the stress is mostly localized in the crumpled folds. However, it is important to note that the specific path in which the stress accumulates is not known, and some folds will likely play a larger role in bearing stress than others. We observed this phenomenon in **Chapter 3**, where crumpled papers formed force chains in which stress accumulated.

7.4 Structural components applied to foods

It is well known that structures in foods play an important role in how we perceive foods. An important aspect from the point of view of food physics is how structural components and ingredients affect the texture of foods. Structuring processes allow us to go beyond what ingredients alone and formulation provide [424, 425]. A clear example of this is mozzarella cheese. Despite differences in milk (animal) origin, there are only minor differences in the formulation of the ingredients in cheeses, but vast differences in the fabrication processes result in different types of cheese. In the case of mozzarella, the pulling of the curd results in macroscopic structures of the casein protein fibers, as mentioned earlier, which creates a completely different sensory experience upon consumption from other cheeses, such as cheddar cheese [48]. Although the aroma and taste of foods involve the interaction of receptors with specific molecules, the texture of food is perceived by vision and touch (also oral processing) [425]. According to the ISO vocabulary for sensory analysis, texture is defined as "all of the mechanical, geometrical, surface and body attributes of a product perceptible by means of kinaesthesis and somesthesis receptors and (where appropriate) visual and auditory receptors from the first bite to final swallowing" [426]. In other words, we perceive structures in foods.

Many of the structures we studied in this thesis can already be found in foods and therefore offer starting ideas to develop new food products or packaging. For example, crumpled structures, which we studied in **Chapter 3** can be found as crumpled chocolate structures found in the famous Cadbury Flakes product, [427]. Although the website states that its fabrication process is a well-protected secret, there are several available videos demonstrating how to recreate the structures by scraping a thin film of chocolate, which results in wrinkling and crumpling of the chocolate to create the airy structures [428]. When the cream layers of cow milk are deposited onto a surface, they crumple into a state of low volume fraction [429]. Therefore, crumpling offers a way to create lightweight structures in foods. When it comes to culinary molds, designs have been proposed in the past inspired by crumpled papers [430]. At the same time, crumpling consists of embedding a 2D structure into a 3D space, and thus consists of a large surface area for its volume. This means that crumpled morphologies offer a good system for controlled release, as shown with crumpled graphene used to deliver the antibiotic vancomycin [431], and could be adapted for controlled release in foods.

In **Chapter 4** we studied quasi 1-D filaments. A common hot topic for discussion at the dinner table that involves quasi-1D objects is regarding whether or not to break spaghetti before boiling. With shear deformations, we showed how having longer chains or ropes results in an "activation" of the entanglements, which can be translated into the effect of twirling the spaghetti with the fork to collect more sample. But spaghetti are not the only filaments found in foods. Another food structure formed by entangled filaments is cotton candy, and in recent years it has attracted the interest of several chefs to design novel dishes, both sweet and savory [432]. Therefore, the information from **Chapter 4** can also help to achieve novel textures with cotton candy-like structures, understanding how entanglements play a role in such configurations.

In **Chapter 5** we have already discussed the presence of 1-D filaments present as oriented fibers in meat and shear-cell structured plant-based fibrous samples. Today, the transformation of sustainable ingredients, such as wheat and pulses, is already underway, as can be seen from the large volume of plant-based meat analogues that appear in the supermarket. With the methodology that we proposed in **Chapter 5** measuring both the shear resistance and Poynting modulus, we successfully quantified differences between samples that have different orientations, as well as different types of fiber. Therefore, this method can aid in the current protein transition by allowing for clear comparison between samples with different formulations, origin (such as cultured meat), or structuring processes. Furthermore, with the rise of 3D printed structured foods, the presence of filaments resulting from the nozzle at the printing will play a role in the mechanical response of such products [433, 434], and thus the methodology proposed in **Chapter 5** can provide valuable insights.

While in **Chapter 6** we studied origami (or crumpled) designs and thus the most logical applications are regarding food packaging, such as a Kresling-inspired wine bag shown in [435], there are also applications to food itself. As just mentioned in the previous paragraph, there is a rise in 3D printing food products, but some researchers are already studying the so-called 4D printing. This essentially consists of a 3D printed product, which contain as 4^{th} dimension the time, meaning that the 3D printed shape will change over time, for example, with external stimuli [436, 437]. In this regard, designing origami shapes which, upon heating or altering the pH of the medium, changes shape, would benefit from the results in **Chapter 6**. Understanding how the unit cells in such structures localize the stress upon external deformations would greatly aid in designing appropriate shapes, even in the case of semi-organized configurations as our crumpled cylinder.

7.5 General conclusion

Understanding the structure-properties relationship in complex materials is essential for using such materials in practical applications. In this thesis, we have employed nonlinear shear rheology extensively to elucidate the role that diverse structural components play under deformations. In some of the chapters, shear deformations were also combined with image analysis and simulations to clearly recognize the structures present in the samples. From completely disordered materials, such as crumpled systems and entangled assemblies of filaments, to ordered arrangements such as anisotropic fibers in meat and anisotropic folds in origami, nonlinear shear rheology sheds light on the material's behavior. Each chapter focused on different aspects of these systems and explored the effects of various parameters on their mechanical response.

In the case of completely disordered materials, the large amplitude oscillatory shear (LAOS) deformations unraveled the localization of strain and stress when the materials were deformed. In crumpled materials the tuning of friction, training, internal morphology, and plasticity can be used to program the response by altering the interplay between structural parts. For macroscopically entangled quasi-1D filaments, changing the chain length allows for the creation of entanglements to distribute the stress to larger areas of the sample, avoiding a pronounced localized yielding.

When studying the arranged counterparts, we demonstrated that combining the study of shear and shear-induced normal stresses allows for a more comprehensive mechanical characterization of the samples. In both meat whole cuts and origami shells, studying only deformations under shear in the linear regime would miss the rich behavior that these different samples can exhibit, traced back to their architectural elements.

The studies in this thesis unveil new possibilities for controlling the interplay between stress-bearing elements in macroscale model systems. The insights gained from our study can potentially contribute to the development of new materials and structures with tunable mechanical properties for various applications. Furthermore, these insights can inform our understanding of the fundamental principles that govern the behavior of different systems under stress.

References

1. Born, M. & Huang, K. *Dynamical theory of crystal lattices* (Clarendon Press ; Oxford University Press, Oxford : New York, 1988).
2. Whitesides, G. M. & Grzybowski, B. Self-Assembly at All Scales. *Science* **295,** 2418–2421 (2002).
3. Bertoldi, K., Vitelli, V., Christensen, J. & van Hecke, M. Flexible mechanical metamaterials. *Nature Reviews Materials* **2,** 17066 (2017).
4. Kadic, M., Milton, G. W., van Hecke, M. & Wegener, M. 3D metamaterials. *Nature Reviews Physics* **1.** Publisher: Springer Nature, 198–210 (2019).
5. Berthier, L. & Biroli, G. Theoretical perspective on the glass transition and amorphous materials. *Reviews of Modern Physics* **83.** arXiv: 1011.2578, 587–645 (2011).
6. Doi, M. & Edwards, S. F. *The theory of polymer dynamcis* (Oxford University Press, 1988).
7. Charbonneau, P., Kurchan, J., Parisi, G., Urbani, P. & Zamponi, F. Glass and Jamming Transitions: From Exact Results to Finite-Dimensional Descriptions. *Annual Review of Condensed Matter Physics* **8,** 265–288 (2017).
8. Berthier, L. Dynamic Heterogeneity in Amorphous Materials. *Physics* **4,** 42 (2011).
9. Falk, M. L. & Langer, J. Deformation and Failure of Amorphous, Solidlike Materials. *Annual Review of Condensed Matter Physics* **2,** 353–373 (2011).

10. Nicolas, A., Ferrero, E. E., Martens, K. & Barrat, J. L. Deformation and flow of amorphous solids: Insights from elastoplastic models. *Reviews of Modern Physics* **90.** Publisher: American Physical Society, 45006 (2018).
11. Albuquerque, R. & Gomes, M. Stress relaxation in crumpled surfaces. *Physica A: Statistical Mechanics and its Applications* **310,** 377–383 (2002).
12. Liu, A. J. & Nagel, S. R. The Jamming Transition and the Marginally Jammed Solid. *Annual Review of Condensed Matter Physics* **1,** 347–369 (2010).
13. Matan, K., Williams, R. B., Witten, T. A. & Nagel, S. R. Crumpling a Thin Sheet. *Physical Review Letters* **88,** 076101 (2002).
14. De Gennes, P. G. & De Genes, P. Reptation of a Polymer Chain in the Presence of Fixed Obstacles. *The Journal of Chemical Physics* **55,** 572–579 (1971).
15. De Gennes, P. G. & Witten, T. A. Scaling Concepts in Polymer Physics. *Physics Today* **33,** 51–54 (1980).
16. Doi, M. & Edwards, S. F. Dynamics of concentrated polymer systems. Part 2.—Molecular motion under flow. *J. Chem. Soc., Faraday Trans. 2* **74,** 1802–1817 (1978).
17. Kramers, H. Het gedrag van macromoleculen in een stroomende vloeistof. *Physica* **11,** 1–19 (1944).
18. Ben-Naim, E., Daya, Z. A., Vorobieff, P. & Ecke, R. E. Knots and Random Walks in Vibrated Granular Chains. *Physical Review Letters* **86,** 1414–1417 (2001).
19. Hastings, M. B., Daya, Z. A., Ben-Naim, E. & Ecke, R. E. Entropic tightening of vibrated chains. *Physical Review E* **66,** 025102 (2002).
20. Daya, Z. A., Ben-Naim, E. & Ecke, R. E. Experimental characterization of vibrated granular rings. *European Physical Journal E* **21,** 1–10 (2006).
21. Zou, L. N., Cheng, X., Rivers, M. L., Jaeger, H. M. & Nagel, S. R. The packing of granular polymer chains. *Science* **326,** 408–410 (2009).
22. Regev, I. & Reichhardt, C. Rheology and shear band suppression in particle and chain mixtures. **87,** 020201 (2013).
23. Soh, B. W., Gengaro, I. R., Klotz, A. R. & Doyle, P. S. Self-entanglement of a tumbled circular chain. *Physical Review Research* **1.** Publisher: American Physical Society (APS), 033194 (2019).

24. Laso, M., Karayiannis, N. C., Foteinopoulou, K., Mansfield, M. L. & Kröger, M. Random packing of model polymers: Local structure, topological hindrance and universal scaling. *Soft Matter* **5,** 1762–1770 (2009).

25. Samadi Taheri, F., Fazli, H., Doi, M. & Habibi, M. Granular chain escape from a pore in a wall in the presence of particles on one side: a comparison to polymer translocation. *Soft Matter* **14.** Publisher: Royal Society of Chemistry, 5420–5427 (2018).

26. Mortazavi, F., Habibi, M. & Nedaaee Oskoee, E. Translocation of a granular chain in a horizontally vibrated saw-tooth channel. *European Physical Journal E* **39.** Publisher: Springer New York LLC, 93 (2016).

27. Sun, Y.-C. C. *et al.* Short granular chain under vibration: Spontaneous switching of states. *Physical Review E* **93.** Publisher: American Physical Society, 032902 (2016).

28. Wen, P. *et al.* Bottom stresses of static packing of granular chains. *Physica A: Statistical Mechanics and its Applications* **419.** Publisher: Elsevier B.V., 457–463 (2015).

29. Yuan, X., Zheng, N., Shi, Q., Sun, G. & Li, L. Segregation in mixtures of granular chains and spherical grains under vertical vibration. *Physical Review E* **87,** 042203 (2013).

30. Prentis, J. J. & Sisan, D. R. Granular polymer solution. *Physical Review E - Statistical Physics, Plasmas, Fluids, and Related Interdisciplinary Topics* **65,** 3–6 (2002).

31. Dumont, D. *et al.* Emergent Strain Stiffening in Interlocked Granular Chains. *Physical Review Letters* **120.** arXiv: 1707.08547 Publisher: American Physical Society, 088001 (2018).

32. Safford, K., Kantor, Y., Kardar, M. & Kudrolli, A. Structure and dynamics of vibrated granular chains: Comparison to equilibrium polymers. *Physical Review E - Statistical, Nonlinear, and Soft Matter Physics* **79,** 061304 (2009).

33. Lopatina, L. M., Olson Reichhardt, C. J. & Reichhardt, C. Jamming in granular polymers. *Physical Review E* **84.** arXiv: 0912.1874, 011303 (2011).

34. Jeng, P.-R. R. *et al.* Collapse kinetics of vibrated granular chains. *Journal of Chemical Physics* **135,** 244903 (2011).

35. Brown, E., Nasto, A., Athanassiadis, A. G. & Jaeger, H. M. Strain Stiffening in Random Packings of Entangled Granular Chains. *Physical Review Letters* **108,** 108302 (2012).
36. Ulrich, X., Fried, E. & Shen, A. Q. Crossover transition in flowing granular chains. *Physical Review E - Statistical, Nonlinear, and Soft Matter Physics* **80,** 030301 (2009).
37. Yadav, V. & Kudrolli, A. Diffusion of granular rods on a rough vibrated substrate. *The European Physical Journal E* **35,** 104 (2012).
38. Reichhardt, C. J. O. & Lopatina, L. M. A Ball-and-Chain Polymer Model. *Science* **326,** 374–375 (2009).
39. Mohaddespour, A. & Hill, R. J. Granular polymer composites. *Soft Matter* **8,** 12060–12065 (2012).
40. Mohaddespour, A. & Hill, R. J. Granular sphere-chain relaxation dynamics to interpret polymer-nanocomposite glass transition temperatures. *Granular Matter* **20.** Publisher: Springer Berlin Heidelberg, 1–11 (2018).
41. Bailey, A. J. The basis of meat texture. *Journal of the Science of Food and Agriculture* **23,** 995–1007 (1972).
42. Purslow, P. P. Muscle fascia and force transmission. *Journal of Bodywork and Movement Therapies* **14,** 411–417 (2010).
43. Pette, D. & Staron, R. S. in *Reviews of Physiology, Biochemistry and Pharmacology, Volume 94* 1–76 (Springer Berlin Heidelberg, Berlin, Heidelberg, 1990).
44. Schreuders, F. K., Schlangen, M., Kyriakopoulou, K., Boom, R. M. & van der Goot, A. J. Texture methods for evaluating meat and meat analogue structures: A review. *Food Control* **127.** Publisher: Elsevier Ltd, 108103 (2021).
45. Voisey, P. W. & Larmond, E. Examination of Factors Affecting Performance of the Warner-Bratzler Meat Shear Test. *Canadian Institute of Food Science and Technology Journal* **7,** 243–249 (1974).
46. Steffe, J. F. *Rheological Methods in Food Process Engineering* (Freeman press, 1996).
47. Melito, H. & Daubert, C. Rheological Innovations for Characterizing Food Material Properties. *Annual Review of Food Science and Technology* **2,** 153–179 (2012).

48. Melito, H., Daubert, C. & Foegeding, E. Relationships between Nonlinear Viscoelastic Behavior and Rheological, Sensory and Oral Processing Behavior of Commercial Cheese: Relationships between Behaviors of Cheese. *Journal of Texture Studies* **44,** 253–288 (2013).
49. Chen, J. Food oral processing—A review. *Food Hydrocolloids* **23,** 1–25 (2009).
50. Liu, Y., Cai, J. & Feng, J. Buckling suppression of a thin-walled Miura-origami patterned tube. *PLOS ONE* **17** (ed Wang, J.) e0270228 (2022).
51. Huang, C. *et al.* Bistable programmable origami based soft electricity generator with inter-well modulation. *Nano Energy* **103,** 107775 (2022).
52. Kuribayashi, K. *et al.* Self-deployable origami stent grafts as a biomedical application of Ni-rich TiNi shape memory alloy foil. *Materials Science and Engineering: A* **419,** 131–137 (2006).
53. Yoshimura, Y. *On the mechanism of buckling of a circular cylindrical shell under axial compression* tech. rep. Publication Title: Technical Memorandum 1390 (National Advisory Committee for Aeronautics (NACA), Washington, 1955).
54. Kresling, B. in *Origami^{3}* (ed Hull, T.) 199–208 (A K Peters/CRC Press, 2002).
55. Hunt, G. W. & Ario, I. Twist buckling and the foldable cylinder: An exercise in origami. *International Journal of Non-Linear Mechanics* **40,** 833–843 (2005).
56. Gottesman, O., Vouga, E., Rubinstein, S. M. & Mahadevan, L. Localized patterns in crushed conical shells. *Epl* **124,** 1–6 (2018).
57. Fokker, M. C., Janbaz, S. & Zadpoor, A. A. Crumpling of thin sheets as a basis for creating mechanical metamaterials. *RSC Advances* **9.** Publisher: Royal Society of Chemistry, 5174–5188 (2019).
58. Weiner, N., Bhosale, Y., Gazzola, M. & King, H. Mechanics of randomly packed filaments - The ”bird nest” as meta-material. *Journal of Applied Physics* **127.** Publisher: American Institute of Physics Inc. (2020).
59. Ewoldt, R. H., Johnston, M. T. & Caretta, L. M. in *Complex Fluids in Biological Systems* (ed Spagnolie, S. E.) 207–241 (Springer New York, New York, NY, 2015).
60. Barnes, H. A. *A Handbook Of Elementary Rheology* (Cambrian Printers, Aberyswyth, 2000).

61. Mezger, T. G. *The Rheology Handbook: 4th Edition* (Vincentz Network, 2019).

62. Hyun, K. *et al.* A review of nonlinear oscillatory shear tests: Analysis and application of large amplitude oscillatory shear (LAOS). *Progress in Polymer Science (Oxford)* **36.** Publisher: Elsevier Ltd, 1697–1753 (2011).

63. Ewoldt, R. H., Hosoi, A. E. & McKinley, G. H. New measures for characterizing nonlinear viscoelasticity in large amplitude oscillatory shear. *Journal of Rheology* **52.** Publisher: Society of Rheology, 1427–1458 (2008).

64. Payne, A. R. The dynamic properties of carbon black loaded natural rubber vulcanizates. Part II. *Journal of Applied Polymer Science* **6,** 368–372 (1962).

65. Giacomin, A. J. & Dealy, J. M. in *Techniques in Rheological Measurement* (ed Collyer, A. A.) 99–121 (Springer Netherlands, Dordrecht, 1993).

66. Dealy, J. M. & Wissbrun, K. F. *Melt Rheology and Its Role in Plastics Processing: Theory and Applications* (Springer Netherlands, Dordrecht, 1999).

67. Ewoldt, R. H., Winter, P., Maxey, J. & McKinley, G. H. Large amplitude oscillatory shear of pseudoplastic and elastoviscoplastic materials. *Rheologica Acta* **49,** 191–212 (2010).

68. Ganeriwala, S. N. & Rotz, C. A. Fourier transform mechanical analysis for determining the nonlinear viscoelastic properties of polymers. *Polymer Engineering and Science* **27,** 165–178 (1987).

69. Poynting, J. On pressure perpendicular to the shear planes in finite pure shears and on the lengthening of loaded wires when twisted. *Proceedings of the Royal Society A: Mathematical, Physical and Engineering Sciences* **82,** 546–559 (1909).

70. Rivlin, R. S. & Saunders, D. Large elastic deformations of isotropic materials VII. Experiments on the deformation of rubber. *Philosophical Transactions of the Royal Society of London. Series A, Mathematical and Physical Sciences* **243,** 251–288 (1951).

71. Macosko, C. *Rheology: Principles, Measurements, and Applications* (Wiley, 1994).

72. Ghorbani, A. *et al.* Inverted and Programmable Poynting Effects in Metamaterials. *Advanced Science* **8.** arXiv: 2102.10904 Publisher: John Wiley and Sons Inc, 1–9 (2021).

73. Janmey, P. A. *et al.* Negative normal stress in semiflexible biopolymer gels. *Nature Materials* **6,** 48–51 (2007).

74. Fan, J. *et al.* A review of additive manufacturing of metamaterials and developing trends. *Materials Today* **50.** Publisher: Elsevier B.V., 303–328 (2021).

75. Kolpakov, A. G. Determination of the average characteristics of elastic frameworks. *Journal of Applied Mathematics and Mechanics* **49,** 739–745 (1985).

76. Roderic, L. Foam Structures with a Negative Poisson's Ratio. *Science* **235.** Publisher: American Association for the Advancement of Science, 1038–1040 (1987).

77. Qin, R., Zheng, J. & Zhu, W. Sign-tunable Poisson's ratio in semi-fluorinated graphene. *Nanoscale* **9.** Publisher: The Royal Society of Chemistry, 128–133 (2017).

78. Ding, Y., Liu, Z., Qiu, C. & Shi, J. Metamaterial with Simultaneously Negative Bulk Modulus and Mass Density. *Physical Review Letters* **99.** Publisher: American Physical Society, 93904 (2007).

79. Mirzaali, M. J., Pahlavani, H. & Zadpoor, A. A. Auxeticity and stiffness of random networks: Lessons for the rational design of 3D printed mechanical metamaterials. *Applied Physics Letters* **115.** Publisher: AIP Publishing LLC, 3–8 (2019).

80. Aste, T., Saadatfar, M. & Senden, T. Geometrical structure of disordered sphere packings. *Physical Review E* **71.** arXiv: cond-mat/0502016, 061302 (2005).

81. Scheffold, F., Cardinaux, F. & Mason, T. G. Linear and nonlinear rheology of dense emulsions across the glass and the jamming regimes. *Journal of Physics: Condensed Matter* **25.** arXiv: 1305.5182, 502101 (2013).

82. Sultan, E. & Boudaoud, A. Statistics of Crumpled Paper. *Physical Review Letters* **96,** 136103 (2006).

83. Keim, N. A Crumpled Sheet's Remembrance of Things Past. *Physics* **10,** 18 (2017).

84. Ren, X., Das, R., Tran, P., Ngo, T. D. & Xie, Y. M. Auxetic metamaterials and structures: A review. *Smart Materials and Structures* **27.** Publisher: IOP Publishing (2018).

85. Lakes, R. Advances in negative Poisson's ratio materials. *Advanced Materials* **5.** Publisher: John Wiley & Sons, Ltd, 293–296 (1993).

86. Bertoldi, K., Reis, P. M., Willshaw, S. & Mullin, T. Negative Poisson's Ratio Behavior Induced by an Elastic Instability. *Advanced Materials* **22.** Publisher: John Wiley & Sons, Ltd, 361–366 (2010).

87. Greaves, G. N., Greer, A. L., Lakes, R. S. & Rouxel, T. Poisson's ratio and modern materials. *Nature Materials* **10,** 823–837 (2011).

88. Carneiro, V. H., Meireles, J. & Puga, H. Auxetic materials — A review. *Materials Science-Poland* **31,** 561–571 (2013).

89. Kolken, H. M. A. & Zadpoor, A. A. Auxetic mechanical metamaterials. *RSC Advances* **7.** Publisher: The Royal Society of Chemistry, 5111–5129 (2017).

90. Kelkar, P. U. *et al.* Cellular auxetic structures for mechanical metamaterials: A review. *Sensors (Switzerland)* **20.** Publisher: MDPI AG (2020).

91. Wang, Z. *et al.* Progress in Auxetic Mechanical Metamaterials: Structures, Characteristics, Manufacturing Methods, and Applications. *Advanced Engineering Materials* **22.** Publisher: Wiley-VCH Verlag (2020).

92. Evans, K. E., Nkansah, M. A., Hutchinson, I. J. & Rogers, S. C. Molecular network design. *Nature* **353,** 124–124 (1991).

93. Li, D., Yin, J., Dong, L. & Lakes, R. S. Strong re-entrant cellular structures with negative Poisson's ratio. *Journal of Materials Science* **53,** 3493–3499 (2018).

94. Prall, D. & Lakes, R. S. Properties of a chiral honeycomb with a poisson's ratio of — 1. *International Journal of Mechanical Sciences* **39,** 305–314 (1997).

95. Sanami, M., Ravirala, N., Alderson, K. & Alderson, A. Auxetic Materials for Sports Applications. *Procedia Engineering* **72,** 453–458 (2014).

96. Mirzaali, M. J. *et al.* Rational design of soft mechanical metamaterials: Independent tailoring of elastic properties with randomness. *Applied Physics Letters* **111.** Publisher: American Institute of Physics, 51903 (2017).

97. Mirzaali, M. J. *et al.* Curvature Induced by Deflection in Thick Meta-Plates. *Advanced Materials* **33.** Publisher: John Wiley and Sons Inc (2021).

98. Wu, W. *et al.* Mechanical design and multifunctional applications of chiral mechanical metamaterials: A review. *Materials & Design* **180,** 107950 (2019).
99. Grima, J. N., Gatt, R. & Farrugia, P.-S. On the properties of auxetic meta-tetrachiral structures. *physica status solidi (b)* **245.** Publisher: John Wiley & Sons, Ltd, 511–520 (2008).
100. Chan, N. & Evans, K. E. Indentation Resilience of Conventional and Auxetic Foams. *Journal of Cellular Plastics* **34.** Publisher: SAGE Publications Ltd STM, 231–260 (1998).
101. Silverberg, J. L. *et al. Using origami design principles to fold reprogrammable mechanical metamaterials* Publication Title: Science Issue: 6197 ISSN: 0036-8075. 2014.
102. Yasuda, H. & Yang, J. Reentrant origami-based metamaterials with negative Poisson's ratio and bistability. *Physical Review Letters* **114.** Publisher: American Physical Society (2015).
103. Overvelde, J. T. *et al.* A three-dimensional actuated origami-inspired transformable metamaterial with multiple degrees of freedom. *Nature Communications* **7.** Publisher: Nature Publishing Group (2016).
104. Zhou, X., Zang, S. & You, Z. *Origami mechanical metamaterials based on the Miura-derivative fold patterns* in *Proceedings of the Royal Society A: Mathematical, Physical and Engineering Sciences* **472.** Issue: 2191 ISSN: 14712946 (Royal Society of London, 2016), 20160361.
105. Johnson, M. *et al.* Fabricating biomedical origami: a state-of-the-art review. *International Journal of Computer Assisted Radiology and Surgery* **12.** Publisher: Springer Verlag, 2023–2032 (2017).
106. Morris, E., McAdams, D. A. & Malak, R. The state of the art of origami-inspired products: A review. *Proceedings of the ASME Design Engineering Technical Conference* **5B-2016.** ISBN: 9780791850169, 1–14 (2016).
107. McPherson, B. N. & Kauffman, J. L. Dynamics and estimation of origami-inspired deployable space structures: A review. *AIAA Scitech 2019 Forum.* Publisher: American Institute of Aeronautics and Astronautics Place: Reston, Virginia ISBN: 9781624105784, 1–18 (2019).
108. Santangelo, C. D. Extreme mechanics: Self-folding origami. *Annual Review of Condensed Matter Physics* **8,** 165–183 (2017).

109. Wang, P., Meyer, T. A., Pan, V., Dutta, P. K. & Ke, Y. The Beauty and Utility of DNA Origami. *Chem* **2.** Publisher: Elsevier Inc., 359–382 (2017).

110. Lang, R. J., Tolman, K. A., Crampton, E. B., Magleby, S. P. & Howell, L. L. A Review of Thickness-Accommodation Techniques in Origami-Inspired Engineering. *Applied Mechanics Reviews* **70,** 1–20 (2018).

111. Wu, S. R., Chen, T. H. & Tsai, H. Y. A Review of Actuation Force in Origami Applications. *Journal of Mechanics* **35,** 627–639 (2019).

112. Bila, H., Kurisinkal, E. E. & Bastings, M. M. Engineering a stable future for DNA-origami as a biomaterial. *Biomaterials Science* **7.** Publisher: Royal Society of Chemistry, 532–541 (2019).

113. Fei, L. J. & Sujan, D. Origami Theory and its Applications: A. *Computer Science, Engineering* **7.** ISBN: 0060128535426, 1131–1135 (2013).

114. Chu, C. C. & Keong, C. K. The review on tessellation origami inspired folded structure. *AIP Conference Proceedings* **1892.** ISBN: 9780735415744 (2017).

115. Peraza-Hernandez, E. A., Hartl, D. J., Malak, R. J. & Lagoudas, D. C. Origami-inspired active structures: A synthesis and review. *Smart Materials and Structures* **23.** Publisher: IOP Publishing (2014).

116. Rus, D. & Tolley, M. T. Design, fabrication and control of origami robots. *Nature Reviews Materials* **3.** Publisher: Nature Publishing Group, 101–112 (2018).

117. Thrall, A. P. & Quaglia, C. P. Accordion shelters: A historical review of origami-like deployable shelters developed by the US military. *Engineering Structures* **59.** Publisher: Elsevier Ltd ISBN: 5746312533, 686–692 (2014).

118. Meloni, M. *et al.* Engineering Origami: A Comprehensive Review of Recent Applications, Design Methods, and Tools. *Advanced Science* **8.** Publisher: John Wiley and Sons Inc (2021).

119. Dey, S. *et al.* DNA origami. *Nature Reviews Methods Primers* **1.** Publisher: Springer Nature (2021).

120. Ji, J. C., Luo, Q. & Ye, K. Vibration control based metamaterials and origami structures: A state-of-the-art review. *Mechanical Systems and Signal Processing* **161.** Publisher: Academic Press (2021).

121. Callens, S. J. & Zadpoor, A. A. From flat sheets to curved geometries: Origami and kirigami approaches. *Materials Today* **21.** Publisher: Elsevier B.V., 241–264 (2018).

122. Xiang, X. M., Lu, G. & You, Z. Energy absorption of origami inspired structures and materials. *Thin-Walled Structures* **157.** Publisher: Elsevier Ltd (2020).

123. Zhai, Z., Wu, L. & Jiang, H. Mechanical metamaterials based on origami and kirigami. *Applied Physics Reviews* **8,** 041319 (2021).

124. Park, J. J., Won, P. & Ko, S. H. A Review on Hierarchical Origami and Kirigami Structure for Engineering Applications. *International Journal of Precision Engineering and Manufacturing - Green Technology* **6.** Publisher: Korean Society for Precision Engineering, 147–161 (2019).

125. Turner, N., Goodwine, B. & Sen, M. A review of origami applications in mechanical engineering. *Proceedings of the Institution of Mechanical Engineers, Part C: Journal of Mechanical Engineering Science* **230,** 2345–2362 (2016).

126. Bell, N. A. & Keyser, U. F. Nanopores formed by DNA origami: A review. *FEBS Letters* **588.** Publisher: Federation of European Biochemical Societies, 3564–3570 (2014).

127. Lebée, A. From folds to structures, a review. *International Journal of Space Structures* **30,** 55–74 (2015).

128. Zhou, C., Wang, B., Ma, J. & You, Z. Dynamic axial crushing of origami crash boxes. *International Journal of Mechanical Sciences* **118.** Publisher: Elsevier, 1–12 (2016).

129. Wang, B. & Zhou, C. The imperfection-sensitivity of origami crash boxes. *International Journal of Mechanical Sciences* **121.** Publisher: Elsevier, 58–66 (2017).

130. Liu, K., Novelino, L. S., Gardoni, P. & Paulino, G. H. Big influence of small random imperfections in origami-based metamaterials. *Proceedings of the Royal Society A: Mathematical, Physical and Engineering Sciences* **476,** 20200236 (2020).

131. Liu, W., Wang, N., Huang, J. & Zhong, H. The effect of irregularity, residual convex units and stresses on the effective mechanical properties of 2D auxetic cellular structure. *Materials Science and Engineering: A* **609,** 26–33 (2014).

132. Mizzi, L. *et al.* Influence of translational disorder on the mechanical properties of hexachiral honeycomb systems. *Composites Part B: Engineering* **80,** 84–91 (2015).

133. Sigmund, O., Torquato, S. & Aksay, I. A. On the design of 1–3 piezocomposites using topology optimization. *Journal of Materials Research* **13,** 1038–1048 (1998).

134. Pozniak, A. A. & Wojciechowski, K. W. Poisson's ratio of rectangular anti-chiral structures with size dispersion of circular nodes. *physica status solidi (b)* **251.** Publisher: John Wiley & Sons, Ltd, 367–374 (2014).

135. Ellenbroek, W. G., Hagh, V. F., Kumar, A., Thorpe, M. F. & van Hecke, M. Rigidity Loss in Disordered Systems: Three Scenarios. *Physical Review Letters* **114.** Publisher: American Physical Society, 135501 (2015).

136. Liu, W., Wang, N., Luo, T. & Lin, Z. In-plane dynamic crushing of reentrant auxetic cellular structure. *Materials & Design* **100,** 84–91 (2016).

137. Meeussen, A. S., Oğuz, E. C., Shokef, Y. & Hecke, M. v. Topological defects produce exotic mechanics in complex metamaterials. *Nature Physics* **16,** 307–311 (2020).

138. Reid, D. R. *et al.* Auxetic metamaterials from disordered networks. *Proceedings of the National Academy of Sciences* **115,** E1384 LP –E1390 (2018).

139. Goodrich, C. P., Liu, A. J. & Nagel, S. R. The Principle of Independent Bond-Level Response: Tuning by Pruning to Exploit Disorder for Global Behavior. *Physical Review Letters* **114.** Publisher: American Physical Society, 225501 (2015).

140. Hexner, D., Liu, A. J. & Nagel, S. R. Role of local response in manipulating the elastic properties of disordered solids by bond removal. *Soft Matter* **14.** Publisher: The Royal Society of Chemistry, 312–318 (2018).

141. Rocks, J. W. *et al.* Designing allostery-inspired response in mechanical networks. *Proceedings of the National Academy of Sciences* **114,** 2520 LP –2525 (2017).

142. Mullin, T., Deschanel, S., Bertoldi, K. & Boyce, M. C. Pattern Transformation Triggered by Deformation. *Physical Review Letters* **99.** Publisher: American Physical Society, 84301 (2007).

143. Caddock, B. D. & Evans, K. E. Microporous materials with negative Poisson's ratios. I. Microstructure and mechanical properties. *Journal of Physics D: Applied Physics* **22.** Publisher: IOP Publishing, 1877–1882 (1989).

144. Grima, J. N., Mizzi, L., Azzopardi, K. M. & Gatt, R. Auxetic Perforated Mechanical Metamaterials with Randomly Oriented Cuts. *Advanced Materials* **28.** Publisher: John Wiley & Sons, Ltd, 385–389 (2016).

145. Chaudhary, G., Niu, L., Lewicka, M., Han, Q. & Mahadevan, L. *Geometric mechanics of random kirigami* arXiv: 2112.13699. 2021.

146. Purohit, P. K., Kondev, J. & Phillips, R. Mechanics of DNA packaging in viruses. *Proceedings of the National Academy of Sciences* **100,** 3173–3178 (2003).

147. Honig, B. Protein folding: from the levinthal paradox to structure prediction. *Journal of Molecular Biology* **293,** 283–293 (1999).

148. Finkelstein, A. & Galzitskaya, O. Physics of protein folding. *Physics of Life Reviews* **1,** 23–56 (2004).

149. Deng, S. & Berry, V. Wrinkled, rippled and crumpled graphene: an overview of formation mechanism, electronic properties, and applications. *Materials Today* **19.** Publisher: Elsevier Ltd., 197–212 (2016).

150. Liao, Y., Li, Z., Fatima & Xia, W. Size-dependent structural behaviors of crumpled graphene sheets. *Carbon* **174.** Publisher: Elsevier Ltd, 148–157 (2021).

151. Plumb, K. Structure and tectonic style of the Precambrian shields and platforms of northern Australia. *Tectonophysics* **58,** 291–325 (1979).

152. Miller, M., Kennett, B. & Gorbatov, A. Morphology of the distorted subducted Pacific slab beneath the Hokkaido corner, Japan. *Physics of the Earth and Planetary Interiors* **156,** 1–11 (2006).

153. Balankin, A. S., Ochoa, D. S., Miguel, I. A., Ortiz, J. P. & Cruz, M. A. M. Fractal topology of hand-crumpled paper. *Physical Review E* **81,** 061126 (2010).

154. Cottrino, S., Viviès, P., Fabrègue, D. & Maire, E. Mechanical properties of crumpled aluminum foils. *Acta Materialia* **81,** 98–110 (2014).

155. Mota, B. & Herculano-Houzel, S. Cortical folding scales universally with surface area and thickness, not number of neurons. *Science* **349,** 74–77 (2015).

R

156. Wood, D. P. Safety and the car size effect: A fundamental explanation. *Accident Analysis & Prevention* **29,** 139–151 (1997).
157. Fu, H., Huang, J. & Gray, K. Crumpled graphene balls adsorb micropollutants from water selectively and rapidly. *Carbon* **183.** Publisher: Elsevier Ltd, 958–969 (2021).
158. Gomes, M. A. F. Paper crushes fractally. *Journal of Physics A: General Physics* **20,** 5–7 (1987).
159. Gomes, M. A. F. Fractal geometry in crumpled paper balls. *American Journal of Physics* **55,** 649–650 (1987).
160. Gomes, M. A., Jyh, T. I., Ren, T. I., Rodrigues, I. M. & Furtado, C. B. Mechanically deformed crumpled surfaces. *Journal of Physics D: Applied Physics* **22,** 1217–1221 (1989).
161. Gomes, M. A. & Oliveira, V. M. Repacking of crumpled systems. *Philosophical Magazine Letters* **78,** 325–329 (1998).
162. Balankin, A. S. *et al.* Intrinsically anomalous roughness of randomly crumpled thin sheets. *Physical Review E* **74,** 061602 (2006).
163. Balankin, A. S., Silva, I. C., Martínez, O. A. & Huerta, O. S. Scaling properties of randomly folded plastic sheets. *Physical Review E - Statistical, Nonlinear, and Soft Matter Physics* **75,** 1–3 (2007).
164. Balankin, A. S., de Oca, R. C. M. & Ochoa, D. S. Intrinsically anomalous self-similarity of randomly folded matter. *Physical Review E* **76,** 032101 (2007).
165. Bouaziz, O., Masse, J., Allain, S., Orgéas, L. & Latil, P. Compression of crumpled aluminum thin foils and comparison with other cellular materials. *Materials Science and Engineering: A* **570,** 1–7 (2013).
166. Martoïa, F. *et al.* Crumpled paper sheets: Low-cost biobased cellular materials for structural applications. *Materials and Design* **136.** Publisher: Elsevier Ltd, 150–164 (2017).
167. Croll, A. B., Twohig, T. & Elder, T. The compressive strength of crumpled matter. *Nature Communications* **10.** Publisher: Springer US, 1502 (2019).
168. Deboeuf, S., Katzav, E., Boudaoud, A., Bonn, D. & Adda-Bedia, M. Comparative Study of Crumpling and Folding of Thin Sheets. *Physical Review Letters* **110,** 104301 (2013).

R

169. Ben Amar, M. & Pomeau, Y. Crumpled paper. *Proceedings of the Royal Society of London. Series A: Mathematical, Physical and Engineering Sciences* **453,** 729–755 (1997).

170. Balankin, A. S. *et al.* Mechanical properties and relaxation behavior of crumpled aluminum foils. *Journal of Materials Science* **50,** 4749–4761 (2015).

171. Shaebani, M. R., Najafi, J., Farnudi, A., Bonn, D. & Habibi, M. Compaction of quasi-one-dimensional elastoplastic materials. *Nature Communications* **8.** Publisher: Nature Publishing Group, 15568 (2017).

172. Wood, A. J. Witten's lectures on crumpling. *Physica A: Statistical Mechanics and its Applications* **313,** 83–109 (2002).

173. Giménez-Ribes, G., van der Linden, E. & Habibi, M. Auxetic behavior and unusual shear resistance of crumpled materials: Opportunities for programming the nonlinear responses of crumpled mechanical metamaterials. *Materials & Design* **223,** 111258 (2022).

174. Ikeda, A., Berthier, L. & Sollich, P. Unified study of glass and jamming rheology in soft particle systems. *Physical Review Letters* **109,** 018301 (2012).

175. Ko, R. H. & Bean, C. P. A simple experiment that demonstrates fractal behavior. *The Physics Teacher* **29,** 78–79 (1991).

176. Kantor, Y., Kardar, M. & Nelson, D. R. Statistical mechanics of tethered surfaces. *Physical Review Letters* **57,** 791–794 (1986).

177. Kramer, E. M. & Lobkovsky, A. E. Universal power law in the noise from a crumpled elastic sheet. *Physical Review E - Statistical Physics, Plasmas, Fluids, and Related Interdisciplinary Topics* **53,** 1465–1469 (1996).

178. Kohlrausch, R. Theorie des elektrischen Rückstandes in der Leidener Flasche. *Annalen der Physik und Chemie* **167,** 179–214 (1854).

179. Williams, G. & Watts, D. C. Non-symmetrical dielectric relaxation behaviour arising from a simple empirical decay function. *Transactions of the Faraday Society* **66,** 80 (1970).

180. Weibull, W. A Statistical Distribution Function of Wide Applicability. *Journal of Applied Mechanics* **18,** 293–297 (1951).

181. Palmer, R. G., Stein, D. L., Abrahams, E. & Anderson, P. W. Models of Hierarchically Constrained Dynamics for Glassy Relaxation. *Physical Review Letters* **53,** 958–961 (1984).

182. Phillips, J. C. Stretched exponential relaxation in molecular and electronic gases. *Reports on Progress in Physics* **59,** 1133–1207 (1996).

183. Krall, A. H. & Weitz, D. A. Internal dynamics and elasticity of fractal colloidal gels. *Physical Review Letters* **80,** 778–781 (1998).

184. Sagis, L. M. C. *et al.* Dynamic heterogeneity in complex interfaces of soft interface-dominated materials. *Scientific Reports* **9,** 2938 (2019).

185. Liao, Y., Li, Z., Chen, L., Croll, A. B. & Xia, W. Crumpling Defective Graphene Sheets. *Nano Letters,* acs.nanolett.2c04771 (2023).

186. Mota, K. P. & de Oliveira, P. M. C. Monte Carlo simulations for the slow relaxation of crumpled surfaces. *Physica A: Statistical Mechanics and its Applications* **387.** arXiv: 0810.3955, 6095–6104 (2008).

187. Tallinen, T., Aström, J. A. & Timonen, J. Deterministic folding in stiff elastic membranes. *Physical Review Letters* **101,** 1–4 (2008).

188. Tallinen, T., Åström, J. A. & Timonen, J. Discrete element simulations of crumpling of thin sheets. *Computer Physics Communications* **180.** Publisher: Elsevier B.V., 512–516 (2009).

189. Tallinen, T., Åström, J. A. & Timonen, J. The effect of plasticity in crumpling of thin sheets. *Nature Materials* **8.** Publisher: Nature Publishing Group, 25–29 (2009).

190. Aharoni, H. & Sharon, E. Direct observation of the temporal and spatial dynamics during crumpling. *Nature Materials* **9.** Publisher: Nature Publishing Group, 993–997 (2010).

191. Susarrey Huerta, O., Mendoza Nuñez, M., Tamayo Meza, P. A. & Balankin, A. S. Mechanics of Randomly Folded Thin Materials. *Advanced Materials Research* **65,** 33–38 (2009).

192. Balankin, A. S., Susarrey Huerta, O. & Tapia, V. Statistics of energy dissipation and stress relaxation in a crumpling network of randomly folded aluminum foils. *Physical Review E - Statistical, Nonlinear, and Soft Matter Physics* **88,** 1–7 (2013).

193. Lin, Y. C., Wang, Y. L., Liu, Y. & Hong, T. M. Crumpling under an Ambient Pressure. *Physical Review Letters* **101,** 125504 (2008).

194. Dierking, I. & Archer, P. Sudden ridge collapse in the stress relaxation of thin crumpled polymer films. *Physical Review E - Statistical, Nonlinear, and Soft Matter Physics* **77,** 1–5 (2008).

195. Thiria, B. & Adda-Bedia, M. Relaxation mechanisms in the unfolding of thin sheets. *Physical Review Letters* **107,** 1–4 (2011).

196. Balankin, A. S., Susarrey Huerta, O., Hernández Méndez, F. & Patiño Ortiz, J. Slow dynamics of stress and strain relaxation in randomly crumpled elasto-plastic sheets. *Physical Review E* **84,** 021118 (2011).

197. Phillips, P. XLIX. The slow stretch in indiarubber, glass, and metal wires when subjected to a constant pull. *The London, Edinburgh, and Dublin Philosophical Magazine and Journal of Science* **9,** 513–531 (1905).

198. Olds, G. C. Mechanisms of creep in a precipitation hardened alloy. *Proceedings of the Physical Society. Section B* **67,** 832–842 (1954).

199. Wyatt, O. H. Transient Creep in Pure Metals. *Proceedings of the Physical Society. Section B* **66,** 459–480 (1953).

200. Nguyen, V. B., Darnige, T., Bruand, A. & Clement, E. Creep and Fluidity of a Real Granular Packing near Jamming. *Physical Review Letters* **107,** 138303 (2011).

201. Siebenbürger, M., Ballauff, M. & Voigtmann, T. Creep in Colloidal Glasses. *Physical Review Letters* **108,** 255701 (2012).

202. Ballesta, P. & Petekidis, G. Creep and aging of hard-sphere glasses under constant stress. *Physical Review E* **93,** 1–10 (2016).

203. Bouttes, D. & Vandembroucq, D. Creep of amorphous materials: A mesoscopic model. *AIP Conference Proceedings* **1518,** 481–486 (2013).

204. Cottrell, A. The time laws of creep. *Journal of the Mechanics and Physics of Solids* **1,** 53–63 (1952).

205. Nabarro, F. R. The time constant of logarithmic creep and relaxation. *Materials Science and Engineering A* **309-310,** 227–228 (2001).

206. Buckle, V. A. & Feltham, P. Logarithmic Creep of Copper and Aluminium. *Metal Science* **9,** 541–546 (1975).

207. Rosti, J., Koivisto, J., Laurson, L. & Alava, M. J. Fluctuations and Scaling in Creep Deformation. *Physical Review Letters* **105,** 100601 (2010).

208. Zaiser, M. & Moretti, P. Fluctuation phenomena in crystal plasticity - A continuum model. *Journal of Statistical Mechanics: Theory and Experiment* **08004,** 79–97 (2005).

209. Lindley, D. *Focus: Paper Stretches Unevenly* 2010.

210. Lahini, Y., Gottesman, O., Amir, A. & Rubinstein, S. M. Nonmonotonic Aging and Memory Retention in Disordered Mechanical Systems. *Physical Review Letters* **118,** 085501 (2017).

211. Kovacs, A. J. Transition vitreuse dans les polymères amorphes. Etude phénoménologique. *Fortschritte der Hochpolymeren-Forschung* **3,** 394–507 (1964).

212. Amir, A., Oreg, Y. & Imry, Y. On relaxations and aging of various glasses. *Proceedings of the National Academy of Sciences of the United States of America* **109.** arXiv: 1112.3371, 1850–1855 (2012).

213. Shohat, D., Hexner, D. & Lahini, Y. Memory from coupled instabilities in unfolded crumpled sheets. *Proceedings of the National Academy of Sciences* **119** (2022).

214. Bense, H. & van Hecke, M. Complex pathways and memory in compressed corrugated sheets. *Proceedings of the National Academy of Sciences* **118,** e2111436118 (2021).

215. Van Bruggen, E., van der Linden, E. & Habibi, M. Tailoring relaxation dynamics and mechanical memory of crumpled materials by friction and ductility. *Soft Matter* **15,** 1633–1639 (2019).

216. Lechenault, F., Thiria, B. & Adda-Bedia, M. Mechanical Response of a Creased Sheet. *Physical Review Letters* **112,** 244301 (2014).

217. Farain, K. Relaxation Constant in the Folding of Thin Viscoelastic Sheets. *Physical Review Applied* **13,** 014031 (2020).

218. Jules, T., Lechenault, F. & Adda-Bedia, M. Plasticity and aging of folded elastic sheets. *Physical Review E* **102.** arXiv: 2004.11825 Publisher: American Physical Society, 1–9 (2020).

219. Shohat, D. & Lahini, Y. *Dissipation indicates memory formation in driven disordered systems* arXiv: 2209.00572. 2022.

220. Merrigan, C. *et al. Emergent Disorder and Mechanical Memory in Periodic Metamaterials* arXiv: 2204.04000. 2022.

221. Mungan, M. Putting memories on paper. *Proceedings of the National Academy of Sciences* **119.** Publisher: National Academy of Sciences (2022).

222. Kramer, E. M. & Witten, T. A. Stress Condensation in Crushed Elastic Manifolds. *Physical Review Letters* **78,** 1303–1306 (1997).

223. Lobkovsky, A., Gentges, S., Li, H., Morse, D. & Witten, T. A. Scaling Properties of Stretching Ridges in a Crumpled Elastic Sheet. *Science* **270,** 1482–1485 (1995).

224. Lobkovsky, A. E. & Witten, T. A. Properties of ridges in elastic membranes. *Physical Review E - Statistical Physics, Plasmas, Fluids, and Related Interdisciplinary Topics* **55,** 1577–1589 (1997).

225. DiDonna, B. A. & Witten, T. A. Anomalous strength of membranes with elastic ridges. *Physical Review Letters* **87.** arXiv: cond-mat/0104119, 206105–1–206105–4 (2001).

226. DiDonna, B. A., Witten, T. A., Venkataramani, S. C. & Kramer, E. M. Singularities, structures, and scaling in deformed m-dimensional elastic manifolds. *Physical Review E - Statistical Physics, Plasmas, Fluids, and Related Interdisciplinary Topics* **65,** 1–25 (2001).

227. Witten, T. A. Stress focusing in elastic sheets. *Reviews of Modern Physics* **79,** 643–675 (2007).

228. Seizilles, G., Bayart, E., Adda-Bedia, M. & Boudaoud, A. Bending waves in crumpled sheets. *Physical Review E* **84,** 065602 (2011).

229. Balankin, A. S. & Huerta, O. S. Entropic rigidity of a crumpling network in a randomly folded thin sheet. *Physical Review E* **77,** 051124 (2008).

230. Edwards, S. & Oakeshott, R. Theory of powders. *Physica A: Statistical Mechanics and its Applications* **157,** 1080–1090 (1989).

231. Edwards, S. F. & Grinev, D. V. Granular materials: Towards the statistical mechanics of jammed configurations. *Advances in Physics* **51,** 1669–1684 (2002).

232. Edwards, S. F., Grinev, D. V. & Brujić, J. Fundamental problems in statistical physics of jammed packings. *Physica A: Statistical Mechanics and its Applications* **330,** 61–76 (2003).

233. Edwards, S. F. New kinds of entropy. *Journal of Statistical Physics* **116,** 29–42 (2004).

234. Vliegenthart, G. A. & Gompper, G. Forced crumpling of self-avoiding elastic sheets. *Nature Materials* **5,** 216–221 (2006).

235. Gardel, M. L. *et al.* Elastic Behavior of Cross-Linked and Bundled Actin Networks. *Science* **304,** 1301–1305 (2004).

236. Blair, D. L. & Kudrolli, A. Geometry of Crumpled Paper. *Physical Review Letters* **94,** 166107 (2005).

237. Andresen, C. A., Hansen, A. & Schmittbuhl, J. Ridge network in crumpled paper. *Physical Review E* **76,** 026108 (2007).

238. Adda-Bedia, M., Boudaoud, A., Boué, L. & Debœuf, S. Statistical distributions in the folding of elastic structures. *Journal of Statistical Mechanics: Theory and Experiment* **2010** (2010).

239. Deboeuf, S., Adda-Bedia, M. & Boudaoud, A. Energy distributions and effective temperatures in the packing of elastic sheets. *EPL (Europhysics Letters)* **85,** 24002 (2009).

240. Andrejevic, J., Lee, L. M., Rubinstein, S. M. & Rycroft, C. H. A model for the fragmentation kinetics of crumpled thin sheets. *Nature Communications* **12,** 1470 (2021).

241. Balankin, A. S. & Flores-Cano, L. Edwards's statistical mechanics of crumpling networks in crushed self-avoiding sheets with finite bending rigidity. *Physical Review E - Statistical, Nonlinear, and Soft Matter Physics* **91,** 1–9 (2015).

242. Balankin, A. S. *et al.* Fractal features of a crumpling network in randomly folded thin matter and mechanics of sheet crushing. *Physical Review E* **87,** 052806 (2013).

243. Rehage, H., Husmann, M. & Walter, A. From two-dimensional model networks to microcapsules. *Rheologica Acta* **41,** 292–306 (2002).

244. Grima, J. N. *et al.* Tailoring Graphene to Achieve Negative Poisson's Ratio Properties. *Advanced Materials* **27,** 1455–1459 (2015).

245. Leal, F. C. B. & Gomes, M. A. F. Strain-strain relation in the unfolding of crumpled thin sheets. *Materials Research Express* **6,** 106407 (2019).

246. DUBKOV, A. A., SPAGNOLO, B. & UCHAIKIN, V. V. LÉVY FLIGHT SUPERDIFFUSION: AN INTRODUCTION. *International Journal of Bifurcation and Chaos* **18,** 2649–2672 (2008).

247. Leal, F. C. B. & Gomes, M. A. F. Unfolding of crumpled thin sheets. *Physical Review E* **106,** 025002 (2022).

248. Balankin, A. S. *et al.* Power law scaling of lateral deformations with universal Poisson's index for randomly folded thin sheets. *Physical Review B - Condensed Matter and Materials Physics* **77,** 3–7 (2008).

249. Choi, J. B. & Lakes, R. S. Analysis of elastic modulus of conventional foams and of re-entrant foam materials with a negative Poisson's ratio. *International Journal of Mechanical Sciences* **37,** 51–59 (1995).
250. Chan, N. & Evans, K. E. The Mechanical Properties of Conventional and Auxetic Foams. Part II: Shear. *Journal of Cellular Plastics* **35,** 166–183 (1999).
251. Alderson, K., Alderson, A., Ravirala, N., Simkins, V. & Davies, P. Manufacture and characterisation of thin flat and curved auxetic foam sheets. *Physica Status Solidi (B) Basic Research* **249.** ISBN: 4412049035, 1315–1321 (2012).
252. Tatlier, M. S. & Aksu, U. Simulation of auxetic behavior in planar random steel fiber networks. *International Journal of Applied Engineering Research* **12,** 3978–3987 (2017).
253. Domaschke, S., Morel, A., Fortunato, G. & Ehret, A. E. Random auxetics from buckling fibre networks. *Nature Communications* **10.** Publisher: Springer US ISBN: 4146701912757, 1–8 (2019).
254. Ye, M., Gao, L. & Li, H. A design framework for gradually stiffer mechanical metamaterial induced by negative Poisson's ratio property. *Materials and Design* **192.** Publisher: Elsevier Ltd (2020).
255. Wang, H., Xiao, S. & Wang, J. Disordered auxetic metamaterials architected by random peanut-shaped perturbations. *Materials and Design* **212.** Publisher: Elsevier Ltd (2021).
256. Lin, Y. C. *et al.* Spontaneous emergence of ordered phases in crumpled sheets. *Physical Review Letters* **103,** 1–4 (2009).
257. Hayase, Y. *et al.* Fold analysis of crumpled sheets using microcomputed tomography. *Physical Review E* **104.** arXiv: 2107.13836, 2–6 (2021).
258. Cambou, A. D. & Menon, N. Three-dimensional structure of a sheet crumpled into a ball. *Proceedings of the National Academy of Sciences of the United States of America* **108,** 14741–14745 (2011).
259. Cambou, A. D. & Menon, N. Orientational ordering in crumpled elastic sheets. *EPL (Europhysics Letters)* **112,** 14003 (2015).
260. Croll, A. B. *et al.* Sticky crumpled matter. *Matter* **5.** Publisher: Cell Press, 1792–1805 (2022).
261. Cranford, S. Crumpled sheets, fractal dimension, and wrinkles in research. *Matter* **5.** Publisher: Cell Press, 1627–1629 (2022).

262. Liao, Y. *et al.* Understanding the Role of Self-Adhesion in Crumpling Behaviors of Sheet Macromolecules. *Langmuir* **37.** Publisher: American Chemical Society, 8627–8637 (2021).
263. Van der Linden, E. & Versluis, P. Membrane crumpling and restricted swelling in onion phases. *Physica A: Statistical Mechanics and its Applications* **298,** 75–80 (2001).
264. Strey, R., Schomäcker, R., Roux, D., Nallet, F. & Olsson, U. Dilute lamellar and L_3 phases in the binary water–$C_{12}E_5$ system. *J. Chem. Soc., Faraday Trans.* **86,** 2253–2261 (1990).
265. Evans, E. & Rawicz, W. Entropy-driven tension and bending elasticity in condensed-fluid membranes. *Physical Review Letters* **64,** 2094–2097 (1990).
266. Bouaziz, O., Bouafif, R. & Massion, R. Sandwich materials with a crumpled aluminium core. *Metallurgical Research and Technology* **118** (2021).
267. Zadpoor, A. A. Meta-biomaterials. *Biomaterials Science* **8.** Publisher: Royal Society of Chemistry, 18–38 (2020).
268. Ganjian, M. *et al.* Controlled metal crumpling as an alternative to folding for the fabrication of nanopatterned meta-biomaterials. *Materials & Design* **220.** Publisher: Elsevier BV, 110844 (2022).
269. Elder, T. & Croll, A. B. Roughness tolerant pressure sensitive adhesives made of sticky crumpled sheets. *Soft Matter* **18,** 7866–7876 (2022).
270. Luo, J. *et al.* Compression and aggregation-resistant particles of crumpled soft sheets. *ACS Nano* **5,** 8943–8949 (2011).
271. Xu, X. *et al.* Highly crumpled graphene-like material as compression-resistant electrode material for high energy-power density supercapacitor. *Chemical Engineering Journal* **397.** Publisher: Elsevier B.V. (2020).
272. Dou, X. *et al.* Self-dispersed crumpled graphene balls in oil for friction and wear reduction. *Proceedings of the National Academy of Sciences* **113,** 1528–1533 (2016).
273. Lerner, M. I. *et al.* Crumpled Aluminum Hydroxide Nanostructures as a Microenvironment Dysregulation Agent for Cancer Treatment. *Nano Letters* **18.** Publisher: American Chemical Society, 5401–5410 (2018).
274. Liu, M., Fernandes, D. C., Saleeba, Z. S. & Hurt, R. H. Controlled Release of Molecular Intercalants from Two-Dimensional Nanosheet Films. *ACS Nano* **15.** Publisher: American Chemical Society, 20105–20115 (2021).

275. Tan, S., Zhong, C. & Langrish, T. Encapsulation of caffeine in spray-dried micro-eggs for controlled release: The effect of spray-drying (cooking) temperature. *Food Hydrocolloids* **108.** Publisher: Elsevier B.V. (2020).

276. Balankin, A. S. *et al.* Slow kinetics of water escape from randomly folded foils. *Physical Review E - Statistical, Nonlinear, and Soft Matter Physics* **83,** 1–4 (2011).

277. Habibi, M., Adda-Bedia, M. & Bonn, D. Effect of the material properties on the crumpling of a thin sheet. *Soft Matter* **13.** Publisher: Royal Society of Chemistry, 4029–4034 (2017).

278. Jackson, P. *Folding Techniques For Designers: From Sheet to Form* (Laurence King Publishing Ltd, London, 2011).

279. Rohmer, S., Merat, A., Floderer, V. & Copinet, A. *Geometric and topological modelling of 3D crumpled structures* in *INTERNATIONAL CONFERENCE ON ENGINEERING DESIGN* (Seoul, 2013), 1–8.

280. Rohmer, S., Mérat, A., Floderer, V. & Copinet, A. Graph based method for the modelling of crumpled structures. *Key Engineering Materials* **572.** Publisher: Trans Tech Publications Ltd ISBN: 9783037858196, 147–150 (2014).

281. Le CRIMP. *Portfolio Centre de Recherche International en Modélisation par le Pli* 2017.

282. Gompper, G. Patterns of stress in crumpled sheets. *Nature* **386,** 439–441 (1997).

283. Witten, T. A. How soft matter correlates: Three examples. *Journal of Physics Condensed Matter* **17** (2005).

284. Mirzaali, M. J., Habibi, M., Janbaz, S., Vergani, L. & Zadpoor, A. A. Crumpling-based soft metamaterials: the effects of sheet pore size and porosity. *Scientific Reports* **7.** Publisher: Springer US, 13028 (2017).

285. Farzam Rad, V., Ramírez-Miquet, E. E., Cabrera, H., Habibi, M. & Moradi, A.-R. Speckle pattern analysis of crumpled papers. *Applied Optics* **58.** Publisher: Optical Society of America, 6549 (2019).

286. Mermet-Guyennet, M. R. *et al.* Size-dependent reinforcement of composite rubbers. *Polymer* **73.** Publisher: Elsevier Ltd, 170–173 (2015).

287. Ayres, C. E. *et al.* Measuring fiber alignment in electrospun scaffolds: A user's guide to the 2D fast Fourier transform approach. *Journal of Biomaterials Science, Polymer Edition* **19.** ISBN: 1568562087840, 603–621 (2008).

288. Bradski, G. The OpenCV Library. *Dr. Dobb's Journal of Software Tools* (2000).

289. Harris, C. R. *et al.* Array programming with NumPy. *Nature* **585.** arXiv: 2006.10256 Publisher: Springer US, 357–362 (2020).

290. Zadpoor, A. A. Mechanical meta-materials. *Materials Horizons* **3.** Publisher: Royal Society of Chemistry, 371–381 (2016).

291. Gottesman, O., Andrejevic, J., Rycroft, C. H. & Rubinstein, S. M. A state variable for crumpled thin sheets. *Communications Physics* **1.** Publisher: Springer US, 1–7 (2018).

292. Eberle, A. P., Baird, D. G. & Wapperom, P. Rheology of non-Newtonian fluids containing glass fibers: A review of experimental literature. *Industrial and Engineering Chemistry Research* **47,** 3470–3488 (2008).

293. Fan, Z. & Advani, S. G. Rheology of multiwall carbon nanotube suspensions. *Journal of Rheology* **51,** 585–604 (2007).

294. Xue, N., Nunes, J. K. & Stone, H. A. Shear-induced migration of confined flexible fibers. *Soft Matter* **18.** Publisher: Royal Society of Chemistry, 514–525 (2022).

295. Grand, A. & Petekidis, G. Effects of particle softness on the rheology and yielding of colloidal glasses. *Rheologica Acta* **47,** 579–590 (2008).

296. Fuongfuchat, A. *et al.* Linear and non-linear viscoelastic behaviors of crosslinked tapioca starch/polysaccharide systems. *Journal of Food Engineering* **109.** Publisher: Elsevier Ltd, 571–578 (2012).

297. Precha-Atsawanan, S., Uttapap, D. & Sagis, L. M. Linear and nonlinear rheological behavior of native and debranched waxy rice starch gels. *Food Hydrocolloids* **85.** Publisher: Elsevier Ltd, 1–9 (2018).

298. Sun, Q., Jin, F., Liu, J. & Zhang, G. Understanding force chains in dense granular materials. *International Journal of Modern Physics B* **24,** 5743–5759 (2010).

299. Kim, D. Y. & Siegmund, T. Mechanics and design of topologically interlocked irregular quadrilateral tessellations. *Materials and Design* **212.** Publisher: Elsevier Ltd (2021).

300. Grill, M. J., Kernes, J., Slepukhin, V. M., Wall, W. A. & Levine, A. J. Directed force propagation in semiflexible networks. *Soft Matter* **17.** arXiv: 2006.15192 Publisher: Royal Society of Chemistry, 10223–10241 (2021).
301. Mann, A. *et al.* Force chains in cell–cell mechanical communication. *Journal of the Royal Society Interface* **16.** Publisher: Royal Society Publishing (2019).
302. Hansell, M. *Animal Architecture* (Oxford Animal Biology Series, Oxford, 2005).
303. Verhille, G., Moulinet, S., Vandenberghe, N., Adda-Bedia, M. & Gal, P. L. Structure and mechanics of aegagropilae fiber network. *Proc. Natl. Acad. Sci. USA* **114,** 4607–4612 (2017).
304. Brown, E., Nasto, A., Athanassiadis, A. G. & Jaeger, H. M. Strain Stiffening in Random Packings of Entangled Granular Chains. *Phys. Rev. Lett.* **108,** 108302 (2012).
305. Dumont, D. *et al.* Emergent Strain Stiffening in Interlocked Granular Chains. *Phys. Rev. Lett.* **120,** 088001 (2018).
306. Zou, L. N., Cheng, X., Rivers, M. L., Jaeger, H. M. & Nagel, S. R. The packing of granular polymer chains. *Science* **326,** 408–410 (2009).
307. Gómez, L. R., Garcia, N. A. & Pöschel, T. Packing structure of semiflexible rings. *Proc. Natl. Acad. Sci. USA* **117,** 3382–3387 (2020).
308. Soh, B. W., Gengaro, I. R., Klotz, A. R. & Doyle, P. S. Self-entanglement of a tumbled circular chain. *Phys. Rev. Res.* **1,** 033194 (2019).
309. Sarate, P. S., Murthy, T. G. & Sharma, P. Column to pile transition in quasi-static deposition of granular chains. *Soft Matter* **18,** 2054–2059 (2022).
310. Safford, K., Kantor, Y., Kardar, M. & Kudrolli, A. Structure and dynamics of vibrated granular chains: Comparison to equilibrium polymers. *Phys. Rev. E* **79,** 061304 (2009).
311. Samadi Taheri, F., Fazli, H., Doi, M. & Habibi, M. Granular chain escape from a pore in a wall in the presence of particles on one side: a comparison to polymer translocation. *Soft Matter* **14,** 5420–5427 (2018).
312. Sunami, H. *et al.* Rapid stem cell extraction and culture device for regenerative therapy using biodegradable nonwoven fabrics with strongly oriented fibers. *Adv. Mater. Interfaces* **9,** 2101776 (2022).

313. Hu, J., Meng, H., Li, G. & Ibekwe, S. I. A review of stimuli-responsive polymers for smart textile applications. *Smart Mater. Struct.* **21,** 053001 (2012).

314. Yun, Y. J., Hong, W. G., Kim, W.-J., Jun, Y. & Kim, B. H. A novel method for applying reduced graphene oxide directly to electronic textiles from yarns to fabrics. *Adv. Mater.* **25,** 5701–5705 (2013).

315. Poincloux, S., Adda-Bedia, M. & Lechenault, F. Geometry and elasticity of a knitted fabric. *Phys. Rev. X* **8,** 021075 (2018).

316. Haines, C. S. *et al.* New twist on artificial muscles. *Proc. Natl. Acad. Sci. USA* **113,** 11709–11716 (2016).

317. Mueth, D. M. *et al.* Signatures of granular microstructure in dense shear flows. *Nature* **406,** 385 (2000).

318. Losert, W., Bocquet, L., Lubensky, T. C. & Gollub, J. P. Particle Dynamics in Sheared Granular Matter. *Phys. Rev. Lett.* **85,** 1428–1431 (2000).

319. Shaebani, M. R. *et al.* Gravity Governs Shear Localization in Confined Dense Granular Flows. *Phys. Rev. Lett.* **127,** 278003 (2021).

320. Fenistein, D. & van Hecke, M. Wide shear zones in granular bulk flow. *Nature* **425,** 256 (2003).

321. Unger, T., Török, J., Kertész, J. & Wolf, D. E. Shear Band Formation in Granular Media as a Variational Problem. *Phys. Rev. Lett.* **92,** 214301 (2004).

322. R. Moosavi et. al. Coexistence and Transition between Shear Zones in Slow Granular Flows. *Phys. Rev. Lett.* **111,** 148301 (2013).

323. Aktas, B., Narang, Y. S., Vasios, N., Bertoldi, K. & Howe, R. D. A Modeling Framework for Jamming Structures. *Adv. Funct. Mater.* **31,** 2007554 (2021).

324. Kamani, K., Donley, G. J. & Rogers, S. A. Unification of the Rheological Physics of Yield Stress Fluids. *Phys. Rev. Lett.* **126,** 218002 (2021).

325. Matoz-Fernandez, D. A., Agoritsas, E., Barrat, J. L., Bertin, E. & Martens, K. Nonlinear Rheology in a Model Biological Tissue. *Phys. Rev. Lett.* **118,** 158105 (2017).

326. Rogers, S. Large amplitude oscillatory shear: Simple to describe, hard to interpret. *Phys. Today* **71,** 34–40 (2018).

327. Baggioli, M., Grieninger, S. & Soltanpanahi, H. Nonlinear Oscillatory Shear Tests in Viscoelastic Holography. *Phys. Rev. Lett.* **124,** 081601 (2020).
328. Tapadia, P., Ravindranath, S. & Wang, S. Q. Banding in entangled polymer fluids under oscillatory shearing. *Phys. Rev. Lett.* **96,** 196001 (2006).
329. Shaebani, M. R., Jose, R., Santen, L., Stankevicins, L. & Lautenschläger, F. Persistence-Speed Coupling Enhances the Search Efficiency of Migrating Immune Cells. *Phys. Rev. Lett.* **125,** 268102 (2020).
330. Z. Shojaaee et. al. An adaptive hierarchical domain decomposition method for parallel contact dynamics simulations of granular materials. *J. Comput. Phys.* **231,** 612–628 (2012).
331. Jean, M. The non-smooth contact dynamics method. *Comput. Methods Appl. Mech. Eng.* **177,** 235–257 (1999).
332. Shaebani, M. R., Unger, T. & Kertész, J. Generation of homogeneous granular packings: contact dynamics simulations at constant pressure using fully periodic boundaries. *Int. J. Mod. Phys. C* **20,** 847–867 (2009).
333. Thielicke, W. & Stamhuis, E. J. PIVlab - Towards User-friendly, Affordable and Accurate Digital Particle Image Velocimetry in MATLAB. *J. Open Res. Softw.* **2,** 1–10 (2014).
334. Sarno, L. *et al.* Challenges and improvements in applying a particle image velocimetry (PIV) approach to granular flows. *J. Phys. Conf. Ser.* **1249,** 012011 (2019).
335. Toiya, M., Stambaugh, J. & Losert, W. Transient and Oscillatory Granular Shear Flow. *Phys. Rev. Lett.* **93,** 088001 (2004).
336. Shaebani, M. R., Unger, T. & Kertész, J. Unjamming due to local perturbations in granular packings with and without gravity. *Phys. Rev. E* **78,** 011308 (2008).
337. Unger, T., Kertész, J. & Wolf, D. E. Force Indeterminacy in the Jammed State of Hard Disks. *Phys. Rev. Lett.* **94,** 178001 (2005).
338. Shaebani, M. R., Unger, T. & Kertész, J. Extent of force indeterminacy in packings of frictional rigid disks. *Phys. Rev. E* **79,** 052302 (2009).
339. Ward, A. *et al.* Solid friction between soft filaments. *Nat. Mater.* **14,** 583 (2015).

340. Goldenberg, C. & Goldhirsch, I. Friction enhances elasticity in granular solids. *Nature* **435,** 188–191 (2005).

341. Shaebani, M. R., Unger, T. & Kertész, J. Unjamming of granular packings due to local perturbations: Stability and decay of displacements. *Phys. Rev. E* **76,** 030301 (2007).

342. Negi, V. & Picu, R. C. Tensile behavior of non-crosslinked networks of athermal fibers in the presence of entanglements and friction. *Soft Matter* **17,** 10186–10197 (2021).

343. Stoop, N., Najafi, J., Wittel, F. K., Habibi, M. & Herrmann, H. J. Packing of Elastic Wires in Spherical Cavities. *Phys. Rev. Lett.* **106,** 214102 (2011).

344. Vetter, R., Wittel, F. K. & Herrmann, H. J. Morphogenesis of filaments growing in flexible confinements. *Nat. Commun.* **5,** 4437 (2014).

345. Steinfeld, H. *et al. Livestock's Long Shadow: Environmental Issues and Options* (Food and Agriculture Organization of the United Nations, 2006).

346. Clark, B., Stewart, G. B., Panzone, L. A., Kyriazakis, I. & Frewer, L. J. Citizens, consumers and farm animal welfare: A meta-analysis of willingness-to-pay studies. *Food Policy* **68.** Publisher: Elsevier Ltd, 112–127 (2017).

347. Micha, R., Wallace, S. K. & Mozaffarian, D. Red and processed meat consumption and risk of incident coronary heart disease, stroke, and diabetes mellitus: A systematic review and meta-analysis. *Circulation* **121,** 2271–2283 (2010).

348. McAfee, A. J. *et al.* Red meat consumption: An overview of the risks and benefits. *Meat Science* **84.** Publisher: Elsevier Ltd, 1–13 (2010).

349. Dekkers, B. L., Boom, R. M. & van der Goot, A. J. Structuring processes for meat analogues. *Trends in Food Science and Technology* **81.** Publisher: Elsevier Ltd, 25–36 (2018).

350. Dekkers, B. L., Emin, M. A., Boom, R. M. & van der Goot, A. J. The phase properties of soy protein and wheat gluten in a blend for fibrous structure formation. *Food Hydrocolloids* **79,** 273–281 (2018).

351. Michel, F., Hartmann, C. & Siegrist, M. Consumers' associations, perceptions and acceptance of meat and plant-based meat alternatives. *Food Quality and Preference* **87,** 104063 (2021).

352. Hoek, A. C. *et al.* Replacement of meat by meat substitutes. A survey on person- and product-related factors in consumer acceptance. *Appetite* **56,** 662–673 (2011).

353. Muliawan, E. B. & Hatzikiriakos, S. G. Rheology of mozzarella cheese: Extrusion and rolling. *International Dairy Journal* **18,** 615–623 (2008).

354. Sheikh, F., Hasani, M., Kiani, H., JavadAsadollahzadeh, M. & Seyfi, J. Investigation of textural, rheological and sensory properties of white cheese analog containing sesame seeds oleosome. *Journal of Food Measurement and Characterization* **17,** 63–74 (2023).

355. Lyu, Z., Sala, G. & Scholten, E. Water distribution in maize starch-pea protein gels as determined by a novel confocal laser scanning microscopy image analysis method and its effect on structural and mechanical properties of composite gels. *Food Hydrocolloids* **133,** 107942 (2022).

356. Liu, X., Sala, G. & Scholten, E. Structural and functional differences between ice crystal-dominated and fat network-dominated ice cream. *Food Hydrocolloids* **138,** 108466 (2023).

357. Feichtinger, A. *et al.* Protein oleogels prepared by solvent transfer method with varying protein sources. *Food Hydrocolloids* **132,** 107821 (2022).

358. Tan, K., Cheng, S., Jugé, L. & Bilston, L. E. Characterising soft tissues under large amplitude oscillatory shear and combined loading. *Journal of Biomechanics* **46,** 1060–1066 (2013).

359. Capilnasiu, A., Bilston, L., Sinkus, R. & Nordsletten, D. Nonlinear viscoelastic constitutive model for bovine liver tissue. *Biomechanics and Modeling in Mechanobiology* **19.** Publisher: Springer Berlin Heidelberg ISBN: 1023702001297, 1641–1662 (2020).

360. Ayyildiz, M., Aktas, R. G. & Basdogan, C. Effect of solution and postmortem time on mechanical and histological properties of liver during cold preservation. *Biorheology* **51,** 47–70 (2014).

361. Ayyildiz, M., Cinoglu, S. & Basdogan, C. Effect of normal compression on the shear modulus of soft tissue in rheological measurements. *Journal of the Mechanical Behavior of Biomedical Materials* **49.** Publisher: Elsevier, 235–243 (2015).

362. Liu, Z. & Bilston, L. On the viscoelastic character of liver tissue: Experiments and modelling of the linear behaviour. *Biorheology* **37,** 191–201 (2000).

363. Bilston, L. E., Liu, Z. & Phan-Thien, N. Linear viscoelastic properties of bovine brain tissue in shear. *Biorheology* **34,** 377–385 (1997).

364. Bilston, L. E., Liu, Z. & Phan-Thien, N. Large strain behaviour of brain tissue in shear: Some experimental data and differential constitutive model. *Biorheology* **38,** 335–345 (2001).

365. Nicolle, S., Lounis, M., Willinger, R. & Palierne, J. F. Shear linear behavior of brain tissue over a large frequency range. *Biorheology* **42,** 209–223 (2005).

366. Melito, H., Daubert, C. & Foegeding, E. Relating Large Amplitude Oscillatory Shear and Food Behavior: Correlation of Nonlinear Viscoelastic, Rheological, Sensory and Oral Processing Behavior of Whey Protein Isolate/kappa-Carrageenan Gels. *Journal of Food Process Engineering* **36,** 521–534 (2013).

367. Schreuders, F. K. G., Sagis, L. M. C., Bodnár, I., Boom, R. M. & van der Goot, A. J. Non-linear rheology reveals the importance of elasticity in meat and meat analogues. *Scientific Reports* **12.** Publisher: Springer Science and Business Media LLC (2022).

368. Tan, K., Cheng, S., Jugé, L. & Bilston, L. E. Characterising skeletal muscle under large strain using eccentric and Fourier Transform-rheology. *Journal of Biomechanics* **48,** 3788–3795 (2015).

369. Paredes, J., Cortizo-Lacalle, D., Imaz, A. M., Aldazabal, J. & Vila, M. Application of texture analysis methods for the characterization of cultured meat. *Scientific Reports* **12,** 3898 (2022).

370. De Cagny, H. C. *et al.* Porosity governs normal stresses in polymer gels. *Physical Review Letters* **117.** arXiv: 1605.04139, 1–5 (2016).

371. Vahabi, M. *et al.* Normal stresses in semiflexible polymer hydrogels. *Physical Review E* **97.** arXiv: 1712.02733 Publisher: American Physical Society, 32418 (2018).

372. Schreuders, F. K. *et al.* Comparing structuring potential of pea and soy protein with gluten for meat analogue preparation. *Journal of Food Engineering* **261,** 32–39 (2019).

373. Krintiras, G. A., Gadea Diaz, J., van der Goot, A. J., Stankiewicz, A. I. & Stefanidis, G. D. On the use of the Couette Cell technology for large scale production of textured soy-based meat replacers. *Journal of Food Engineering* **169,** 205–213 (2016).

R

374. Obuz, E., Dikeman, M., Erickson, L., Hunt, M. & Herald, T. Predicting temperature profiles to determine degree of doneness for beef biceps femoris and longissimus lumborum steaks. *Meat Science* **67,** 101–105 (2004).

375. Głuchowski, A., Czarniecka-Skubina, E. & Buła, M. The Use of the Sous-Vide Method in the Preparation of Poultry at Home and in Catering—Protection of Nutrition Value Whether High Energy Consumption. *Sustainability* **12,** 7606 (2020).

376. Martikainen, L., Bertula, K., Turunen, M. & Ikkala, O. Strain stiffening and negative normal force of agarose hydrogels. *Macromolecules* **53,** 9983–9992 (2020).

377. Habibi, M., Dinkgreve, M., Paredes, J., Denn, M. & Bonn, D. Normal stress measurement in foams and emulsions in the presence of slip. *Journal of Non-Newtonian Fluid Mechanics* **238,** 33–43 (2016).

378. McKinley, G. H., Byars, J. A., Brown, R. A. & Armstrong, R. C. Observations on the elastic instability in cone-and-plate and parallel-plate flows of a polyisobutylene Boger fluid. *Journal of Non-Newtonian Fluid Mechanics* **40,** 201–229 (1991).

379. Schwartz, M., Marais, J., Strydom, P. E. & Hoffman, L. C. Effects of increasing internal end-point temperatures on physicochemical and sensory properties of meat: A review. *Comprehensive Reviews in Food Science and Food Safety* **21,** 2843–2872 (2022).

380. Birbaum, F. C., Haavisto, S., Koponen, A., Windhab, E. J. & Fischer, P. Shear localisation in interfacial particle layers and its influence on Lissajous-plots. *Rheologica Acta* **55,** 267–278 (2016).

381. Mermet-Guyennet, M. R. B. *et al.* LAOS: The strain softening/strain hardening paradox. *Journal of Rheology* **59.** Publisher: Society of Rheology, 21–32 (2015).

382. García-Segovia, P., Andrés-Bello, A. & Martínez-Monzó, J. Effect of cooking method on mechanical properties, color and structure of beef muscle (M. pectoralis). *Journal of Food Engineering* **80,** 813–821 (2007).

383. Balbi, V., Trotta, A., Destrade, M. & Ní Annaidh, A. Poynting effect of brain matter in torsion. *Soft Matter* **15.** arXiv: 1811.00832 Publisher: Royal Society of Chemistry, 5147–5153 (2019).

384. Sun, Y. *et al.* Origami-inspired folding assembly of dielectric elastomers for programmable soft robots. *Microsystems & Nanoengineering* **8,** 37 (2022).

385. Lv, C., Krishnaraju, D., Konjevod, G., Yu, H. & Jiang, H. Origami based mechanical metamaterials. *Scientific Reports* **4.** Publisher: Nature Publishing Group (2014).

386. Zhang, X., Wang, S., Durandet, Y., Palanisamy, S. & Lu, G. Energy absorption behavior of origami bellows under tension. *International Journal of Mechanical Sciences* **246,** 108143 (2023).

387. Hu, J., Li, H. & Chen, W. A squid-inspired swimming robot using folding of origami. *The Journal of Engineering* **2021,** 630–639 (2021).

388. Chen, W.-H. *et al.* A Programmably Compliant Origami Mechanism for Dynamically Dexterous Robots. *IEEE Robotics and Automation Letters* **5,** 2131–2137 (2020).

389. Westra, K., Dunne, F., Kulsa, S., Hunt, M. & Leachman, J. Compliant polymer origami bellows in cryogenics. *Cryogenics* **114,** 103226 (2021).

390. Reid, A., Lechenault, F., Rica, S. & Adda-Bedia, M. Geometry and design of origami bellows with tunable response. *Physical Review E* **95.** arXiv: 1609.01354, 1–10 (2017).

391. Suh, J.-E., Kim, T.-H. & Han, J.-H. New Approach to Folding a Thin-Walled Yoshimura Patterned Cylinder. *Journal of Spacecraft and Rockets* **58,** 516–530 (2021).

392. Horgan, C. O. & Murphy, J. G. Poynting and reverse Poynting effects in soft materials. *Soft Matter* **13.** Publisher: Royal Society of Chemistry, 4916–4923 (2017).

393. Horgan, C. O. & Murphy, J. G. Fiber-Matrix Interaction and Fiber Orientation in Simple Shearing of Fibrous Soft Tissues. *Journal of Elasticity* (2021).

394. Criscione, J. C., Lorenzen-Schmidt, I., Humphrey, J. D. & Hunter, W. C. Mechanical Contribution of Endocardium During Finite Extension and Torsion Experiments on Papillary Muscles. *Annals of Biomedical Engineering* **27,** 123–130 (1999).

395. Horgan, C. O. & Murphy, J. G. On the modeling of extension-torsion experimental data for transversely isotropic biological soft tissues. *Journal of Elasticity* **108,** 179–191 (2012).

396. Kanner, L. M. & Horgan, C. O. On extension and torsion of strain-stiffening rubber-like elastic circular cylinders. *Journal of Elasticity* **93,** 39–61 (2008).

397. Anssari-Benam, A. & Horgan, C. O. Extension and torsion of rubber-like hollow and solid circular cylinders for incompressible isotropic hyperelastic materials with limiting chain extensibility. *European Journal of Mechanics, A/Solids* **92.** Publisher: Elsevier Ltd (2022).

398. Del Álamo, J. C., Norwich, G. N., Li, Y.-s. J., Lasheras, J. C. & Chien, S. Anisotropic rheology and directional mechanotransduction in vascular endothelial cells. *Proceedings of the National Academy of Sciences* **105,** 15411–15416 (2008).

399. Duclut, C., Paijmans, J., Inamdar, M. M., Modes, C. D. & Jülicher, F. Nonlinear rheology of cellular networks. *Cells & Development* **168,** 203746 (2021).

400. The mechanism of plastic deformation of crystals. Part I.—Theoretical. *Proceedings of the Royal Society of London. Series A, Containing Papers of a Mathematical and Physical Character* **145,** 362–387 (1934).

401. Goodrich, C. P., Liu, A. J. & Nagel, S. R. Solids between the mechanical extremes of order and disorder. *Nature Physics* **10,** 578–581 (2014).

402. Schlegel, M., Brujic, J., Terentjev, E. M. & Zaccone, A. Local structure controls the nonaffine shear and bulk moduli of disordered solids. *Scientific Reports* **6,** 18724 (2016).

403. Falk, M. L. & Langer, J. S. Dynamics of viscoplastic deformation in amorphous solids.

404. Argon, A. Plastic deformation in metallic glasses. *Acta Metallurgica* **27,** 47–58 (1979).

405. Chen, M. Mechanical Behavior of Metallic Glasses: Microscopic Understanding of Strength and Ductility. *Annual Review of Materials Research* **38,** 445–469 (2008).

406. Zhang, M., Wang, Y. & Dai, L. Bridging shear transformation zone to the atomic structure of amorphous solids. *Journal of Non-Crystalline Solids* **410,** 100–105 (2015).

407. Manning, M. L., Langer, J. S. & Carlson, J. M. Strain localization in a shear transformation zone model for amorphous solids. *Physical Review E* **76,** 056106 (2007).

408. Hayman, N. W., Ducloué, L., Foco, K. L. & Daniels, K. E. Granular Controls on Periodicity of Stick-Slip Events: Kinematics and Force-Chains in an Experimental Fault. *Pure and Applied Geophysics* **168,** 2239–2257 (2011).

409. Zhou, L., Cook, L. & McKinley, G. H. Probing shear-banding transitions of the VCM model for entangled wormlike micellar solutions using large amplitude oscillatory shear (LAOS) deformations. *Journal of Non-Newtonian Fluid Mechanics* **165,** 1462–1472 (2010).

410. Carter, K. A., Girkin, J. M. & Fielding, S. M. Shear banding in large amplitude oscillatory shear (LAOStrain and LAOStress) of polymers and wormlike micelles. *Journal of Rheology* **60,** 883–904 (2016).

411. Radhakrishnan, R. & Fielding, S. M. Shear banding in large amplitude oscillatory shear (LAOStrain and LAOStress) of soft glassy materials. *Journal of Rheology* **62,** 559–576 (2018).

412. Manzano, H., Masoero, E., Lopez-Arbeloa, I. & Jennings, H. M. Shear deformations in calcium silicate hydrates. *Soft Matter* **9,** 7333 (2013).

413. Mandal, R., Casert, C. & Sollich, P. Robust prediction of force chains in jammed solids using graph neural networks. *Nature Communications* **13,** 4424 (2022).

414. Desmond, K. W., Young, P. J., Chen, D. & Weeks, E. R. Experimental study of forces between quasi-two-dimensional emulsion droplets near jamming. *Soft Matter* **9,** 3424 (2013).

415. Katgert, G. & van Hecke, M. Jamming and geometry of two-dimensional foams. *EPL (Europhysics Letters)* **92,** 34002 (2010).

416. Delarue, M. *et al.* Self-driven jamming in growing microbial populations. *Nature Physics* **12,** 762–766 (2016).

417. Mandal, R., Bhuyan, P. J., Chaudhuri, P., Dasgupta, C. & Rao, M. Extreme active matter at high densities. *Nature Communications* **11,** 2581 (2020).

418. Daub, E. G. & Carlson, J. M. Friction, Fracture, and Earthquakes. *Annual Review of Condensed Matter Physics* **1,** 397–418 (2010).

419. Hsu, T.-S. in *Earthquakes - Forecast, Prognosis and Earthquake Resistant Construction* (ed Svalova, V.) (InTech, 2018).

420. Perepezko, J. H., Imhoff, S. D., Chen, M.-W., Wang, J.-Q. & Gonzalez, S. Nucleation of shear bands in amorphous alloys. *Proceedings of the National Academy of Sciences* **111,** 3938–3942 (2014).

421. Divoux, T., Fardin, M. A., Manneville, S. & Lerouge, S. Shear Banding of Complex Fluids. *Annual Review of Fluid Mechanics* **48,** 81–103 (2016).

422. Boukany, P. E., Wang, S.-Q., Ravindranath, S. & Lee, L. J. Shear banding in entangled polymers in the micron scale gap: a confocal-rheoscopic study. *Soft Matter* **11,** 8058–8068 (2015).

423. Wickeler, A. L. & Naguib, H. E. Novel origami-inspired metamaterials: Design, mechanical testing and finite element modelling. *Materials & Design* **186,** 108242 (2020).

424. Van Der Sman, R. G. M. & Van Der Goot, A. J. The science of food structuring. *Soft Matter* **5,** 501–510 (2009).

425. Pascua, Y., Koç, H. & Foegeding, E. A. Food structure: Roles of mechanical properties and oral processing in determining sensory texture of soft materials. *Current Opinion in Colloid & Interface Science* **18,** 324–333 (2013).

426. ISO. *Sensory analysis — Vocabulary (ISO 5492:2008)* Geneva, Switzerland, 2008.

427. Cadbury. *Cadbury Flake* Accessed April 26, 2023. https://www.cadbury.co.uk/products/cadbury-flake-11309. 2020.

428. NMK Channel. *Easily make Chocolate Flakes* Accessed April 26, 2023. https://www.youtube.com/watch?v=TFL3rdyFkjc. 2017.

429. Gomes, M. A., Donato, C. C., Campello, S. L., De Souza, R. E. & Cassia-Moura, R. Structural properties of crumpled cream layers. *Journal of Physics D: Applied Physics* **40,** 3665–3669 (2007).

430. Rohmer, S. & Merat, A. *Innovative design of culinary moulds based on crumpled papers* in *13th International Design Conference (Design2014)* (2014), 2147–2156.

431. He, X. *et al.* Mechanism of Controlled Release of Vancomycin from Crumpled Graphene Oxides. *ACS Omega* **4,** 12252–12258 (2019).

432. Spence, C., Corujo, A. & Youssef, J. Cotton candy: A gastrophysical investigation. *International Journal of Gastronomy and Food Science* **16,** 100146 (2019).

R

433. Liu, Z., Zhang, M., Bhandari, B. & Wang, Y. 3D printing: Printing precision and application in food sector. *Trends in Food Science & Technology* **69,** 83–94 (2017).

434. Phuhongsung, P., Zhang, M., Devahastin, S. & Mujumdar, A. S. Defects in 3D/4D food printing and their possible solutions: A comprehensive review. *Comprehensive Reviews in Food Science and Food Safety* **21,** 3455–3479 (2022).

435. Liu, K. & Paulino, G. H. Nonlinear mechanics of non-rigid origami: an efficient computational approach. *Proceedings of the Royal Society A: Mathematical, Physical and Engineering Sciences* **473,** 20170348 (2017).

436. Teng, X., Zhang, M. & Mujumdar, A. S. 4D printing: Recent advances and proposals in the food sector. *Trends in Food Science & Technology* **110,** 349–363 (2021).

437. Navaf, M. *et al.* 4D printing: a new approach for food printing; effect of various stimuli on 4D printed food properties. A comprehensive review. *Applied Food Research* **2,** 100150 (2022).

Summary

All materials present different levels of structural order at different length scales. From a soft matter perspective, microscopically ordered materials are often represented by crystalline lattices, whereas disordered materials are most often depicted by glasses or other amorphous solids such as foams or emulsions. For such materials, understanding the relation between the structural components and the response under deformations is a requirement to employ them in any practical application. However, this proves to be a difficult task when the components are at the microscopic scale. It is therefore not surprising that model systems have arisen to understand microscopic structures with macroscopic analogues, where the structural components are more easily accessed or visualized. In this regard, studying the behavior of materials under shearing deformations can help elucidate how the specific structures respond to stress and interact in the system. Therefore, studying the materials with different levels of order at the macroscopic scale under shearing deformations can lead to future insights into geometric ingredients and the behavior of ordered or disordered solids at different length scales. Furthermore, a deeper understanding of how macroscopic structures behave under large shear deformations, where is the stress localized, and how is the energy dissipated or stored, will facilitate the future employment of such structures for building new materials ranging from metamaterials to food products.

When it comes to macroscopic model systems for disordered materials, crumpled materials and granular chains have been previously proposed in literature. In **Chapter 1** we provide a brief introduction to

these two systems, and how they have been previously used in literature to obtain insights into microscopic disordered solids. We then introduce our chosen systems for studying the structural components of the disordered systems, but in ordered arrangements. The structural components of crumpled materials, a random network of folds and vertices, is present in an ordered manner in origami shells with ordered patterns of folds. Whereas the structural components of granular chains and ropes, semi-flexible quasi-1D objects, are present in anisotropic meat and meat analogues in the form of fibrous structures. Then we introduce the shear rheology, both linear and nonlinear, used throughout this thesis to understand the different systems.

In chapter **Chapter 2** we performed a review on the current understanding of crumpled materials, from an amorphous solid perspective. We discuss how these systems have been studied in the past, and what previous literature has reported on similarities between crumpled materials and other disordered systems such as glasses, emulsions, or granular materials. Crumpled materials present a metastable energy landscape where the frustration of components prevents the relaxation to global energy minima. Mostly the study of the material's relaxation, or deformation under a constant force, i.e., creep experiments, have pointed to these similarities, where the results in different studies were interpreted using stretched exponential or logarithmic models, commonly applied in the study of complex relaxation of amorphous systems. Further research drew parallels between the memory effect of crumpled structures and glasses. Attempts have also arisen in recent years to apply the statistical mechanics of athermal solids to crumpled configurations. We end the review by proposing a design principle to make crumpled origami-like structures where disorder is introduced into the otherwise ordered configuration that is origami.

In chapter **Chapter 3**, we studied how bulk crumpled configurations behave under shear, both in short and large amplitude oscillatory deformations. We systematically modified different parameters, i.e., training of the material, internal morphology, friction, and plasticity effect to study each parameter's individual contribution to the shear response.

By training crumpled paper, we observed a decrease in long range correlations that formed force chains, which lead to an increase of shear modulus with compaction, not observed for untrained paper. The orientation of the internal stacked layers also influenced the shear response: layers parallel to shear resulted in lower storage modulus and increased dissipation via layer sliding, as opposed to perpendicular layer orientations. Lower surface friction facilitated the internal rearrangement of energy-focusing regions during shear deformations.

Changing to a different disordered material, in **Chapter 4** we studied the effect of chain length on entangled granular chains and ropes. We combined short and large amplitude oscillatory shear experiments with image analysis and simulations to understand the effect of entanglements. We observed that a universal transition occurs from narrow to wide shear zones encompassing various lengths, flexibilities, and materials. The critical deflection angle for the transition is aligned with the onset of stiffening in the system as measured directly from the torque. We found scaling laws for the width of the transition and the shear zone, and for the increase of stiffness with chain length. Our results indicate that the entanglements become activated under increasing deformations, and span through the system for sufficiently long chains.

We studied two ordered systems in this thesis. First, in **Chapter 5** we studied meat and meat analogue samples with anisotropic structure in an ordered arrangement. Meat contains a naturally created anisotropic structure, where the skeletal muscle fibers have a specific orientation. Meat analogues trying to mimic whole-cut meat sample contain fibrous structures created, in this case, via shear structuring plant protein samples inside a Couette cell. Methods that quantitatively compare the structures of whole-cut meat samples and meat analogues under deformations, taking into consideration the fibrous structure orientation, are still scarce. For this reason, we used a combination of non-linear shear rheology and shear-induced normal stress measurements to study the effect of structure orientations in beef, chicken, and fibrous model systems made with soy or pea protein isolates combined with wheat gluten. We observed differences in the mechanical response with different orientations for all samples, except the pea protein-wheat gluten sample. Furthermore, via large amplitude oscillatory rheology we observed rearrangements in meat at small strains, and lower energy dissipation at large strains. The more elastic fibers in the meat samples at the same time showed a larger normal stress response (larger Poynting modulus) and showed large differences in magnitude between different fiber orientations. The meat analogues, on the contrary, behave more solid-like at small strains where rearrangements cannot occur, and showed greater energy dissipation than meat at larger strains due to structure breakdown. The study, therefore, emphasizes the importance of fiber orientation in the rheology of plant-based meat analogues, and provides a methodology to quantitatively compare their mechanical responses to real meat, aiding in the development of new plant-based alternatives.

In our last experimental chapter, **Chapter 6**, we studied the second ordered system: Kresling and Yoshimura origami bellows presenting an ordered arrangement with well-defined patterns of folds, but different symmetry with respect to the shear direction. In addition, we investigated a third sample with a semi-ordered pattern: crumpled cylinder created via buckling under compression, which presents a semi-ordered arrangement but an *a priori* unknown asymmetry. Origami bellows are often studied under uni-axial deformations, but their mechanical response under shear is still poorly investigated. Specifically, the shear-induced normal force response of such structures has received little attention. For the Yoshimura design, having a symmetric structure with both shear directions, a Poynting effect was observed and fit with a quadratic relation to obtain the Poynting modulus. The Kresling design, having an asymmetric structure with the shear directions showed a linear relation with a positive or negative normal force depending on the direction of shear, and was fit with a linear approximation of the shifted (due to asymmetry) quadratic Poynting relation. For the crumpled cylinders the level of asymmetry in the pattern of the semi-random folds was quantified via an asymmetry index from the 2D Fast Fourier transform spectrum of the crease pattern images, which was well correlated to the asymmetry of the normal force response. Therefore, we found that in all these structures, the shear-induced normal force response is linked to the structural imperfections, order, and (a)symmetry, and provided a deeper understanding of the nonlinear mechanical response of origami bellows. These findings provide opportunities for programming the shear and shear-induced normal responses of origami cylinders, and using crumpling as a design principle for fabricating new metastructures.

Finally, in the general discussion in **Chapter 7** we provided an overview of the studied systems and main results. Then, we discussed the results of the thesis from a broader perspective of material deformations and stress/strain localization at different length scales. While the deformations in crystalline solids are generally well understood, mechanics of disordered solids such as glasses is still ill understood. We explain how the deformations in our macroscopically disordered system (crumpled materials) show similarities with the proposed basic units of plastic deformations in literature, known as shear transformation zones (STZs). Such STZs, have been used to understand deformations from the microscopic scale with glasses, to the macroscopic scale with geological faults. STZs are furthermore hypothesized to act as nucleation points for the formation of macroscopic shear bands in literature, which we linked to our study with granular chains and width of sheared zones through the stress localization on the chains. Therefore, both crumpled systems and granular chains could be used in future studies to understand the deformation events in other types of disordered solids at different length scales. In the two ordered systems we studied, the use of non-linear rheology also informed us about the stress localization in such systems: in the connective tissue between fibers in the case of meat samples, and in the pattern of folds in ordered and disordered origami bellows. The results from this thesis, therefore, unveil new possibilities for controlling the interplay between stress-bearing elements in macroscale model systems. The insights gained from our study can potentially contribute to the future development of new materials and structures with tunable mechanical properties for various applications. Furthermore, these insights can inform our understanding of the fundamental principles governing the behavior of different systems under stress.

Acknowledgments

My journey in the group of *Physics and Physical Chemistry of Foods* (FPH) started even before my PhD did, with my M.Sc. thesis. But time flies, and after many years this journey comes to an end. Despite all the individual effort that a PhD involves, it would go nowhere without the help and collaboration of many people along the way.

First of all, I would like to thank my daily supervisor **Mehdi** (Dr. Habibi) for always being available to resolve my doubts, providing quick feedback on my drafts, and in general for his support during our weekly meetings and teachings during my whole PhD. And above all, for his trust offering me the opportunity to do this PhD. Secondly, my promotor **Erik** (Prof. van der Linden) for all our insightful discussions, each of them being close to a brainstorming session with plenty of new ideas not only about my thesis, but of science as a whole. Each of those afternoons together going through my drafts point by point were inspiring.

Besides my supervisors, many people contributed to the chapters in this thesis. I would like to specially thank **Leonard** (Dr. Sagis), who despite not being involved officially in my PhD, was like a third supervisor solving all my LAOS related doubts and teaching me about bulk and interfacial rheology in our many collaborations. I also acknowledge the special contributions of **Melika** (Dr. Motaghian) for her help in writing the review that is Chapter 2 and the fun times we had during these years; **Reza** (Dr. Shaebani) for his collaboration in performing the simulations, help in writing the manuscript for Chapter 4, and insightful discussions; **Atze Jan** (Prof. van der Goot) for his contributions and input on meat analogues in Chapter 5; and **Aref** (Dr. Ghorbani) for performing the simulations for Chapter 6, his extensive knowledge on metamaterials, and all the nice conversations we got to have during these years. Also equally important, I acknowledge the help of the students I supervised during these four years. **Dong** and **Yiyun**, who helped me better understand some of the systems I was working with. **Qixin** for his help on experiments for interfacial rheology that turned into two manuscripts. **Sybren** for his enthusiasm and help in obtaining the experimental results for Chapter 4. **Mats** for his interest in meat analogues and help in getting the results for Chapter 5. And finally, **Soon Yuan** for starting the experiments which turned into Chapter 6.

Without the people at FPH, my PhD experience would have been very different, and for that there is many people to thank. **Els**, for her kind support, and resolving all my doubts about administrative matters during my PhD (and help me book my defense date at 9:00 sharp!). During my lab work, I spent countless hours in front of (or fighting with) the rheometers, and if I somehow succeeded is thanks to **Harry** and **Floris**, who helped me with the rheometers almost 24/7. **Elke** for constantly taking care of the social aspects within FPH. Without her there would be no ”family” feeling at FPH. **Guido** for all the invitations for sport sessions and insights into training. I also thank the other staff at FPH: **David**, **Roy**, **Karlijn**, **Paul**, **Arjen**, **Jasper**, **Maruschka**, and **Mark** who also offered their support and help during diverse activities throughout my PhD.

During my time at FPH, I was lucky to share the office Y0011 with great colleagues too. **Zhihong**, thank you for welcoming me into the office on my first day as a PhD student, and for sharing many laughs over these past years. **Xilong**, thank you for our endless discussions about science, foods, politics, and life in general! And for cooking dumplings for me. I hope to visit you both some time in China. **Annika**, thank you for bringing a charming attitude to our office every day and for all the nice talks about PhD students’ mental health. **Xiangyu**, thank you for organizing nice hot pot dinners. **Nana** thank you for the nice insights into Chinese foods I should try. **Chaya** and **Chon**, thank you for the nice office diners and sporadic discussions on differences between Asia and Europe. **Ashoka** despite the short stay in our department, thank you for encouraging me to visit and learn about Sri Lanka. I hope to visit it soon! **Senna**, thanks for providing with great homemade cakes on a regular basis!

I shared great moments with many members of FPH and other departments at WUR. **Philipp**, thank you for our friendship, which started when I was still a bachelor student, guiding me through the initial stages of my PhD, and the meetings in Utrecht every time you visit NL! **Belinda**, thank you for all the interesting discussions, and sharing your passion about Indonesian culture and food. **Jack**, thank you for helping and teaching me about interfacial rheology when I was still an MSc student, and for all the enjoyable collaborations and trips to conferences that emerged during my PhD. **Lei**, thank you for all the nice coffee breaks with many laughs and encouragement that lifted my mood every time. **Claudine**, thank you for all the nice chats we had, specially about our dilemmas of living abroad and missing home (and ethics about proper referencing of pictures). **Ahmed**, thank you for the many laughs every time I came to bother you at your office, the sport sessions in our trips for conferences, and for being my paranymph! **Remco** thank you for the encouragement and perspective on the PhD process from your experience. **Nirzar** thank you for the tips on all-things spicy foods. Too bad I did not get to learn from you how to make kimchi. **Wenjie** thank you for being my main competitor on booking the rheometers, and the fun we had about it. **Naomi**, thank you for the many chats we had in Spanish so that I could rest my brain from the English! **Yifan**, thank you for constant encouragement on my Chinese learning, and pointing out how it was getting worse during the last months of my thesis, when I stopped learning it. I plan to take on it again after finishing the PhD! **Cristina**, gracias por todos los breaks, las sesiones de deporte cada semana, el roadtrip de Madrid a Wageningen, por ser my paranymph, y en general por la amistad estos años desde antes del PhD!

Thanks all other people from FPH with whom I had the luck to share coffee breaks or international dinners: **Qi**, **Diana**, **Ting**, **Bo**, **An-**

teun, **Marco**, **Luka**, **Monica**, **Naoya**, **Ornicha**, **Robert**, **Huifang**, **Penghui**, **Raisa**, **Thiemo**, **Ting**, **Evelen**, **Shuzo**, **Xudong**, **Ngamjit**, **Parisa**, **Wanting**, **Cai (Yang)**, **Ziyang**, **Ninna**, **Mengyue**, **Dieke**. I got to learn things from all of you on one way or another, scientifically, about life in general, and other cultures.

Finalment, vull fer uns agraïments especials. En primer lloc, Alba, que has fet de tots estos anys una aventura al marge del doctorat mateix. Des de les pràctiques a Berlin, a la quarentena tancats a Vilafranca, i després els últims anys vivint a Utrecht. Per les incontables series a casa, viatges que hem fet (i farem), i tots els menjars que hem tingut l'oportunitat de provar. No podria haver tingut millor companya de viatge durant el doctorat, i pel que vindrà d'ací endavant. Gràcies per aguantar-me en els meus moments d'estrés, i especialment els últims mesos.

I per descomptat, als meus pares, Marisa i Vicent. Ha sigut gràcies a vosaltres, a tot el vostre suport per a la meua educació, i per ensenyar-me a mantindre una actitut crítica, fonamental per a la investigació, que he arribat fins ací. Ha sigut un procés llarg, i molts anys als Països Baixos, però per fi aquesta etapa arriba al seu final. Tornem a casa!

About the author

Gerard Giménez I Ribes was born on February 20, 1993, in València, Spain. He obtained his BSc in Food Science and Technology from the Technical University of Valencia (UPV) (2011-2016). During the academic year 2014-2015 he was an Erasmus exchange student at Wageningen University and Research, Netherlands (2014-2015). While doing his BSc thesis he developed a keen interest on food systems from a soft matter perspective, studying the *in vitro* digestibility of cellulose ether emulsions. He continued his MSc studies at Wageningen University and Research, between 2016-2019, where he did a double specialization in Ingredient Functionality and Gastronomy, graduating *Cum Laude*. His first MSc thesis was dedicated to the surface rheology and properties of viscoelastic interfaces subjected to fast and large deformations. The results were published in the *Journal of Colloids and Interface Science*, and *Food Hydrocolloids*. The second MSc thesis was on the effect of pH and ionic strength on the molecular properties of yellow pea protein fractions. He performed his MSc internship at the Technical University Berlin, Germany, on the topic of enzymatic hydrolysis of pea protein and its effect on the rheological properties of plant-based yogurts. The main results were published in *Food Hydrocolloids*. After his MSc, he was hired as a PhD candidate in the department of Physics and Physical Chemistry of Foods, at Wageningen University and Research, Netherlands. During his PhD, he conducted research on the non-linear rheological behavior of complex structures with different macroscopic ordering level, from disordered to ordered systems. The main results of his PhD research are presented in this thesis.

Contact:
Email - gerard.gimenezribes@gmail.com
Linkedin - www.linkedin.com/in/gerardgimenezribes

List of publications

This thesis

- **Chapter 2: Giménez-Ribes, G.**, Motaghian, M., van der Linden, E., & Habibi, M. Crumpled structures as robust disordered mechanical metamaterials. *Materials & Design*, 232, 112159 (2023).
- **Chapter 3: Giménez-Ribes, G.**, van der Linden, E., & Habibi, M. Auxetic behavior and unusual shear resistance of crumpled materials: Opportunities for programming the nonlinear responses of crumpled mechanical metamaterials. *Materials & Design*, 223, 111258 (2022).
- **Chapter 4:** Shaebani, M. R.*, **Giménez-Ribes, G.**,* Zondervan, S., Sagis, L. M. C., van der Linden, E., & Habibi, M. Universal Transition to Wide Shear Zones in Entangled Macroscale Chains or Ropes. *arXiv preprint arXiv:2208.13516* (2022) *Manuscript submitted to journal.*

  * Co-first author
- **Chapter 5: Giménez-Ribes, G.**, Oostendorp, M., van der Goot, A. J., van der Linden, E., & Habibi, M. Effect of fibrillar orientation on the shear rheology and Poynting effect in meat and meat analogues. *Manuscript submitted to journal.*
- **Chapter 6: Giménez-Ribes, G.**, Ghorbani, A., Teng, S. Y., van der Linden, E., & Habibi, M. Normal and shear responses of

origami cylinders: normal response reveals structural asymmetries. *Manuscript in preparation.*

Other research

- **Giménez-Ribes, G.**, Habibi, M., & Sagis, L. M. C. Interfacial rheology and relaxation behavior of adsorption layers of the triterpenoid saponin Escin. *Journal of colloid and interface science*, 563, 281-290 (2020).

- **Giménez-Ribes, G.**, Sagis, L. M., & Habibi, M. Interfacial viscoelasticity and aging effect on droplet formation and breakup. *Food Hydrocolloids*, 103, 105616 (2020).

- Klost, M., **Giménez-Ribes, G.**, & Drusch, S. Enzymatic hydrolysis of pea protein: Interactions and protein fractions involved in fermentation induced gels and their influence on rheological properties. *Food Hydrocolloids*, 105, 105793 (2020).

- **Giménez-Ribes, G.***, Yang, J.*, He, Q., Habibi, M., & Sagis, L.M.C. Self-similarity and Payne effect of whey protein-escin mixtures at the air-water interface. *Food Hydrocolloids*, 139, 108554 (2023).

  * Co-first author

- Yang, J.*, **Giménez-Ribes, G.***, He, Q., Habibi, M., & Sagis, L.M.C. Surface dilatational and foaming properties of whey protein and escin mixtures. *Food Hydrocolloids*, 144, 108941 (2023).

  * Co-first author

- Yang, J., Risse, K, De Groot, A, Shen, P., Hinderink, E., **Giménez-Ribes, G.**, Landman, J., & Sagis, L.M.C. Review on interfacial large amplitude oscillatory dilatation (LAOD) rheology. *Manuscript in preparation.*

- Feichtinger, A., **Giménez-Ribes, G.**, Landman, J., & Scholten, E. Influence of capillary bridge formation on the rheological properties of protein oleogels. *Manuscript in preparation.*

- Jarray, A., Motaghian, M., **Giménez-Ribes, G.**, & Scholten, E. Structure and rheological behaviour of bidisperse capillary suspensions. *Manuscript in preparation.*

- Motaghian, M., **Giménez-Ribes, G.**, Ji, Lei, van der Linden, E., Scholten, E., & Habibi, M. Polymer-surfactant mixtures: Rheology and tribology. *Manuscript in preparation.*

Overview of completed training activities

Discipline specific activities

Title	Organization	Year
17^{th} European School on Rheology	KU Leuven in BE	2019
Physics @ Veldhoven	NWO in NL	$2020^{\dagger}$
Rheology, the do's and dont's	WUR in NL	2020
Physics @ Veldhoven	NWO in NL	$2021^{\dagger}$
Physics @ Veldhoven	NWO in NL	$2022^{\dagger}$
18^{th} Food Colloids Conference	Lund University, Online	$2022^{\dagger}$
Annual European Rheology Conference	European Society of Rheology in ES	$2022^{\dagger}$
Physical Chemistry Han-sur-Lesse Winterschool	WUR in BE	2022
2nd Edible Soft Matter Conference	WUR in NL	$2022^{\dagger}$
36^{th} EFFoST	University College Dublin in IE	$2022^{\dagger}$
32^{nd} Dutch Soft Matter Meeting	WUR in NL	2022^{*}
NWO Physics	NWO in NL	2023^{*}
9^{th} International Congress on Food Rheology and Structure	WUR in NL	2023^{*}
XIX^{th} International Congress on Rheology	Hellenic and Israeli Societies of Rheology in GR	2023^{*}

† Poster presentation

* Oral presentation

General Courses

Title	Organization	Year
SolidWorks course	PCC, WUR in NL	2019
PhD Workshop Carousel	WGS in NL	2019
VLAG PhD Week	VLAG in NL	2019
Introduction to R programming	VLAG in NL	2020
Adobe InDesign Essential Training	WUR Library in NL	2020
Applied Statistics	VLAG in NL	2020
Career Perspectives	WGS in NL	2022

Other activities

Title	Organization	Year
Preparation of research proposal		2019
Weekly group meetings	FPH in NL	2019-2023
Using python for research	Harvard University (Online edX)	2020
Databases and SQL for Data Science with Python	IBM (Online Coursera)	2022

Assisting in teaching/supervision activities

Title	Organization	Year
Physical Chemistry for Food Scientists	FPH	2019-2022
Food Ingredient Functionality	FPH	2019-2022
Supervision of 6 MSc thesis	FPH	2019-2023

The research described in this thesis has been funded by the Netherlands Organization for Scientific Research (NWO) through NWO-VIDI grant No. 680-47-548/983.

Financial support from Wageningen University and Research for printing this thesis is gratefully acknowledged.

Layout and cover design by Gerard Giménez I Ribes. Cover design created by adapting Anders Hoff's (GitHub user @inconvergent) "Sand spline" generative art Python algorithm.

Printed by Proefschriftenmaken.nl.